KINETIC ENERGY FLUCTUATION-DRIVEN LOCOMOTOR TRANSITIONS ON POTENTIAL ENERGY LANDSCAPES OF BEAM OBSTACLE TRAVERSAL AND GROUND SELF-RIGHTING

by

Ratan Sadanand Othayoth Mullankandy

A dissertation submitted to Johns Hopkins University
in conformity with the requirements for
the degree of Doctor of Philosophy

Baltimore, Maryland
October 2021

Abstract

Animals' physical interaction with their environment, although often difficult, is effective and enables them to move robustly by using and transitioning between different modes such as running and climbing. Although robots exhibit some of these transitions, we lack a principled approach to generating and controlling them using effective physical interaction. Bridging this knowledge gap, in addition to advancing our understanding of animal locomotion, will improve robotic mobility.

Recent studies of physical interaction with environment discovered that during beam obstacle traversal and ground self-righting, discoid cockroaches use and transition between diverse locomotor modes probabilistically and via multiple pathways. To traverse beams, the animal first pushes against them, but eventually pitches up due to beam restoring forces, following which it either pushes across beams (pitch mode) or rolls into the gap (roll mode). To self-right, the animal opens and pushes its wings against the ground, which pitches its body forward (metastable mode), and then rolls sideways (roll mode). Here, we seek to begin to explain these observations by integrating biological, robotic, and physics studies. We focus on pitch-to-roll and metastable-to-roll transitions of cockroaches during escape and emergency responses and feedforward-controlled

robots.

We discovered that across both systems, physical interaction is stochastic, with animals showing more variability. Animal and robot system states are strongly attracted to basins of their potential energy landscape, resulting in stereotyped locomotor modes. Locomotor transitions are probabilistic barrier-crossing transitions between landscape basins. Whereas the animal and robot traversed stiff beams via roll mode, they pushed across flimsy beams, suggesting that modes with easier physical interaction are more probable to occur (more favorable). Varying potential energy barriers by changing beam torsional stiffness (in the animal and robot) and kinetic energy fluctuation by changing body oscillation (in the robot) in both beam traversal and self-righting revealed that kinetic energy fluctuation comparable to the barrier facilitates probabilistic transition to the more favorable mode. Changing the system configuration (self-righting robot's wing opening) facilitates transitions by lowering the barrier. The animal's pitch-to-roll transition during beam traversal occurred even with insufficient kinetic energy fluctuation, suggesting that sensory feedback may be involved. These discoveries support the use of potential energy landscapes as a framework to understand locomotor transitions. Finally, we implemented methods for tracking and 3-D reconstruction of small animal locomotion in an existing terrain treadmill.

Primary Reader and Advisor: Chen Li

Secondary Readers: Noah J. Cowan, Louis L. Whitcomb

Acknowledgments

I am deeply indebted to my advisor, Prof. Chen Li, for accepting me into his group, the effort he has put into training me on multiple fronts, and the kindness he has shown me over the years. Working with him since day one of Terradynamics Lab has been a rewarding experience. It would be an understatement to say that I have been lucky enough to have him as my advisor.

I have had the privilege of being taught by an amazing set of teachers during my time at Hopkins. I would especially like to thank Prof. Noah Cowan, Prof. Louis Whitcomb, and Prof. Gregory Chirikjian. The seven classes that I have taken between them were not only interesting but were often a good breather from my experimental work in lab.

I thank the members of the Terradynamics Lab, past and present, for making my time in lab enjoyable and intellectually stimulating. I am grateful to Sean Gart, Rick Han, Thomas Mitchel, George Thoms, Qihan Xuan, Qiyuan Fu, Yaqing Wang, Allen Ren, Divya Ramesh, and Eugene Lin for the help and support they have given me in during my years at the Terradynamics Lab. I thank Qihan and Qiyuan for their thoughtful questions and suggestions, which has often helped notice some of the aspects of my work that I overlooked. I have also had the privilege of mentoring Yaqing, Divya, and Allen during their

early days in lab, which proved to be a very rewarding experience for me.

I would like to thank my committee members Prof. Noah Cowan and Prof. Louis Whitcomb for their support and reading of my dissertation. I also thank Prof. Yannis Kevrekidis, Prof. Avanti Athreya, Prof. Gregory Chirikjian, Prof. Noah Cowan, and Prof. Mehran Armand for examining me at my graduate qualifiying examinations.

I thank the academic staff at Department of Mechanical Engineering and Laboratory for Computational Sensing and Robotics—especially, Mike Bernard, Kevin Adams, Lorrie Dodd, Jordan Card, Ashley Moriarty, Alison Morrow, and Rose Chase. They generously provided me academic and logistical support during various stages of my Ph.D., which enabled me to spend time on research without having to worry too much about purchases and reimbursements. I would also like to acknowledge the funding sources of Terradynamics Lab; my research would not have been possible without the generous funding that Chen and the lab received from the Army Research Lab, the Beckman Foundation, the Burroughs Wellcome Fund, and the Whiting School of Engineering at Johns Hopkins.

During my Ph.D., I have had the pleasure of being a part of the amazing scientific communities of comparative biomechanics and robophysics. In addition to giving the much needed morale boost, their scientific meetings were also an opportunity to meet a diverse set of researchers. The suggestions I received during these meetings—especially from Prof. Bob Full, Prof. Dan Goldman, Prof. Shai Revzen, and Prof. Simon Sponberg—have been crucial in improving certain sections of this dissertation. In addition, I would like to thank Prof. Simon Sponberg, Prof. Jean-Michel Mongeau, Prof. Kaushik Jayaram, and

Prof. Shai Revzen for the career advice they have given me.

I have had the good fortune to make and count on some really good friends during my time at Hopkins. Arun Nair, Karuna Agarwal, Rupini Shukla, and Anjali Nelliat have always been there to lift me up and offer sage advice during trying times. Radhika Rajaram, Weiqi Wang, and Qiaozhi Wang ensured that our study sessions were not only productive, but also fun. I would also like to thank Stephanie Hao, Chris Weng, Ting Yung Fang, and Poojan Oza for making my time at Hopkins memorable. I am also grateful to Emanuel Chirayath, Safvan Palathingal, and Nirmal Sabu for their camaraderie since our days as roommates at National Institute of Technology Calicut.

Finally, I thank my family: my parents, Sadanandan and Poornima, for their unconditional love and immense support for pursuing my dreams, through the ups and downs in my life; my grandmother Sarojini, for her constant encouragement and advice; my brother Rajat, who has often been the elder (and very likely the richer) one between us, for being there for me, no matter what; my partner Rupini, for her love and support over the past three years and also 'bearing' with my ever-changing plans.

Table of Contents

List of Tables

List of Figures

Chapter 1

Introduction

1.1 Motivation and Significance

Movement is one of the most ubiquitous and conspicuous features of animals (Alexander, 2006; Biewener, 2003; Tinbergen, 1955) and occurs across diverse environments ranging from rainforests to deserts to flat plains, and over large spatiotemporal scale. Animals' terrestrial locomotion in such natural environments, requires generating necessary propulsion (Taylor and Heglund, 1982), which results in significant physical interaction of limbs and often the body with the terrain (Alexander, 2006; Biewener, 2003; Dickinson et al., 2000). Physical interaction between animal and environment is often complex and seemingly difficult (Dickinson et al., 2000; Holmes et al., 2006). In addition to the heterogeneity and variation in physical properties such as shape, size, and stiffness of environment and continual terrain contact, animals must also operate under the constraints imposed by their morphology and physiology (Figure 1.1). These may limit the animals' propulsion (Dickinson et al., 2000; Taylor and Heglund, 1982) when moving in their environment.

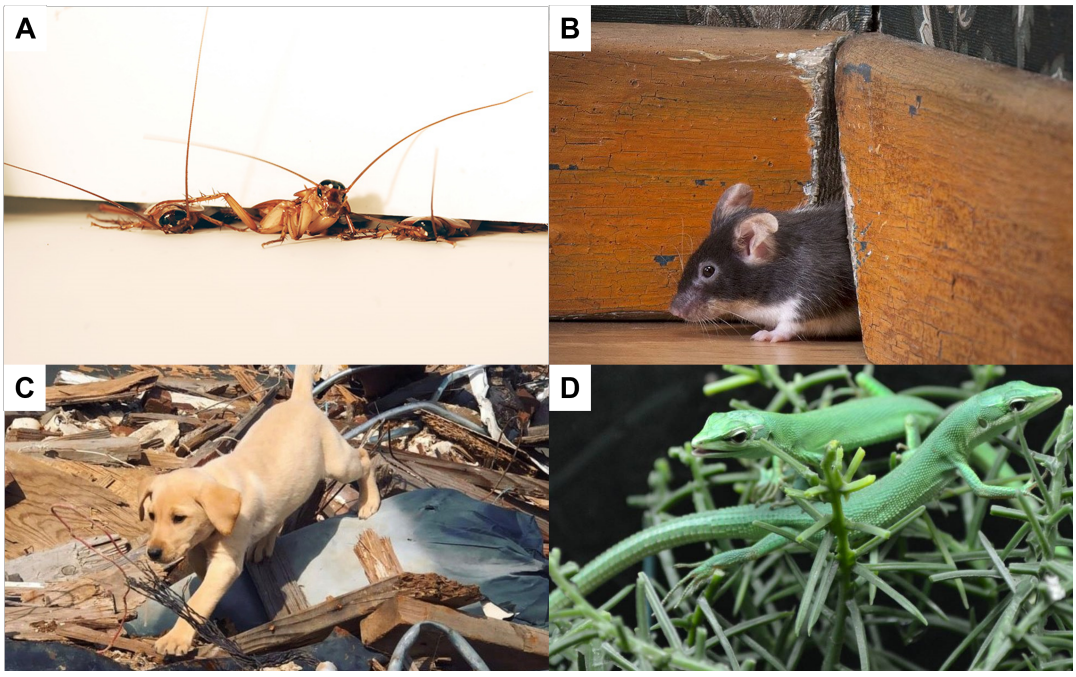

Figure 1.1: Physical interaction during terrestrial locomotion is constrained by environmental, morphological, and physiological constraints. Examples of physical interaction during locomotion. (A) American cockroach exiting a crevice. (B) Mouse passing trough a vertical gap. (C) Search and Rescue dog moving in rubble. (D) Lizards moving through flexible shrubs. Images courtesy of (A) PolyPEDAL Lab, (B) Getty Images, (C) Ground Zero Emergency Canine Training, (D) LLL Reptile and Supply Co Inc.

Despite these seeming difficulties during physical interaction, terrestrial locomotion in biological organisms is robust and agile (Dickinson et al., 2000; Biewener, 2003; Alexander, 2006). Even with perturbations from continual contact and instabilities in the environment (Sponberg and Full, 2008; Biewener and Daley, 2007) and the biomechanical constraints imposed on them (Biewener, 2003; Holmes et al., 2006), animals adjust their physical interaction to generate and maintain sufficient propulsion. Furthermore, in the extreme case of losing foothold and flipping over on their back, animals self-right to get back on their feet and continue moving (Ashe, 1970; Full, Yamauchi, and Jindrich, 1995; Li

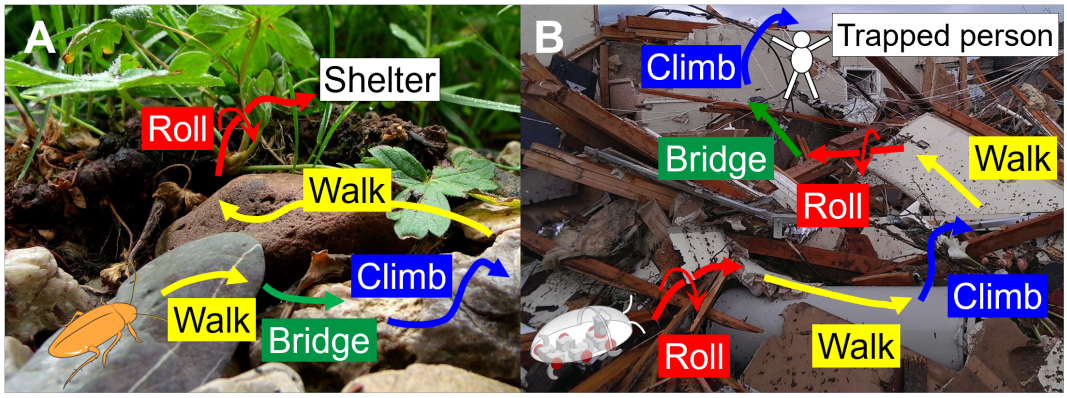

Figure 1.2: Illustrative examples of animal and robot locomotor transitions. Reproduced from (Othayoth, Thoms, and Li, 2020). Image credit: (A) Scott Brill.

et al., 2019). Often, running or walking alone cannot accomplish effective locomotion in varying environments (e.g., cluttered forest floor, sparse branches in canopy, etc.) and animals must transition (Lock, Burgess, and Vaidyanathan, 2013; Low et al., 2015) between different modes of locomotion such as climbing (Goldman et al., 2006), rolling (Domokos and Várkonyi, 2008), burrowing (Winter et al., 2014), or even self-righting (Li et al., 2019) (Figure 1.2A). They do so robustly by making effective physical interaction with the environment.

Advancements in robotics over the past decades (Raibert, 1986; Saranli, Buehler, and Koditschek, 2001; Raibert, 2008) have enabled robots to walk and run stably across surfaces that are rigid (Raibert, 1986; Raibert, 2008), rugged (Saranli, Buehler, and Koditschek, 2001), and even yielding (Li et al., 2009; Li, Zhang, and Goldman, 2013; Aguilar and Goldman, 2016). State-of-the-art legged robots such as those from Boston Dynamics (Bouman et al., 2020), Ghost Robotics (Kenneally, De, and Koditschek, 2016), and ANYbotics (Hwangbo et al., 2019; Lee et al., 2020) have not only begun to walk and run

effectively in modest terrain but also transition to modes such as jumping and somersaulting. However, the ability of such robots to transition between modes is far from robust, and perhaps even fragile, in complex terrain with obstacles as large as themselves. It is crucial to be able to robustly transition between different modes of locomotion for robots to move effectively in natural, artificial or extraterrestrial environments (which often have physical constraints) to autonomously perform tasks such as search and rescue in earthquake rubble (Murphy et al., 2008), environmental monitoring in forests (Dunbabin and Marques, 2012), extraterrestrial exploration on Mars (Titus et al., 2021), and home service (Forlizzi and DiSalvo, 2006).

To enable these capabilities, we need general physics models that can inform us how to predict and generate the necessary propulsion (Koditschek, 2021) to interact with environment for transitioning to, avoiding, or escaping from locomotor modes beyond walking and running. Improving robotic mobility in extreme environments is a grand challenge in robotics (Yang et al., 2018), and understanding the physics of locomotor transitions is an essential ingredient for addressing this challenge.

A major obstacle towards accomplishing this grand challenge in robotics is that we do not yet well understand how to make direct physical interaction with their environment to transition between locomotor modes. Although existing models such as the spring-loaded inverted pendulum (SLIP) model (Blickhan and Full, 1993) are effective and generalize over a broad range of locomotor-terrain parameters for dynamic running or walking (Holmes et al., 2006), they do not inform locomotor transitions. In particular, we lack principled approaches

and theoretical concepts for thinking about how to generate and control locomotor transitions emerging from physical interaction that are on the same level as SLIP model for single-mode locomotion (Holmes et al., 2006). Bridging this knowledge gap, in addition to advancing to our understanding of how biological organisms move (Dickinson et al., 2000; Padilla et al., 2014), will also enable robots to move robustly in nature for societally relevant applications (Yang et al., 2018) such as search and rescue and environmental monitoring.

This dissertation is a step towards beginning to establish a framework towards understanding how locomotor transitions emerge from physical interaction with terrain. The following sections of this chapter will discuss the necessary scientific background, the specific knowledge gaps that I seek to address, and the approach towards addressing them.

1.2 Background

Existing physics models in legged locomotion of animals and robots predominantly focus on generating (Blickhan and Full, 1993; Goldman et al., 2006; Kuo, 2007; Li, Hsieh, and Goldman, 2012), stabilizing (Biewener and Daley, 2007; Couzin-Fuchs et al., 2015; Revzen et al., 2013) or transitioning between (Bramble and Lieberman, 2004; Diedrich and Warren, 1995; Hoyt and Taylor, 1981; Li, 2000) steady-state between walking and running. But the physical principles and insights from these studies do not translate to scenarios where the animal or robot must make locomotor transitions using physical interaction while operating under environmental or biomechanical constraints. The studies in this dissertation are motivated by the recent observations of physical interaction during traversal of flexible beam-like obstacles (Li et al., 2015) and self-righting on flat ground (Li et al., 2019) in discoid cockroaches (*Blaberus discoidalis*, Figure 1.3).

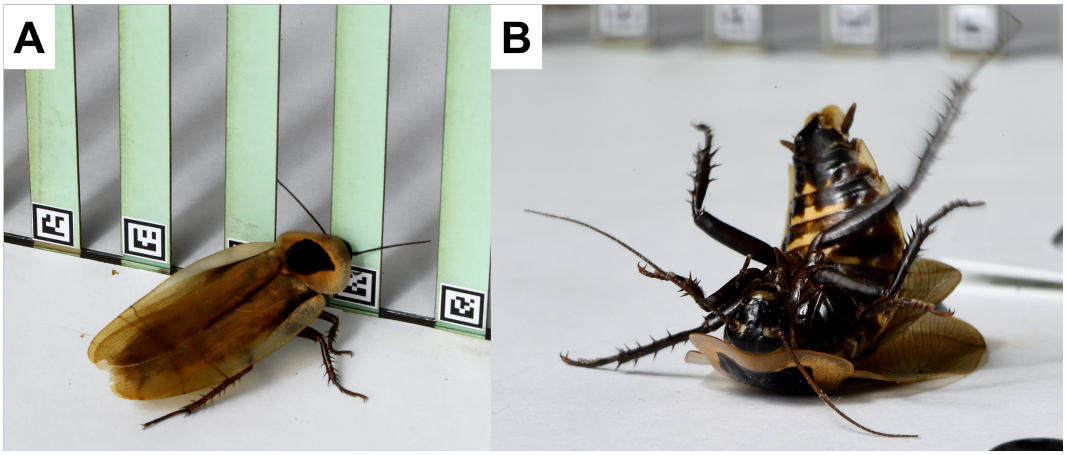

Figure 1.3: Model organism and model systems. Discoid cockroach (*Blaberus discoidalis*) (A) traversing flexible beams and (B) self-righting on flat ground. Images courtesy of Will Kirk, Homewood Photography.

In both beam obstacle traversal (Li et al., 2015) and ground self-righting (Li et al., 2019), the animal displayed diverse, probabilistic locomotor transitions that emerged via constrained physical interaction with its environment. To traverse flexible beam obstacles or self-right, animals must physically interact with the environment, which is often constrained or strenuous. For example, traversing layers of adjacent beams with a gap narrower than their body width is difficult for animals (Li et al., 2015); so is pushing against stiff beams which may not deflect easily due to large restoring forces. Similarly, to self-right, animals must overcome potential energy barriers that are seven times greater than the mechanical energy required per stride for steady-state, medium speed running (Kram, Wong, and Full, 1997) or, exert ground reaction forces eight times greater than that during steady-state medium speed running (Full, Yamauchi, and Jindrich, 1995). In the this section, we briefly summarize the results from previous studies of locomotor transitions in beam obstacle traversal (Li et al., 2015) and ground self-righting of cockroaches (Li et al., 2019).

1.2.1 Model system I: Beam obstacle traversal

To begin to understand physical interaction of animals with their environment in three dimensions, Li and colleagues (Li et al., 2015) challenged cockroaches to traverse flexible beams with gaps smaller than their body width. The study discovered that during the physical interaction to traverse the beam obstacles, cockroaches use different modes such as climbing up the beams, rolling in between the beam gaps, pushing against the beams, falling forward, or moving laterally (Figure 1.4A). Animals transitioned between different modes and did

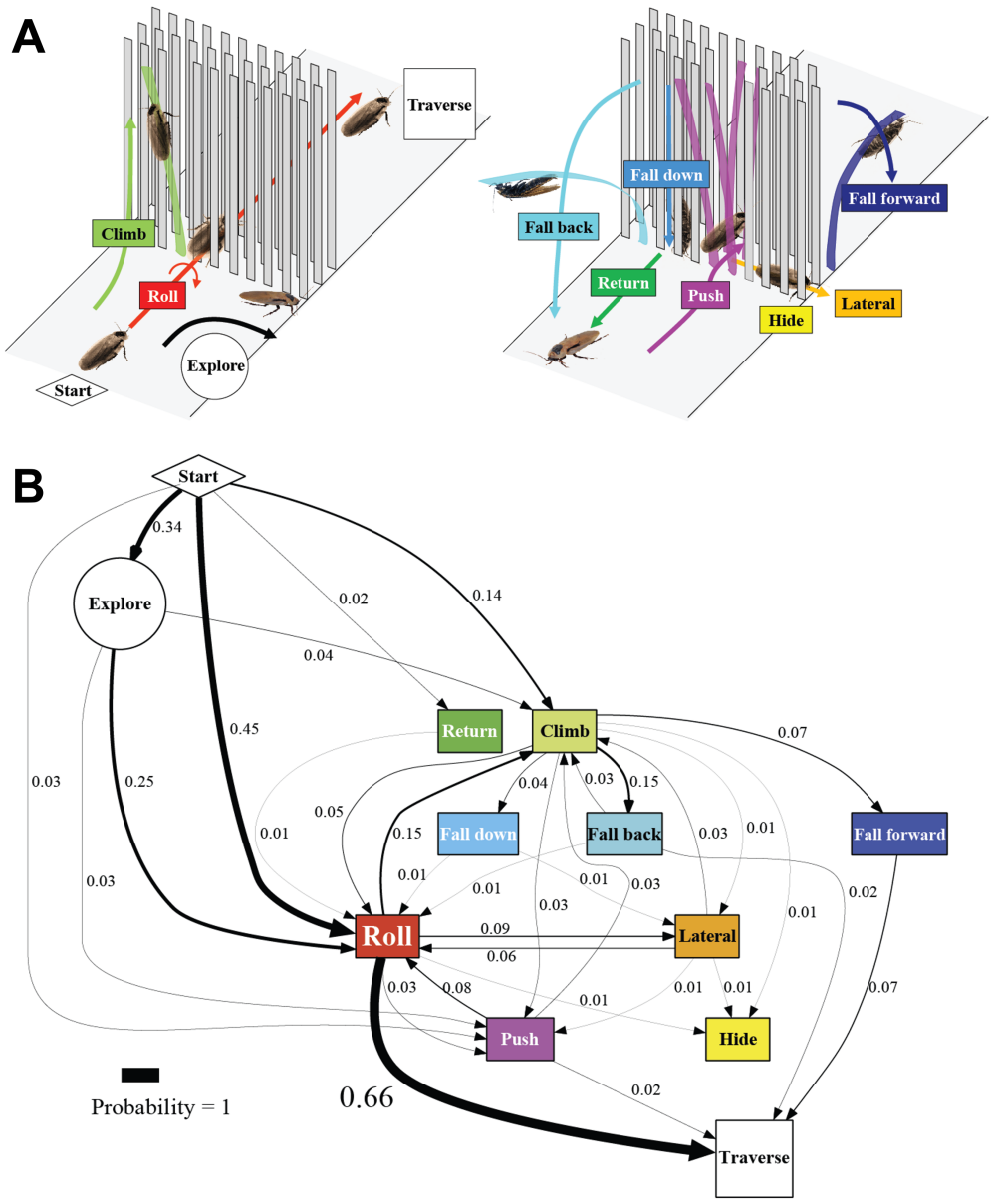

Figure 1.4: Model system I : Beam obstacle traversal. (A) Schematic of diverse locomotor modes observed during beam traversal. (B) Multi-pathway locomotor transitions and their probabilities during beam traversal. Reproduced from (Li et al., 2015).

so via multiple pathways with varying probabilities (Figure 1.4B) during traversal attempts. Some modes and transitions were more likely to occur than others, with traversal most likely to occur via body rolling. This fact was attributed to the streamlined ellipsoidal shape of the cockroach, which induced body rolling from passive mechanical interactions. The study also hypothesized that body rolling may be induced by the animal's kinetic energy fluctuation from constant body vibrations due to intermittent ground contact. Using a simplified physics model (Figure 1.8), the authors speculated that during traversal, the animal must overcome a potential energy barrier which may vary across different modes (see Section 1.3 for details).

1.2.2 Model system II: Winged self-righting on flat ground

An interesting observation in beam obstacle traversal (Li et al., 2015) led to a more detailed study on self-righting (Li et al., 2019). As the cockroach traversed and exited the beam obstacle field, it occasionally became unstable, lost its foothold, and fell on its back but almost always self-righted to continue moving. Li et al., 2019 discovered that cockroaches self-right on flat ground via diverse strategies such as by opening their wings against ground (winged self-righting) or by pushing their legs against the ground (legged self-righting) (Figure 1.5A). It was also observed that physical interaction with flat ground resulted in probabilistic transitions between self-righting modes via multiple pathways (Figure 1.5). Certain modes and transitions were more likely to occur. In addition, the animal frequently and vigorously flailed its legs during

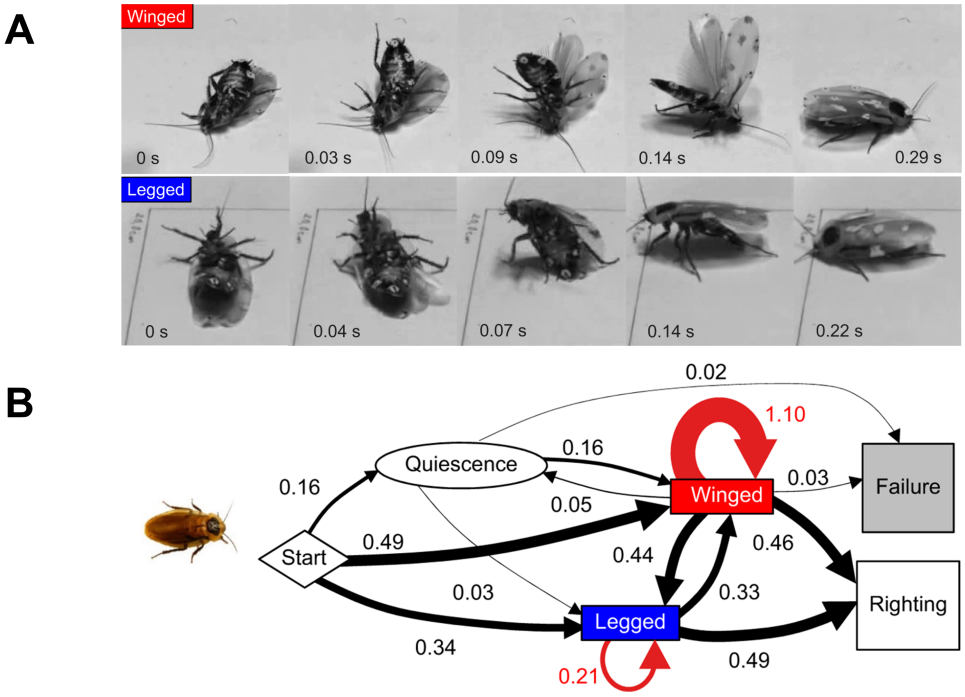

Figure 1.5: Model system II : Ground self-righting (A) Winged and legged modes observed during self-righting. (B) Multi-pathway locomotor transitions and their probabilities during beam traversal. Reproduced from (Li et al., 2019)

its self-righting attempts; it was presumed that these created small kinetic energy fluctuation, which seem wasteful. Finally, the study proposed a simplified physics model (Figure (1.9); see Section 1.3 for details) which was used to posit that different modes overcame varying potential energy barriers.

1.3 Towards a conceptual framework to understand locomotor transitions emerging from physical interaction

While seeking to begin to explain the common observations (see Section 1.2) in both beam obstacle traversal (Li et al., 2015) and self-righting (Li et al., 2019), we found interesting analogies between microscopic protein folding transitions and macroscopic locomotor transitions. In this section, I describe how mechanistic models for protein folding transitions inspired a framework to understand locomotor transitions in beam obstacle traversal and ground self-righting, and more broadly a variety of model systems studies in our lab (for a review, see Othayoth et al., 2021b).

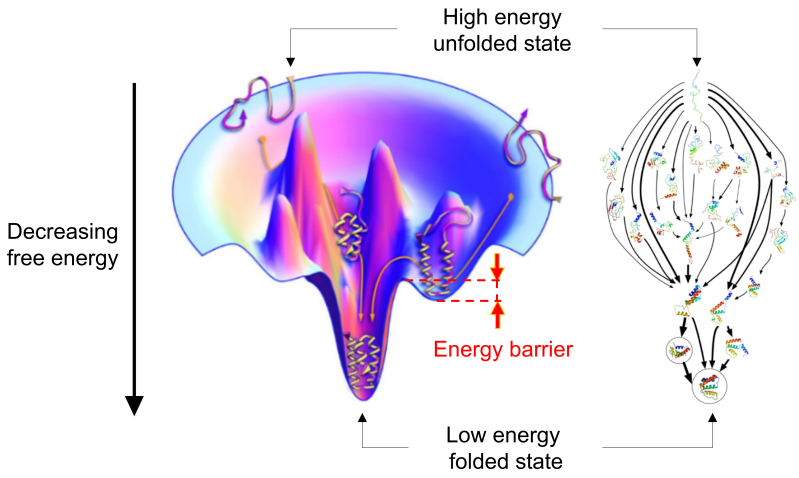

Figure 1.6: Free energy landscapes of protein folding transitions. Left: Funnel shaped free energy landscapes of protein folding. As proteins fold, their state moves transitions from a high energy state to a low energy state by overcoming free energy barriers. Modified from Dill and MacCallum, 2012. Right: Schematic of stochastic, multi-pathway protein folding transitions. Thicker arrows show transitions that are more probable. Modified from Voelz et al., 2012.

1.3.1 Inspiration: Free energy landscapes of protein folding transitions

Our approach for understanding locomotor transition emerging from physical interaction with environment is directly inspired by free energy landscapes of multi-pathway protein folding transitions (Dill and Chan, 1997; Onuchic and Wolynes, 2004; Wales, 2003). Free energy landscape is a function of all possible confirmations (molecular structure) of a protein molecule (Figure 1.6). Microscopic, near-equilibrium proteins have a three-dimensional chain-like conformation which is initially unfolded and has a high free energy. To achieve its biological function, the unfolded protein chain must fold into a specific confirmation called the native state, which has the lowest possible free energy. However, the transition from unfolded to native state does not occur in a single step; instead, unfolded states progressively transition to various intermediate states before reaching the native state. Lower free energy states are more stable and hence thermodynamically more favorable. When the protein folding problem is seen through the lens of free energy landscapes (Figure 1.6), the following observations emerge:

1. Free energy landscapes have peaks (local free energy maxima) and basins (local free energy minima) (Wales, 2003; Socci, Onuchic, and Wolynes, 1996).

2. When proteins fold, they transition from higher energy states/basins to lower energy states/basins. In other words, proteins transition towards thermodynamically more favorable, lower energy states (Onuchic, Luthey-Schulten, and Wolynes, 1997).

3. The transitions from high energy state/basin to a low energy state/basin requires overcoming substantial free energy barriers separating the basins, which is enabled by the random thermal energy fluctuation. Hence, transitions are probabilistic (Dill and MacCallum, 2012; Onuchic and Wolynes, 2004).

4. Proteins can probabilistically transition via multiple pathways. However, some transitions are more likely than others depending on the thermodynamic favorability, barrier height, and thermal energy fluctuation (Onuchic, Luthey-Schulten, and Wolynes, 1997).

5. In addition to thermal energy fluctuation, transitions can also be enabled by modifying the landscape to lower the transition barrier (Dill and Chan, 1997).

Although our model systems (Li et al., 2015; Li et al., 2019) of beam traversal and self-righting are macroscopic, self-propelled, and far-from-equilibrium, their locomotor transitions share several similarities such as diverse locomotor modes, multi-pathway transitions between locomotor modes that occur probabilistically, and preference of some modes over others. Inspired by the seeming similarities of our system to them, we contend that the potential energy landscape approach helps understand how self-propelled, far-from-equilibrium macroscopic animals' and robots' probabilistic locomotor transitions during traversal of flexible beam obstacles and self-righting on flat ground emerge from physical interaction, whose equations of motion are unknown or intractable (Aguilar et al., 2016).

1.3.2 Plausibility of a potential energy landscape approach to locomotor transitions

A major challenge to modelling physical interaction during locomotor transitions is the high degrees of freedom. Although the physical interaction obeys Newton's laws of motion, solving (or even deriving) the equation for such complex systems is often intractable. Given these complexities, and the fact that transitions are probabilistic in both beam obstacle traversal (Li et al., 2015) and self-righting (Li et al., 2019), a statistical physics-like approach may prove useful. A statistical physics treatment has advanced understanding of complex, stochastic, macroscopic phase transitions in self-propelled living systems, such as animal foraging (Viswanathan et al., 2011), traffic (Helbing, 2001), and active matter (Fodor and Marchetti, 2018; Ramaswamy, 2010).

Previous use of potential energy functions approaches for robot manipulation and parts alignment (Peshkin and Sanderson, 1988; Brost, 1992; Krishnasamy, 1996) and grasping (Zumel, 1997) also suggests that a potential energy landscape approach may be a plausible framework towards understanding physical interaction. In these systems, robot-part contact is not only unavoidable, but also often involves continual collision (Peshkin and Sanderson, 1988; Zumel, 1997; Krishnasamy, 1996; Mohri and Saito, 1994; Swanson, Burridge, and Koditschek, 1995), which is similar to the intermittent animal- or robot-environment contact during locomotor transitions. Although understanding these interactions by solving equations of motion remained intractable, simplified quasi-static potential energy field models derived from first principles well explained how the shape of robots and parts affected their physical interaction

(Brost, 1992; Krishnasamy, 1996; Zumel, 1997). In addition, they also informed planning strategies to achieve the desired alignment even with uncertainties in part orientation, friction, and intermittent contact dynamics (Peshkin and Sanderson, 1988; Brost, 1992; Zumel, 1997).

The success of these potential energy function-based methods in robotics further suggests that a potential energy landscape approach, such as those posited by Li et al., 2015 for beam traversal and Li et al., 2019 for self-righting, may prove useful to understand how locomotor transitions emerge from physical interaction of animals and robots with environment.

1.3.3 Difference from artificial potential field approaches in robotics

Previously, artificial potential functions have been used for robot navigation (Khatib, 1986; Rimon and Koditschek, 1992) and visual servoing (Cowan and Koditschek, 1999). It was first proposed[1] by Oussama Khatib, in the context of robot arm collision avoidance. In this approach, the state of the robot is considered as moving in a field of forces. The goal state to be reached is an attractive pole, and the obstacles to be avoided are repulsive surfaces for the robot. In this method, the goal and obstacle exert virtual forces on the robot—i.e., as the robot's becomes closer to the obstacle, it experiences a virtual repulsive force that pushes it away (closer the robot, larger the repulsion from obstacle) and avoids collision (Figure 1.7A). In addition, the goal exerts a virtual attractive force on the robot. The sum of attractive and repulsive potential field ideally results in a potential field with a global minima at the goal state to which

[1] Although a 1979 article (Larcombe, 1979) fleetingly mentions the possibility of using repulsive potential fields for robot navigation, no analysis was reported

the robot state is attracted while avoiding obstacles. By choosing the closed form-expression for attractive and repulsive forces (and the associated potential field), the robot motion can be controlled.

Rimon and Koditschek later proposed a new class of potential functions—navigation functions (Rimon and Koditschek, 1992)—that not only finds a collision-free path for the robot, but also specifies a feedback controller for the robot. Navigation functions are guaranteed to bring a bounded-torque actuated robot to a desired state while avoiding obstacles in a known and stationary environment (Figure 1.7B). Navigation functions have also been used for occlusion avoidance during vision-based control of rigid body motion (Figure 1.7C) (Cowan and Koditschek, 1999; Cowan, Lopes, and Koditschek, 2000).

Here, the choice of artificial potential (Khatib, 1986) or navigation function (Rimon and Koditschek, 1992) are not necessarily directly related to the system potential energy. However, the potential energy functions used in the approaches mentioned in Section 1.3.2 and those proposed previously in Li et al., 2015 and Li et al., 2019 are derived from first principles using a simplified physics model.

1.3.4 Insights from potential energy landscapes in previous studies of beam traveral and self-righting

Previous studies of beam obstacle traversal (Li et al., 2015) and self-righting (Li et al., 2019) used simple physics models to obtain the system potential energy (Figures 1.8A, 1.9A-C) and visualize the potential energy landscape (Figures 1.8B, 1.9D). Despite the simplicity of the physics models, the potential energy landscape posited possible explanations for some of the observations in beam

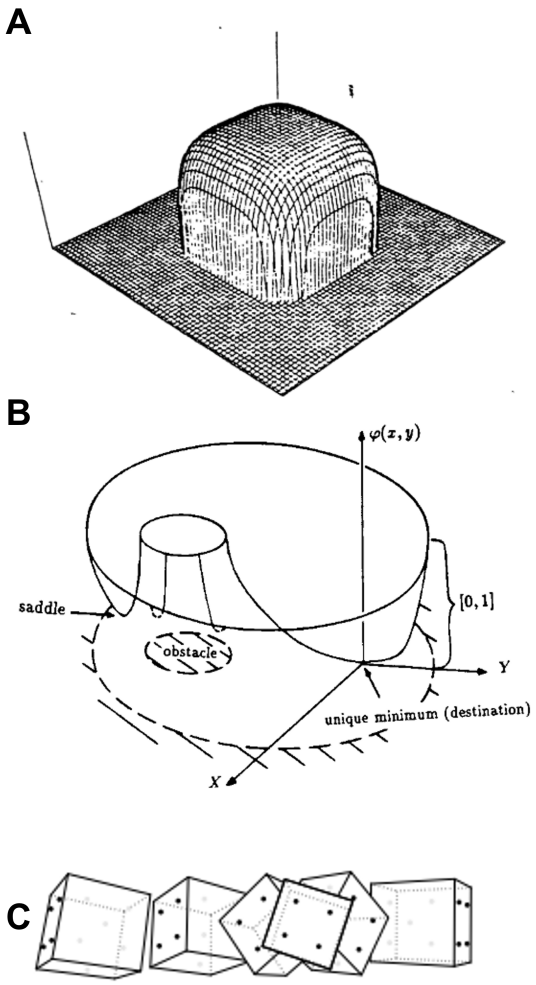

Figure 1.7: Potential field approaches in robotics. (A) A repulsive potential function around an obstacle. (B) An exact navigation function. (C) Simulated visual servoing of a rigid cube using a navigation function-based controller. Image credits: (A) Reproduced from Khatib, 1986, (B) Reproduced from Rimon and Koditschek, 1992, (C) Reproduced from Cowan, Lopes, and Koditschek, 2000.

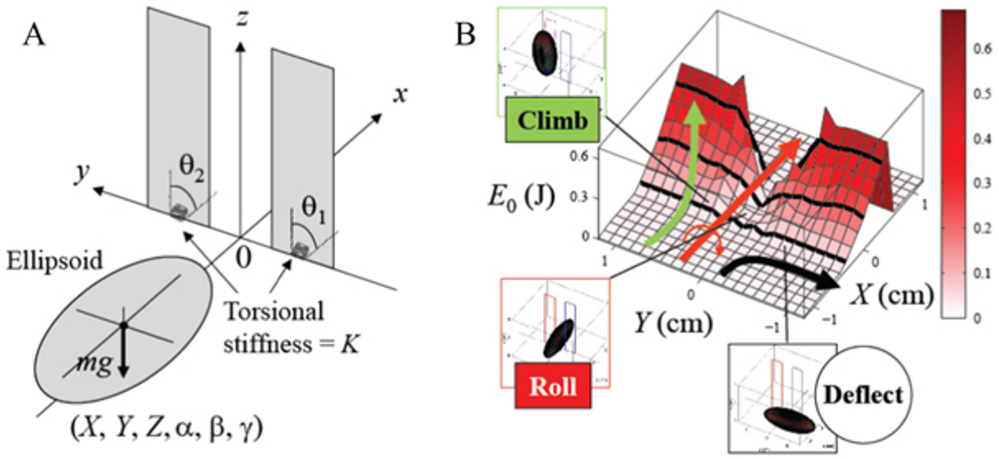

Figure 1.8: Minimal potential energy landscape of flexible beam traversal.(A) Simplified physics model to calculate system potential energy. (B) Potential energy landscape in the space of forward (X) and lateral (Y) body center of mass position. Colored arrows indicate hypothesized systems state trajectories on landscape. Roll mode (red arrow) overcomes lower barrier on landscape during traversal compared to climb mode (green arrow). Deflect mode (black arrow) does not result in traversal. Reproduced from (Li et al., 2015).

obstacle traversal and self-righting. For example, a minimal landscape for beam traversal (Li et al., 2015; Figure 1.8) posited that when traversing the system state on the landscape overcame lower barrier as for body rolling. In addition, it provided insights into the shape-dependent locomotor–ground interaction during movement in 3D, multi-component terrain; the model suggested that the rounded ellipsoid body of the animal results in attractive lateral forces towards the middle of the beams. Similarly, a potential energy landscape of a rigid ellipsoid (Li et al., 2019; Figure 1.9) hypothesized that self-righting via body rolling overcame lower potential energy barrier compared to that by body pitching.

While these landscapes provided initial qualitative explanations or hypotheses, they had a few shortcomings. In both these simplified potential energy

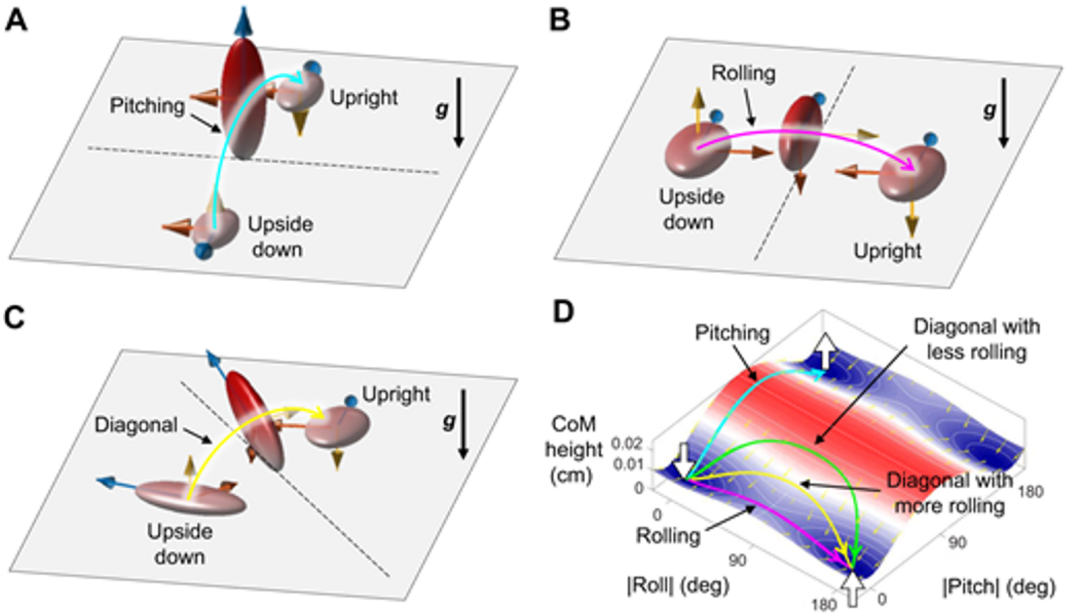

Figure 1.9: Static potential energy landscape of ground self-righting. (A-C) An ellipsoid approximating the animal body in contact with the ground, pitching (A), rolling (B) or rotating diagonally (simultaneous pitching and rolling; (D), Potential energy landscape, shown as the center of mass height in the space of body pitch and roll. Colored arrows indicate hypothesized system state trajectories for body rotations of modes shown in (A)-(C) Reproduced from (Li et al., 2019)

landscape models (Figures 1.8, 1.9), the systems potential energy depend on more than two parameters. The previous beam traversal landscape was a minimal potential energy landscape; Li et al., 2015 simply calculated the minimal potential energy over all rotational degrees of freedom for positions in the vicinity of the beam obstacles. Similarly in self-righting landscape, the animal's wing opening, which substantially changes potential energy, is not considered. Finally, neither of the previous studies investigated how the system state behaves on potential energy landscapes during physical interaction.

1.3.5 Hypotheses

Having reasoned about the validity of using potential energy landscape approach, we present the hypotheses about beam obstacle traversal and self-righting that we seek to resolve in this dissertation:

1. Macroscopic, far-from equilibrium locomotor transitions of beam traversal and self-righting systems are barrier-crossing transitions on their evolving potential energy landscapes.

2. When comparable to the potential energy barriers between basins, the kinetic energy fluctuation during beam traversal and self-righting facilitate escape from a landscape basin to make locomotor transitions.

3. When kinetic energy fluctuation is not sufficient to overcome barriers along certain directions, altering the system configuration changes the landscape and lowers the barriers to be comparable to the available kinetic energy fluctuation, which then induces transition.

4. Physical interaction in some modes are easier (more favorable) than other modes; locomotor-terrain system is more likely to transition to a more favorable mode.

I emphasize that these hypotheses have only been speculated and not tested in previous studies of beam traversal (Li et al., 2015) and self-righting (Li et al., 2019).

1.4 Approach

1.4.1 Integrative approach to bridge knowledge gap

Considering the challenges discussed in Section 1.3.2, studying physical interaction during locomotor transitions may seem daunting at first, but we posit that an interdisciplinary approach integrating biology, robotics, and physics will help reveal physical principles by testing the hypotheses posed in Section 1.3.5. Such an integrative approach has already begun to successfully advance the study of locomotor-terrain interactions (terradynamics, (Li, Zhang, and Goldman, 2013; Li et al., 2015); Figure 1.10), especially in granular media (see Goldman, 2014 for a review).

By creating controlled granular media testbeds, robotic physical models, and theoretical and computational models, recent studies elucidated how animals, and how robots should use physical interaction with granular media to move effectively both on and within sandy terrain. The general physical principles (Goldman, 2014) and predictive physics models (Goldman, 2014; Li, Zhang, and Goldman, 2013) not only advanced understanding of functional morphology (Li, Hsieh, and Goldman, 2012; Maladen et al., 2011; Sharpe et al., 2015), muscular control (Ding et al., 2013; Sharpe, Ding, and Goldman, 2013), and evolution (McInroe et al., 2016) of animals, but also led to new design and control strategies (Aguilar et al., 2016; Goldman, 2014; Li et al., 2009; Li et al., 2010; Marvi et al., 2014; Shrivastava et al., 2020) that enabled a diversity of robots to traverse granular environments.

Such an integrated approach offers several advantages. Observations of model organisms inspire robot design and action strategies (Ijspeert, 2014;

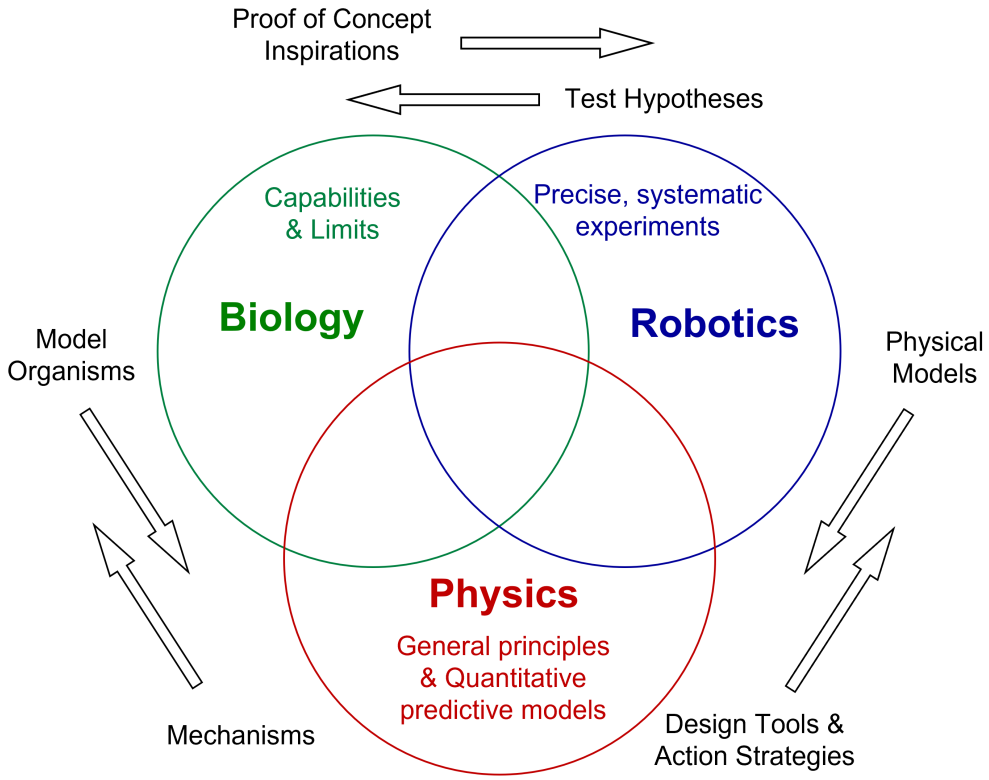

Figure 1.10: Integrative approach to understand physical interaction of animals and robots with their environment. Modified from Othayoth et al., 2021b; image courtesy of Chen Li.

Saranli, Buehler, and Koditschek, 2001; Teoh and Wood, 2013; Goldman, 2014; Shrivastava et al., 2020). Simplified robots serve as physical models for testing biological hypotheses or generating new ones and allow control and variation of parameters to discover general principles (Long, 2012; Aguilar et al., 2016; Aydin et al., 2019; Gravish and Lauder, 2018). In addition, they enact the laws of physics instead of those prescribed by a model (Long, 2012).Finally, physical principles and predictive models (Dickinson, Lehmann, and Sane, 1999; Blickhan and Full, 1993; Lauder and Drucker, 2002; Li, Zhang, and Goldman, 2013)

from this empirical approach provide mechanistic explanations for animal locomotion (Dickinson, Lehmann, and Sane, 1999; Kuo, 2007; Daley and Biewener, 2006; Birn-Jeffery et al., 2014; Lauder and Drucker, 2002) and design tools and action strategies for robots (Teoh and Wood, 2013; Shrivastava et al., 2020; Zhu et al., 2019; Li et al., 2009; Marvi et al., 2014).

Inspired by these successes, we will adopt a similar integrative approach by integrating biological, robotic, and physics studies of beam traversal and self-righting to understand how locomotor transitions emerge from physical interaction of animals and robots with their environment.

1.4.2 Rationale for studying physical interaction of animals and robots with enviornment

Locomotion in biological systems emerges (Dickinson et al., 2000; Anderson, 1972) not just from physical interaction with the environment; animals can also sense and adjust their mechanical interaction in response to the sensed information via feedback, both neural and mechanical (Dickinson et al., 2000) (Figure 1.11). For example, when fetching balls, a dog adjusts its running speed and direction based on the sensory information from its eyes.

In this dissertation, I focus on understanding physical interaction, which will provide a foundation for understanding sensory feedback control. This approach is inspired from early studies of aerodynamics of passive airfoils (Cayley, 1876), and recent studies of using robotic physical models to understand animals (Koehl, 2003; Long, 2012; Ijspeert, 2014; Aguilar et al., 2016; Aydin et al., 2019; Gravish and Lauder, 2018). For example, although airfoils were extremely simplified models of bird wings, these studies provided physics insights about

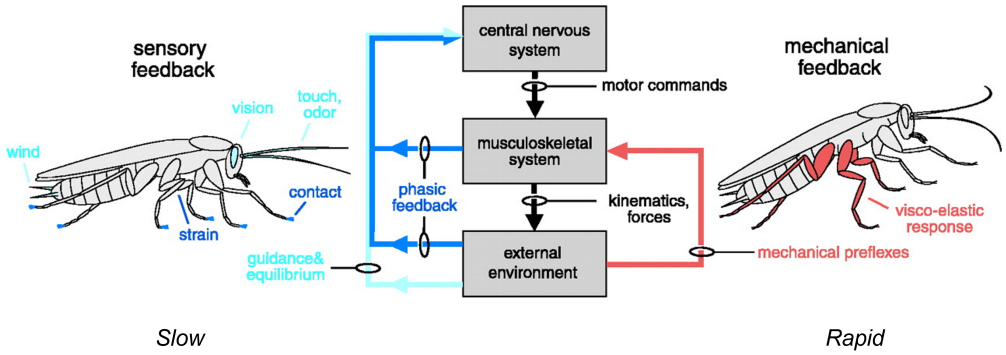

Figure 1.11: Neuromechanical feedback during locomotion. Neural sensory feedback (blue lines) is minimal during rapid bandwidth-limited locomotion. Image modified from Dickinson et al., 2000.

flight control, which were lacking in detailed anatomical studies and observation of birds at the time (Lindhe Norberg, 2002). Similarly, over the last three decades, such an approach of studying simplified physical models of physical interaction in air (Ellington et al., 1996; Dickinson, Lehmann, and Sane, 1999), water (Koehl, 2003; Ijspeert, 2008; Lauder, Flammang, and Alben, 2012), flat ground (Raibert, 1986), and flowable ground (Goldman, 2014; Aguilar et al., 2016; Aydin et al., 2019) has advanced our understanding of animals and robot locomotion (Dickinson et al., 2000).

Inspired by the success of this approach in previous studies, we follow a similar approach here by studying not just the animal, but also its simplified robotic model and comparing them to gain physical insights and develop physics models (Long, 2012; Ijspeert, 2014; Aguilar et al., 2016; Aydin et al., 2019). To make meaningful comparison with the feedforward-controlled robots with no sensory feedback, we study locomotor transitions of the animal during escape and self-righting emergency responses, where there is significant bandwidth limit on

sensory feedback (Sponberg and Full, 2008) due to delays in neuronal transmission (Figure 1.11). Finally, to begin to quantify sensory feedback and physical interaction over large spatiotemporal scales, we develop methods to track and reconstruct the motion of cockroach body and antennae using a previously developed terrain treadmill.

1.5 Organization of Chapters

- Chapter 2 details the biological, robotic, and physics studies of physical interaction during beam traversal.
- Chapter 3 details the biological, robotic, and physics studies of physical interaction during self-righting on flat ground.
- Chapter 4 describes methods to track and analyze animal kinematics during movement on a terrain treadmill over large spatiotemporal scales.
- Chapter 5 summarize the research results reported in Chapters 2-4 and their implications and possible future directions.

Chapter 2

Kinetic energy fluctuation from oscillatory self-propulsion facilitates barrier-crossing locomotor transitions during beam traversal

This chapter is a published paper by Ratan Othayoth, George Thoms, and Chen Li in *The Proceedings of the National Academy of Sciences* (2020) (Othayoth, Thoms, and Li, 2020).

2.1 Summary

Effective locomotion in nature happens by transitioning across multiple modes of locomotion such as walking, running, and climbing). Despite this, far more of our mechanistic understanding of terrestrial locomotion has been on how to generate and stabilize around near-steady-state movement in a single mode. We still know little about how locomotor transitions emerge from physical interaction with complex terrain. Consequently, mobile robots largely rely on

geometric maps to avoid obstacles, not traverse them. Recent studies revealed that locomotor transitions in complex 3-D terrain occur probabilistically via multiple pathways (Li et al., 2015). Here, we show that an energy landscape approach elucidates the underlying physical principles. We discovered that locomotor transitions of animals and robots self-propelled through complex 3-D terrain correspond to barrier-crossing transitions on a potential energy landscape. Locomotor modes are attracted to landscape basins separated by potential energy barriers. Kinetic energy fluctuation from oscillatory self-propulsion helps the system stochastically escape from one basin and reach another to make transitions. System's escape from a landscape basin is more likely towards lower barrier direction. These principles are surprisingly similar to those of near-equilibrium, microscopic systems. Analogous to free energy landscapes for multi-pathway protein folding transitions, our energy landscape approach from first principles is the beginning of a statistical physics theory of multi-pathway locomotor transitions in complex terrain. This will not only help understand how the organization of animal behavior emerges from multi-scale interactions between their neural and mechanical systems and the physical environment, but also guide robot design, control, and planning over the large, intractable locomotor-terrain parameter space to generate robust locomotor transitions through the real world.

2.2 Author contributions

Ratan Othayoth designed study, developed robotic physical model, performed animal and robot experiments, analyzed data, developed energy landscape model,

wrote and revised the paper; George Thoms developed robotic physical model and performed preliminary robot experiments; Chen Li designed and oversaw study, defined analyses, and wrote and revised the paper.

2.3 Introduction

To move about in the environment, animals can use many modes of locomotion (e.g., walk, run, crawl, climb, fly, swim, jump, burrow) (Alexander, 2006; Biewener, 2003; Dickinson et al., 2000) and must often transition across them (Lock, Burgess, and Vaidyanathan, 2013; Low et al., 2015) (e.g., Figure 1.2A). Despite this, far more of our mechanistic understanding of terrestrial locomotion has been on how animals generate (Blickhan and Full, 1993; Goldman et al., 2006; Hu et al., 2009; Kuo, 2007; Li, Hsieh, and Goldman, 2012) and stabilize (Biewener and Daley, 2007; Couzin-Fuchs et al., 2015; Revzen et al., 2013) steady-state, limit-cycle-like locomotion using a single mode.

Recent studies begin to reveal how terrestrial animals transition across locomotor modes in complex environments. Locomotor mode transitions, like other animal behavior, emerge from multi-scale interactions of the animal and external environment across the neural, postural, navigational, and ecological levels (Berman, 2018; Brown and Bivort, 2018; Nathan et al., 2008). At the neural level, terrestrial animals can use central pattern generators (Ijspeert, 2008) and sensory information (Blaesing, 2004; Kohlsdorf and Biewener, 2006; Ritzmann et al., 2012) to switch locomotor modes to traverse different media or overcome obstacles. At the ecological level, terrestrial animals foraging across natural landscapes switch locomotor modes to minimize metabolic cost (Shepard et al., 2013). At the intermediate level, terrestrial animals also transition between walking and running to save energy (Bramble and Lieberman, 2004). However, there remains a knowledge gap in how locomotor transitions in complex terrain emerge from direct physical interaction (i.e., terradynamics (Li, Zhang, and

Goldman, 2013)) of an animal's body and appendages with the environment. In particular, we lack theoretical concepts for thinking about how to generate and control locomotor transitions in complex terrain that are on the same level of limit cycles for single-mode locomotion (Holmes et al., 2006). For example, locomotion in irregular terrain with repeated perturbations is rarely near steady state and requires an animal to continually modify its behavior, which cannot be well described by limit cycles (Spagna et al., 2007; Sponberg and Full, 2008).

Understanding of how to make use of physical interaction with complex terrain (environmental affordance (Gibson, 2014; Roberts, Koditschek, and Miracchi, 2020)) to generate and control locomotor transitions is also critical to advancing mobile robotics. Similar to personal computers decades ago, mobile robots are on the verge of becoming a part of society. Some robots (e.g., robot vacuums, self-driving cars) already excel at navigating flat surfaces, by transitioning across driving modes (e.g., forward drive, U-turn, stop, park (Thrun, 2010)) to avoid sparse obstacles using a geometric map of the environment (Latombe, 2012). However, many critical applications, such as search and rescue in rubble, inspection and monitoring in buildings, extraterrestrial exploration through rocks, and even drug delivery inside a human body, require robots to transition across diverse locomotor modes to traverse unavoidable obstacles in complex terrain (Hu et al., 2018; Lock, Burgess, and Vaidyanathan, 2013; Low et al., 2015) (Figure 1.2B)). Yet, terrestrial robots still struggle to do so robustly (Guizzo and Ackerman, 2015), because we do not understand well how locomotor transitions (or lack thereof) emerge from physical interaction with complex terrain.

Our study is motivated by recent observations in a model system of insects

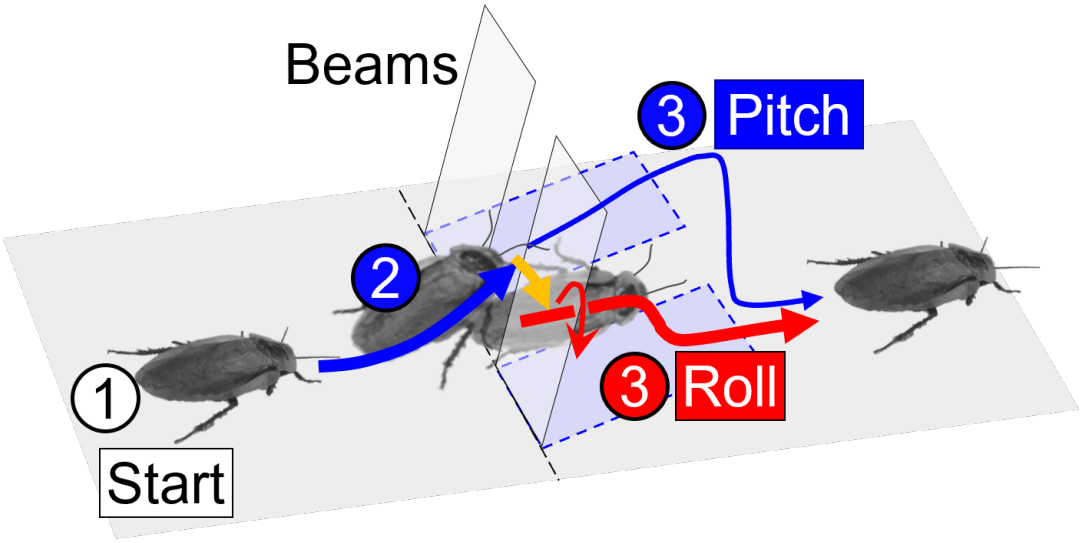

Figure 2.1: A cockroach transitioning (orange arrow) from pitch to roll mode to traverse grass-like beam obstacles.Reproduced from Othayoth, Thoms, and Li, 2020.

traversing complex 3-D terrain. The discoid cockroach, native to rainforest floor, can traverse flexible, grass-like beam obstacles using many locomotor modes, stochastically transitioning across them via multiple pathways (Li et al., 2015). For simplicity, hereafter we focus on the transition between two modes. The animal often first pushes against the beams, and beam elastic restoring forces lead the animal body to pitch up (Figure 2.1), blue). After this, though, the animal rarely pushes across (3% probability) but often rolls (Figure 2.1), red) to maneuver through beam gaps (45% probability). We define these as "pitch" and "roll" modes. Note that we use "locomotor mode" here in the general sense, not confined to limit-cycle locomotor behavior. The pitch mode is more challenging than the roll mode because the animal has to lift its weight and deflect the beams more (this is only true when beams are stiff, though; see Results). Thus, the animal appears to statistically transition from less to more

favorable modes. In addition, the animal's body oscillates as its legs continually push against the ground when trying to traverse. Besides in obstacle traversal, similar multi-pathway locomotor transitions, preference of some modes over others, and seemingly wasteful body oscillation were observed in self-righting of insects (Li et al., 2019).

In the field of protein folding, adopting a statistical physics view and using an energy landscape approach led researchers to recognize that proteins fold via multiple pathways and understand the physical principles (Dill et al., 2008; Onuchic and Wolynes, 2004; Wales, 2003). These near-equilibrium, microscopic systems statistically transition from higher to lower energy states (local minima) on a free energy landscape (increasing thermodynamic favorability). Thermal fluctuation helps the system stochastically cross energy barriers at transition states (saddle points between local minimum basins). These physical principles operating on a rugged landscape leads to the multi-pathway protein folding transitions. Inspired by the seeming similarities of our system to them, we contend that an energy landscape approach helps understand how self-propelled, far-from-equilibrium macroscopic animals' and robots' probabilistic locomotor transitions in complex 3-D terrain emerge from physical interaction, whose equations of motion are unknown or intractable (Aguilar and Goldman, 2016; Han et al., 2021). Specifically, we hypothesize that:

1. The self-propelled system's state is attracted to a local minimum basin on a potential energy landscape; locomotor transition from one mode to another can be viewed as the system state escaping from one basin and settling into another. (What governs transition?)

2. When it is comparable to the potential barrier, kinetic energy fluctuation from oscillatory self-propulsion helps the system escape from a landscape basin to make locomotor transitions. (When does transition happen?)

3. Escape from a basin is more likely towards a direction along which the escape barrier is lower. (How does transition happen?)

To begin to establish an energy landscape approach of locomotor transitions across modes in complex 3-D terrain, we tested these hypotheses for the two representative modes (pitch and roll) of the model body-beam interaction system defined above. Although the previous study introduced an early energy landscape model to qualitatively explain why locomotor shape affected physical interaction and thus locomotion (Li et al., 2015), none of these hypotheses were proposed or tested. We emphasize that our potential energy landscape directly arises from locomotor-terrain interaction physics using first principles. This is unlike artificially defined potential functions to explain walk-to-run transition (Diedrich and Warren, 1995) and other non-equilibrium biological phase transitions (Kelso, 2012), or metabolic energy landscapes inferred from oxygen consumption measurements to explain behavioral switching of locomotor modes (Shepard et al., 2013).

Because animal locomotion emerges from complex interactions of neural and physical mechanisms (Dickinson et al., 2000), to observe the outcome of pure physical interaction, we developed and tested a minimalistic robotic physical model (Figure 2.2)) with feedforward control. The robot had an ellipsoid-like body that was propelled forward at a constant speed and was free to pitch and roll (achieved through a gimbal mechanism) in response to interaction with two

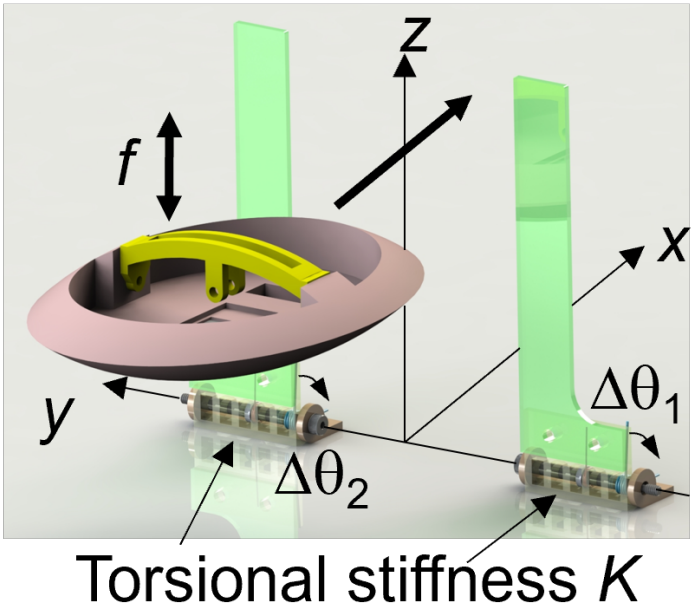

Figure 2.2: Robotic physical model. Reproduced from Othayoth, Thoms, and Li, 2020.

beams. The body was constrained not to yaw or move laterally to simplify energy landscape modeling. We also performed experiments with the discoid cockroach traversing beams during escape response to study how physical interaction affects the animal's locomotor transitions when neural control is bandwidth limited (Dickinson et al., 2000). Comparison of robot and animal observations can reveal aspects of the transitions that likely involve neural mechanisms.

To test the first hypothesis, in both robot and animal experiments, we used rigid "beams" with torsional joints at the base (Figures 2.3,2.4,2.5,2.6) as one-degree-of-freedom 3-D terrain components to generate a simple potential energy landscape. We then reconstructed the potential energy landscape and 3-D motion of the robot or animal body and beams in high accuracy (as opposed to

visual examination reported in the previous study (Li et al., 2015)) (Figures 2.14, 2.15) for the entire traversal. This allowed us to quantify how the system state behaved on the landscape during each observed locomotor mode and transition between modes. To test the second hypothesis, for the robot, we applied controlled oscillation with variable frequency f to vary kinetic energy fluctuation (Figure 2.10). Because we could not vary the animal's naturally occurring body oscillation, in animal experiments we changed the barrier relative to kinetic energy oscillation by varying beam torsional joint stiffness K by over an order of magnitude in the range of natural flexible terrain elements (Table **??**). K was also varied by over an order of magnitude for robot experiments and, together with animal experiments, helped elucidate how transition depended on terrain properties. Because the potential energy landscape consists of not only beam elastic energy but also body and beam gravitational energy, variation of K also changed how escape barrier compared in different directions, allowing the third hypothesis to be tested. See Methods and Supplementary Methods for technical detail and Table 2.1 for sample sizes.

2.4 Methods

2.4.1 Robotic physical model

To approximate the body shape of the discoid cockroach (Li et al., 2015), we 3-D printed an ellipsoid-like body, PLA plastic using UPBOX+, Tiertime, CA, USA), whose top and bottom halves were slices of an ellipsoid. The body was suspended (center of mass at 10 cm above the ground) via a custom gimbal mechanism that allowed free body pitching and rolling (Figure 2.3A). We added mass to the body so that it is bottom heavy, with body center of mass at 1.1 cm below the pitch axis and 1.6 cm below the roll axis. Body pitch and roll at static equilibrium for a freely suspended body without beam contact were near zero (pitch = $3.3^\circ \pm 0.4^\circ$, roll = $1.7^\circ \pm 0.8^\circ$; note that positive pitch is pitching downward). See Table 2.1 for geometric dimensions and physical properties of the body.

We used a linear actuator (Firgelli FA-HF-100-12-12, Firgelli Automation, WA, USA) to propel the body forward towards the obstacles. To introduce body kinetic energy fluctuation, we oscillated the body vertically using two DC servo motors (XM430-W350T, Dynamixel, CA, USA) via a five-bar linkage mechanism 3-D printed from PLA plastic (UPBOX+, Tiertime, CA, USA). We varied kinetic energy fluctuation by varying oscillation frequency. Our preliminary experiments showed that body oscillation along different directions did not qualitatively affect the outcome. Thus, we chose vertical oscillation to better observe response in body pitch and roll.

The body oscillated vertically along the following triangular wave trajectory

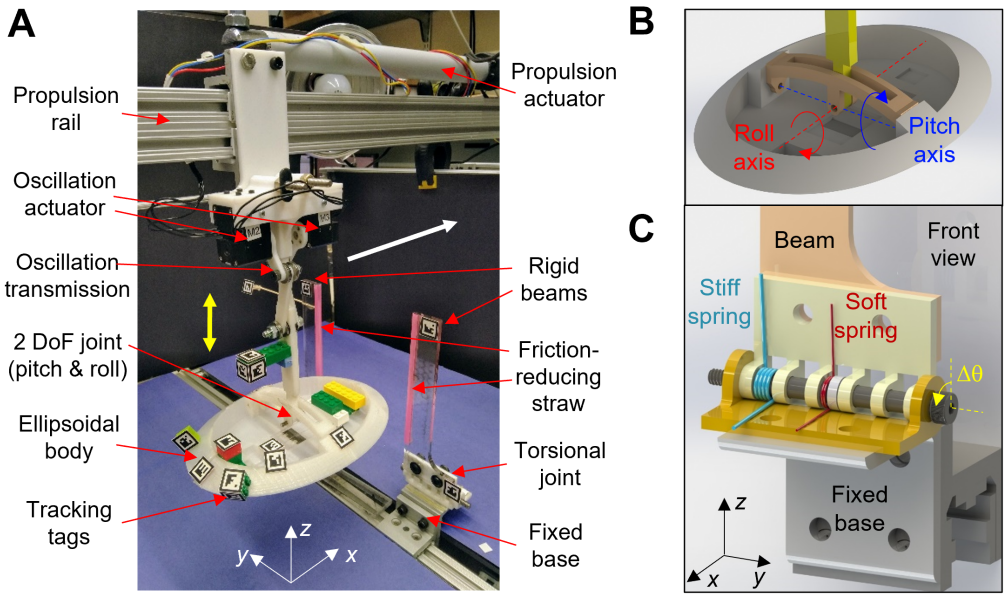

Figure 2.3: Design of robotic physical model and rigid beams with torsional springs at base. (A) Photo of robot body and beams. Body is propelled forward at a constant speed (white arrow) and can be oscillated vertically (yellow arrows). Body can freely pitch and roll in response to interaction with beams. (B) CAD model of body, showing design of pitch and roll joints and axes. Body center of mass is below geometric center due to added weight. Pitch (blue) and roll (red) axes cross geometric center. (C) CAD model of beam base, showing design of torsional joint. Rigid beams rotate about an axis parallel to y-axis (yellow arrow). K is varied by using different combinations of soft (red) and stiff (cyan) springs. Reproduced from Othayoth, Thoms, and Li, 2020.

(fitted from the measured z position):

$$z = z_0 + Aft + N(\mu, \sigma), \qquad 0 \leq t \leq \frac{T}{2} \tag{2.1}$$

$$z = z_0 + A(1 - ft) + N(\mu, \sigma), \qquad \frac{T}{2} < t \leq T \tag{2.2}$$

where z is the vertical position of the body geometric center, f is vertical oscillation frequency, $T = 1/f$ is vertical oscillation period, $A = 23.4$ mm is the vertical oscillation amplitude, and $z_0 = 102.4$ mm is the average vertical position when there is no oscillation. To prevent the body from being stuck against beams due to friction, we added a small noise, N, which is normally distributed with a mean of $\mu = 0.7$ mm and a standard deviation of $\sigma = 1.2$ mm. Kinetic energy fluctuation from this noise was small compared to that from the vertical oscillation. The vertical oscillation induced small lateral oscillation (12% of vertical oscillation amplitude). The motor angles were commanded using a microcontroller (Open CM 0.94, Robotis, CA, USA). We note that the animal's body oscillation is much more complex, variable, and less periodic than the robot's. It was difficult to use a wave oscillation with well-defined amplitude and frequency to approximate it.

Table 2.1: Geometric dimensions, physical properties, and sample sizes for animal and robot experiments.

		Animal						**Robot**				
	Number of Individuals	6						N/A				
Body	Mass m_{body} (g)	2.6 ± 0.3						233				
	Length (cm)	5.3 ± 0.1						22.1				
	Width (cm)	2.4 ± 0.1						15.8				
	Thickness (cm)	0.8 ± 0.1						5.8				
Beam	Lateral spacing(cm)	1.0						12.7				
	Width (cm)	1.0						2.8				
	Mass m_{beam} (g)		0.33	0.42	0.63	0.70	1.03		38			
	Inner layer thickness (mm)		0.04	0.05	0.07	0.10	0.25		N/A			
	Total thickness (mm)		0.54	0.55	0.72	0.75	0.85		6			
	Length L (cm)		5.7	8.8	8.7	8.6	9.3		18			
	Torsional stiffness K (mN·m/rad)		0.1	0.2	0.7	1.7	11.4		28	55	255	344
Sample size	No. of trials	Ind. 1	11	10	9	11	10	0 Hz	10	10	10	10
		Ind. 2	10	10	10	7	10	1 Hz	10	10	10	10
		Ind. 3	11	10	10	11	11	2 Hz	10	10	10	10
		Ind. 4	13	10	11	11	13	3 Hz	10	10	10	10
		Ind. 5	10	10	10	12	10	4 Hz	10	10	10	10
		Ind. 6	9	10	10	10	10	5 Hz	10	10	10	10
		Total	64	60	60	62	64	6 Hz	10	10	10	10
	Total no. of trials	310						280				

All data averages are mean ± s.d. m_{beam} is the mass of one beam.

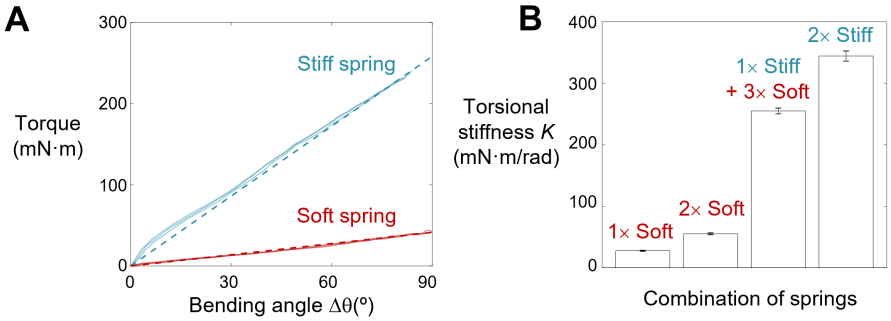

Figure 2.4: Robot beam stiffness characterization. Beam restoring torque as a function of bending angle $\Delta\theta$(defined in Figure 2.3C). Red and cyan curves are data for soft and stiff spring. Dashed lines are linear fits (through the origin) of data of each K, whose slope give K. (B) K for different combinations of springs used (mean $\pm$ s.d., $n = 3$ springs, 3 loading cycles each). Reproduced from Othayoth, Thoms, and Li, 2020.

2.4.2 Robot beam obstacles

For robot experiments, we mounted two rigid acrylic plates to a fixed base (Figure 2.3A) vertically using 3-D printed joints with torsional springs (Figure 2.3). We varied K by using different combinations of soft and stiff torsional springs (McMaster Carr, NJ) (Figure 2.3C, red and cyan) in parallel. The rigid beams were laser cut from acrylic plates (VLS60, Universal Laser & McMaster-Carr, NJ, USA). We covered the beam edges using smooth plastic straw (6 mm diameter) to reduce friction between them and the body during interaction.

We characterized torsional stiffness of the stiff and soft torsional springs by measuring the restoring torque about the torsional joint as a function of joint deflection angle (Figure 2.4A) using a 3-axis force sensor (Optoforce OMD-20-FG, OnRobot, Denmark). Torsional stiffness was calculated from the slope of the linear fit (across the origin) of torque as a function of deflection angle (Figure

2.4B). By combining the stiff and soft torsional springs, we varied K by over an order of magnitude ([28, 55, 255, 344] mN·m/rad). See Table 2.1 for geometric dimensions and physical properties of the beams.

2.4.3 Robot experiment imaging

Robot experiments were recorded using three synchronized high-speed cameras (IL5, Fastec Imaging, San Diego, CA) at 200 frames s^{-1} and a resolution of 1920 × 1080 pixels. To automatically track the body and beams over the entire range of rotation, we attached BEEtags (Crall et al., 2015) (18 mm × 18 mm) on the body (9 markers), vertical oscillation transmission (3 markers), right beam (2 markers), and left beam (5 markers). We used FasMotion software (Fastec Imaging, San Diego, CA) to save the videos to storage drives after recording for tracking and processing.

2.4.4 Robot experiment protocol

Before each trial, the body was positioned at a distance of 11 cm from the beams, and the beams were set to be vertical. We started video recording and body oscillation (for $f > 0$), waited for 1 s, and then propelled the body forward at a constant speed of 0.7 cm·s^{-1} by a distance of 30 cm (maximum possible by the linear actuator). Body oscillation was applied (for $f > 0$) until the end of forward translation. After forward translation completed, we stopped body oscillation and video recording and moved the body to its initial position for the next trial.

At each K, we varied kinetic energy fluctuation by varying f from 0 Hz to 6 Hz with an increment of 1 Hz. At each K and each f, we performed 10 trials.

This resulted in a total of 280 trials, with 70 trials at each K across all f. See Table 2.1 for detailed sample size.

2.4.5 Animals

We chose to study the discoid cockroach, *Blaberus discoidalis*, because it dwells on the floor of tropical rainforests with dense vegetation and litter and excels at traversing complex terrain (Li et al., 2015). We used adult male discoid cockroaches (Pinellas County Reptiles, St Petersburg, FL, USA), as females are often gravid and under different load bearing conditions. Prior to experiments, we kept the cockroaches in individual plastic containers at room temperature (24 °C) on a 12h:12h light:dark cycle. See Table 2.1 for dimensions and mass of the animals tested.

2.4.6 Animal beam obstacles

We custom made rigid "beams" with torsional springs at the base (Figure 2.5A). For each beam, we sandwiched a flexible layer between two stiff layers and exposed a small portion of the flexible layer (Figure 2.5B), which acted as torsional spring joint about which the beams deflect in the $x - z$ plane. We varied the thickness of the flexible layer ([0.04, 0.05, 0.07, 0.10, 0.25] mm) to vary the torsional stiffness K of the torsional joint by over two orders of magnitude ([0.1, 0.2, 0.7, 1.7, 11.4] mN·m/rad) in a similar range as natural obstacles like leaves, stalks, and grass. Polyethylene terephthalate plastic (McMaster Carr, NJ, USA) and cardstock (0.2 mm thickness, Neenah Inc., GA, USA) were used for the flexible and stiff layers and bonded using thermally bonding glue (Therm-O-Web, IL, USA) and a laminating machine (AmazonBasics, Amazon). The layer of

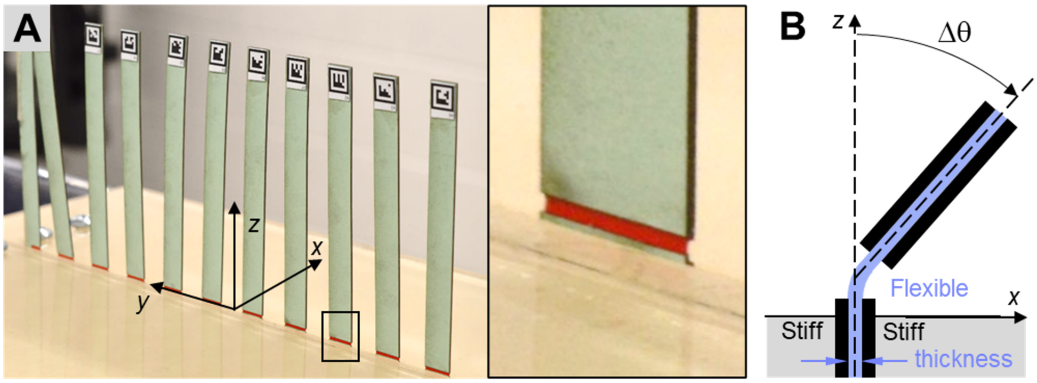

Figure 2.5: Design of rigid beams with torsional springs at base for animal experiments.(A) Photo of a layer of animal beams. Inset shows a closer view of torsional joint. (B) Side view schematic of beam design following (Haldane et al., 2015). Stiff outer layers (black) provide rigidity, and a small exposed section of flexible inner layer (blue) acts as a torsional spring joint. Dimensions not true to scale. Reproduced from Othayoth, Thoms, and Li, 2020.

10 beams was laser cut (VLS60, Universal Laser Systems, AZ, USA) to have identical geometry and spacing.

We characterized K by measuring the restoring torque about the torsional joint as a function of beam deflection angle (Figure 2.6A) using a 6-axis force and torque sensor (Nano 43, ATI Industrial Automation, NC, USA). K was calculated from the slope of the linear fit (across the origin) of torque as a function of deflection angle (Figure 2.6B). See Table 2.1 for geometric dimensions and physical properties of the beams.

2.4.7 Animal multi-camera imaging arena

We constructed an arena for animal experiments to measure locomotor transitions (Figure 2.7). Previous studies showed that animals often laterally explored beam obstacles before traversing (Li et al., 2015). To increase experimental yield, we used 10 identical beams in an obstacle layer, which presented nine

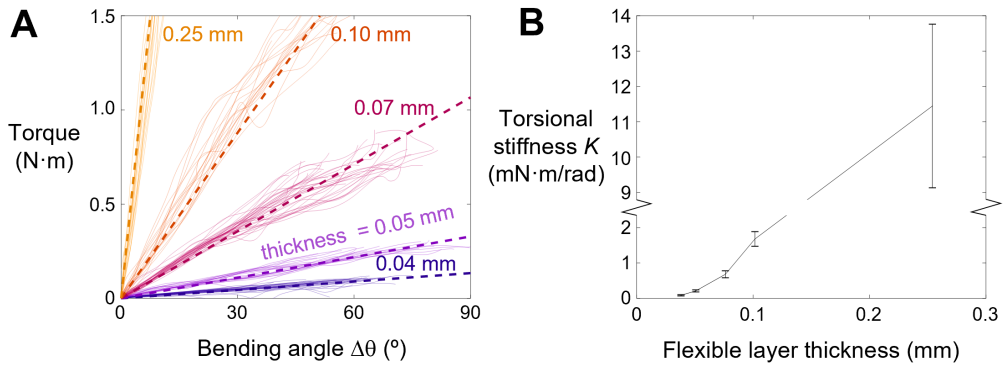

Figure 2.6: Characterization of rigid beams with torsional springs at base for animal experiments. (A) Beam restoring torque as a function of bending angle for different flexible layer thickness ([0.04, 0.05 0.07, 0.10, 0.25] mm). Dashed lines are linear fits (through the origin) of data, whose slopes give K. (B) K as a function of flexible layer thickness (mean ± s.d., n = 62, 37, 76, 38, 32 loading cycles). Reproduced from Othayoth, Thoms, and Li, 2020.

gaps of 1 cm (narrower than animal body width of 2.4 cm, but larger than body thickness of 0.8 cm) for the animal to traverse. All the beams were vertical without external force from the animal. The beam obstacle layer was inserted into a slit cut in the flat ground between two transparent sidewalls made of acrylic sheets. A runway funneled the animal towards the middle of beam obstacle layer to minimize the interaction with the sidewall. To facilitate traversal with minimal body yaw (on average), we arranged the beam obstacle layer to be perpendicular to the direction of animal movement. The reduced body yaw allowed us to more accurately visualize how trials evolved on the potential energy landscape (see section below), which was calculated using the average body yaw from all trials. Paper cardstock covered the ground surface. We placed a dark shelter with food and water on the exit side of the obstacle layer for the animal to rest after each trial.

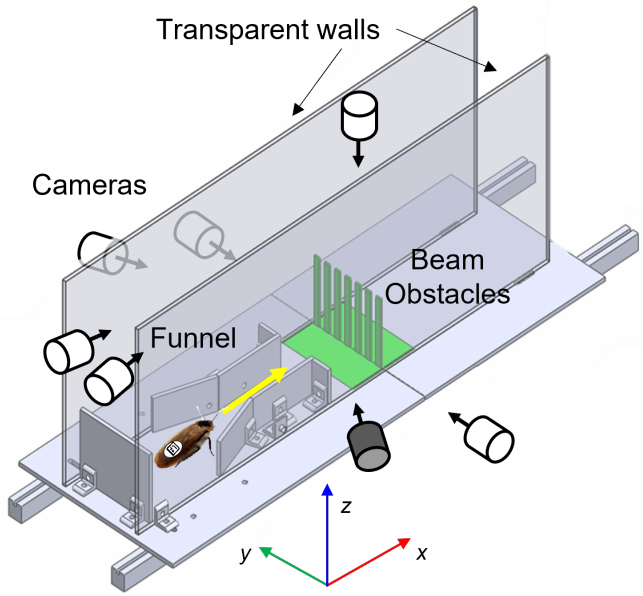

Figure 2.7: Animal locomotion arena with a layer of beam obstacles (green), with seven high-speed cameras. x, y,z axes show lab frame. Reproduced from Othayoth, Thoms, and Li, 2020. CAD model courtesy of Yaqing Wang.

Animal experiments were recorded using seven synchronized high-speed cameras (N5A-100, Adimec, Netherlands) at 100 frames s^{-1} and a resolution of 2592 $\times$ 2048 pixels. When interacting with the obstacles, animal body orientation varied substantially. We carefully positioned the cameras around the entire arena to cover the entire rotation range of motion, with two from back views, two side views, two isometric views, and one top view (Figure 2.7A). We used the StreamPix software (Norpix Inc., Montreal, Canada) to automatically save the videos to storage drives as they were being recorded, after which they were converted to AVI format for tracking and processing.

To automatically track the animal and beams, we attached a 7 mm $\times$ 7 mm BEEtag (Crall et al., 2015) to the animal body and 9 mm $\times$ 9 mm BEEtags to the top and bottom ends of both sides of each beam (Figure 2.8). The

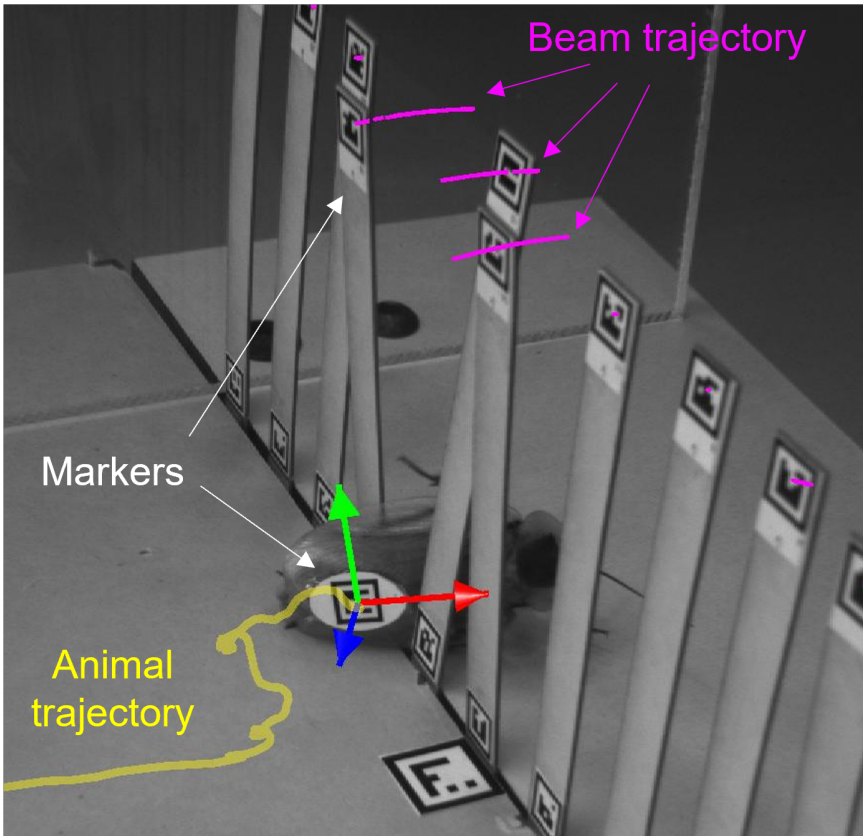

Figure 2.8: Snapshot of animal traversing beam obstacles (view from the shaded camera in Figure 2.7). Markers are attached to the animal body and beams to track their 3-D motion (yellow and magenta trajectories). Red, green, blue axes show body frame attached to markers. Reproduced from Othayoth, Thoms, and Li, 2020.

animal BEEtag was much lighter (< 0.15 g) than the animal itself (2.6 g). It was printed onto a rounded oval cardboard to minimize interference with the obstacle traversal and attached to the dorsal surface of the abdomen using ultraviolet curing glue (Bondic, Aurora, Canada).

2.4.8 Animal experiment protocol

Before the experiment, the arena was illuminated and heated to about 43°C with six work lamps (Coleman Cable, Waukegan, IL, USA). Before each trial, the animal was placed in the starting end of the arena and allowed to settle down. We then started video recording and probed the animal with a stick with a soft tip (made from paper tapes) to induce it to run towards the obstacles. The animal did not always immediately traverse after running into beam obstacles. Instead, it often made multiple failed attempts to traverse and sometimes explored the obstacle layer laterally to attempt traversing at different beam gaps, before eventually traversing. Once the animal traversed and reached the shelter, we stopped video recording and allowed the animal to rest for $\sim$10 minutes before the next trial.

We tested six animal individuals and beams of five different torsional stiffness K and collected a total of 337 trials. The same six individuals were tested across all K. We discarded trials in which any of the following were observed: (1) the animal did not move within 10 s after it was probed; (2) the animal moved back to the starting area or did not attempt to traverse; (3) the animal used the sidewall to traverse; or (4) the animal climbed up the beams and its body and all six legs lost contact with the ground. This resulted in a total of 310 accepted trials, with approximately 10 trials for each animal at each K. See Table 2.1 for detailed sample size.

2.4.9 High accuracy 3-D motion reconstruction

To calibrate the cameras over the working space for 3-D motion reconstruction, for both robot and animal experiments, we built a calibration object with multiple markers (47 for robot and 17 for animal) using Lego bricks (The Lego Group, Denmark). We then used the direct linear transformation software DLTcal5 (Hedrick, 2008) to obtain intrinsic and extrinsic camera parameters. We used a custom MATLAB script to automatically track 2-D coordinates of the markers in each camera view using the BEEtag code (Crall et al., 2015).

Using the tracked 2-D marker coordinates from multiple camera views and camera calibration parameters, we obtained the 3-D position of the four corners of each BEEtag markers using the direct linear transformation software DLTdv5 (Hedrick, 2008) , which was then used to obtain the marker frame (Figure 2.8). For the animal, we translated and rotated the marker frame by the measured translational (Δx = 10 mm, Δy = -0.2 mm, Δz = -3 mm) and rotational (roll = $0°$, pitch = $10°$, yaw = $1°$) offsets to obtain 3-D position and orientation of the body frame at the body geometric center, which nearly overlapped with body center of mass (Kram, Wong, and Full, 1997). For the robot, we used a CAD model of the body to determine the location of center of mass relative to the markers fixed to the body. Depending on which body markers were reconstructed in each video frame, we translated and rotated the reconstructed marker frame by its measured translational and rotational offsets to obtain 3-D position and orientation of the body frame at the center of mass. For both the robot and animal, we used Euler angles (yaw α, pitch β, and roll γ, $Z-Y'-X$" Tait-Bryan convention) to define 3-D rotation. Note that with this convention,

when the body pitches upward, pitch angle is negative.

To quantify the accuracy of 3-D reconstruction using BEEtag tracking combined with Direct Linear Transformation, we 3-D printed a high-precision calibration object. The calibration object had nine BEEtag markers mounted on a horizontal plate in a 3 $\times$ 3 grid with a 7 cm grid distance, each oriented at a pitch and yaw angle of 0°, 30°, and 60°. We measured the 3-D position and orientation of each marker from 3-D reconstruction (described above) and compared them to the designed values. This demonstrated that our imaging setup achieved high accuracy in 3-D position and orientation reconstruction (s.d. of position error = 0.6 mm; s.d. of orientation error = 1.1°). We also verified that lens distortion was minimal ($< 1\%$) using the checkboard distortion measurement method.

For each trial, we calculated body translational (v_x, v_y, v_z) and rotational (ω_α, ω_β, ω_γ) velocities and beam deflection angles from vertical ($\Delta\theta_i$) as a function of time. Beam angle was averaged from visible tags on each beam. Considering lateral symmetry, to simplify analysis of the roll mode, we flipped all trials in which the body rolled left to rolling right. For the animal, we offset the measured lateral positions (y) of each trial so that $y = 0$ in the middle of the gap that the animal traversed during the final, successful attempt.

2.4.10 Definition of pitch and roll modes and pitch-to-roll transition

We defined the robot to be in the roll mode if both beams lost contact with the body and bounced back to vertical before the distal end of the body crossed the beams ($x = 0$), and we defined it to be in the pitch mode otherwise. For

the robot, body motion was highly repeatable from trial to trial, and pitch-to-roll transition always resulted in a sharp decrease in system potential energy. Thus, we defined transition to occur when system potential energy reached a peak value (Figure 2.9E, vertical dashed line (*ii*)), after which it immediately reduced.

We defined the animal to be in the roll mode if its body roll (absolute value) exceeded 62°, because from system geometry this was the minimal roll for the body to move through the gap between two adjacent beams without deflecting them. The animal was defined to be in pitch mode otherwise. For trials in which the animal transitioned from the pitch to roll mode, we defined transitions to occur when body roll (absolute value) exceeded 20° (Figure 2.9B, vertical dashed line (*ii*)). We verified that system potential energy (Figure 2.9F) decreased at this moment. See Section 2.4.14 for details of computing potential energy.

2.4.11 Data averaging

Because the robot was propelled forward at a constant speed, its 3-D kinematics, potential energy, and kinetic energy were a function of body forward position x. To obtain average 3-D kinematics and potential energy as a function of x, we interpolated the measured position, orientation, and potential energy over x and then averaged them across all trials at a given K. For the robot, we averaged lateral position y and body yaw α for all the trials at each K for each x and used this average trajectory of measured x, y, and α to calculate an average potential energy landscape. For the animal, because of the high variability in y and α, for simplicity we set both y and α to zero when calculating the average potential energy landscape at each x.

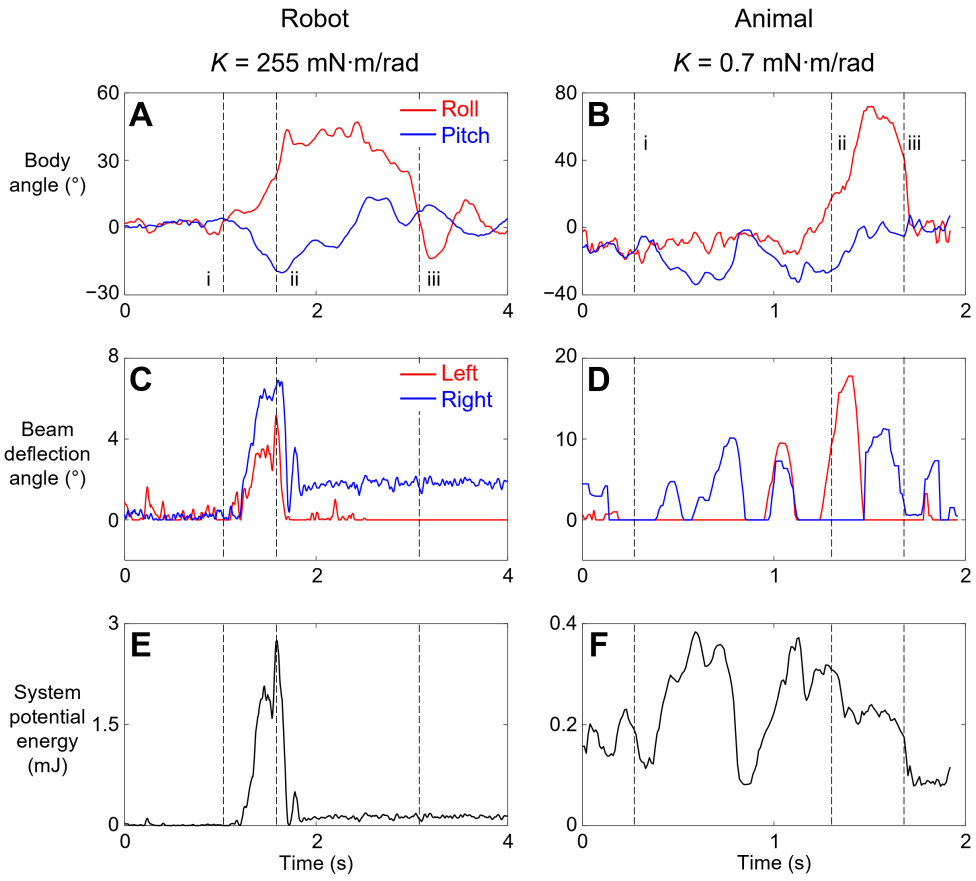

Figure 2.9: Representative motion of body and beams and system potential energy during interaction and definition of traversal and pitch-to-roll transition. (A, B) Body roll (red) and pitch (blue) as a function of time. (C, D) Left (red) and right (blue) beam deflection angle as a function of time. (E, F) System potential energy as a function of time. Data shown for a representative pitch-to-roll transition at K = 255 mN·m/rad for robot and K = 0.7 mN·m/rad for animal. For both the robot and animal, pitch-to-roll transition resulted in a reduction in system potential energy. Note that negative pitch is the body pitching head-up. Dashed lines (i) and (ii) are when body first contacts beams and when pitch-to-roll transition occurs. Dashed line (iii) is when the robot's forward translation ends and when animal's distal end crosses the beam (x = 0). For details of computing system potential energy, see Section 2.4.14. Reproduced from Othayoth, Thoms, and Li, 2020.

Because we focused on the pitch-to-roll transition (see definition in the next section), we considered only the animal's final, successful attempt in which such a transition may occur. For the final, successful attempt, we analyzed the portion of the trial starting from five frames (0.05 s) before the animal's head contacted the beams (Figure 2.9, dashed vertical line (*i*)) to ten frames (0.1 s) after the entire body crossed the obstacle layer (at $x = 0$, Figure 2.9, dashed vertical line (*iii*)). Because the robot body was translated with a constant forward speed and always crossed the beams, for it we analyzed the portion of the trial starting from when the body first contacted the beams (Figure 2.9, dashed vertical line (*i*)) until the end of forward translation (Figure 2.9, dashed vertical line (*iii*)).

2.4.12 Kinetic energy fluctuation

For both the robot and animal, we defined body kinetic energy fluctuation as the sum of kinetic energy due to translational and rotational velocity components other than forward motion of the body (v_y, v_z, ω_α, ω_β, ω_γ). To calculate moment of inertia, we approximated the animal body as an ellipsoid with uniform mass distribution, considering that legs only consist less than 15% of total mass (Kram, Wong, and Full, 1997). For the robot, we calculated moment of inertia from a CAD model of the body with accurate geometry and mass distribution.

For both the robot and animal, we calculated average kinetic energy fluctuation from first beam contact (of the final successful attempt of each trial for the animal) to when transition occurred using the trials in which the body transitioned to the roll mode. This was because for the trials in which the body was trapped in the pitch mode, it was difficult to define the onset of pitching as

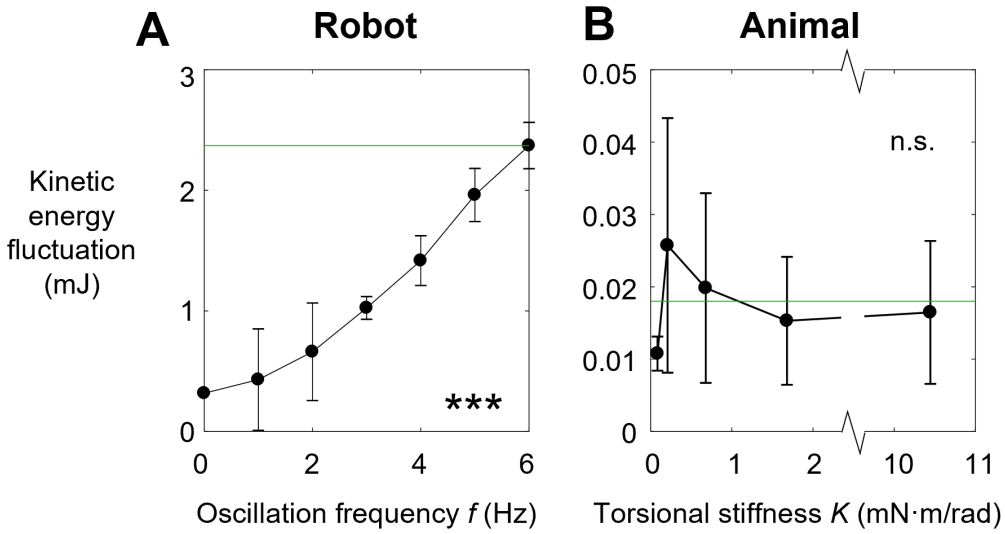

Figure 2.10: Kinetic energy fluctuation. (A) Kinetic energy fluctuation of robot as function of f. *** indicates a significant dependence (ANOVA, $P < 0.0001$, $F = 520.99$). (B) Kinetic energy fluctuation of animal as function of K. n.s. indicate no significant difference (ANOVA, $P = 0.3835$, $F = 0.9047$). See Table 2.1 for sample size. Reproduced from Othayoth, Thoms, and Li, 2020.

can be readily done for the onset of rolling. Including these trials would add the substantial kinetic energy of continuous body pitching that resulted from the interaction, which was not part of the fluctuation that induced the transition. We verified that kinetic energy fluctuation differed little between before contact with the beams and from first contact to when transition occurred. We then averaged kinetic energy fluctuation over time for each trial, from when the body first contacted a beam (Figure 2.9, dashed line (i)) (in the final successful attempt of each trial for the animal), to when it transitioned to roll mode (Figure 2.9, dashed line (ii)). For the robot, we then averaged these trial averages across all trials at each f in which the robot transitioned to the roll mode to obtain

average kinetic energy fluctuation at each f (Figure 2.10A). For the animal, we averaged these trial averages across all trials at each K to obtain average kinetic energy fluctuation at each K (Figure 2.10B).

2.4.13 Statistics

All probabilities were calculated relative to the total number of accepted trials of each treatment. All average data are reported as mean ± s.d. For the robot, we used a chi-square test to test whether pitch-to-roll transition probability depended on K, with K and f as fixed factors. For the animal, we used a chi-square test to test whether pitch-to-roll transition probability depended on K, with K and individual as fixed factors and including their crossed effect. For the robot, we used an ANOVA to test whether kinetic energy fluctuation increased with f. To test whether the animal's kinetic energy fluctuation depended on K, we pooled data from all the trials in which pitch-to-roll transition occurred (see section above for explanation) for each K and performed a mixed-effect ANOVA with K as a fixed factor and individual as a random factor. We used a Student's t-test to test whether the robot's system state was attracted to the basin corresponding to the measured mode in all trials. All statistical tests were performed using JMP Pro 13 (SAS Institute Inc., NC, USA).

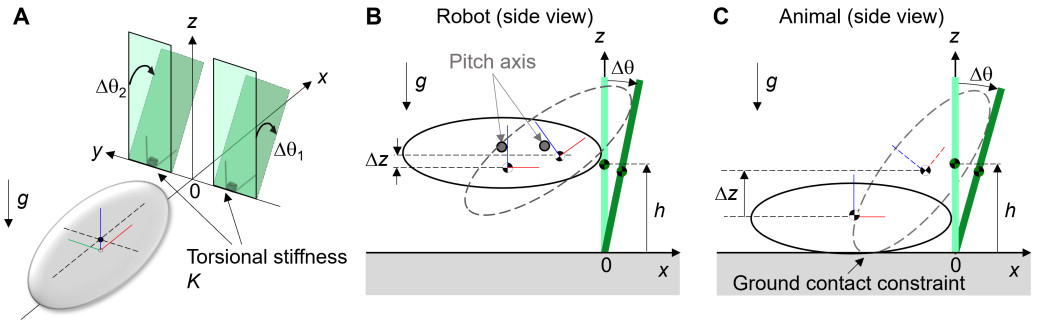

Figure 2.11: Potential energy landscape model, with definition of variables and parameters. (A) Oblique view schematic of body (a rigid ellipsoid) and beams (rigid rectangular plates with torsional joints at base) of torsional stiffness K. Without body contact, both beams are vertical (light green). With body contact, beams are deflected forward (dark green) by angles $\Delta\theta_{1,2}$. (B, C) Side view of model for robot (B) and animal (C) to show center of mass height changes with body pitching and beam deflection. Solid and dashed ellipses show body in static equilibrium and pitched-up, respectively. Center of mass of body and beams are shown. Reproduced from Othayoth, Thoms, and Li, 2020.

2.4.14 Potential energy landscape

In energy landscape modeling, we approximated the animal body as a rigid ellipsoid and obtained the robot body shape from a CAD model used for 3-D printing the body. The beams were modeled as rigid rectangular plates on torsional joints (Figure 2.11A). Because the beams had a finite mass, forward deflection lowered beam center of mass and thus beam gravitational potential energy. Because the measured beam restoring torque was nearly proportional to deflection angle for both the robot (Figure 2.4B) and animal (Figure 2.6A), we approximated the torsional joint at the base of each beam as a perfect Hookean torsional spring and assumed that there was no damping. Because the body only pushed forward against the beams, in the model we only allowed forward beam deflection ($\Delta\theta_{1,2} \geq 0$).

For robot modeling, we set center of mass to be below the pitch and roll axes as measured (Figure 2.11B). For animal modeling, we constrained the lowest point of the body to always touch the ground (ground constraint, Figure 2.11C), because the animal maintained ground contact during traversal (we rejected trials in which the animal climbed onto the beams) and we neglected the animal's legs. Thus, for both the robot and animal, body pitching and rolling in response to interaction with the beams increased center of mass height and thus body gravitational potential energy. In addition, because the robot was suspended from and driven forward by a linear actuator, its center of mass height was constrained to move within a measured range of z = [9.9 cm, 11.8 cm]. Because the robot's controlled vertical oscillation was modeled as part of kinetic energy fluctuation, we used the average body center of mass vertical position before contacting the beams (z = 10.8 cm, vertical height constraint) to calculate its initial body potential energy. We verified that at any given x, landscape shape remained similar within the z range in which the robot was oscillated. For both the robot and animal, we offset system potential energy to zero when the body was not in contact with beams and in its static equilibrium (at zero pitch and zero roll) so system potential energy shown on the landscapes were relative to this initial equilibrium (2.11B, C).

The full potential energy landscape depended on body orientation (pitch, roll, yaw) and forward and lateral positions (x, y), given the vertical height and ground constraints on the robot and animal, respectively. Because we focused on body pitch and roll motions, for a given body position (x, y) and yaw, we varied body pitch and roll over [$-180°$, $180°$] to calculate system potential energy landscape over pitch-roll space. In Figures 2.13B, 2.14, 2.15A, and 2.17A,

we only show the landscape over a part of the entire pitch-roll space to better focus on the pitch and roll basins. We then calculated beam deflection due to body contact (only allowing $\Delta\theta_{1,2} \geq 0$) and center of mass height increase (Δz) to obtain system potential energy as below.

$$E = m_{body} g \Delta z + \frac{1}{2} m_{beam} g L (\cos \Delta\theta_1 + \cos \Delta\theta_2 - 2) + \frac{1}{2} K (\Delta\theta_1^2 + \Delta\theta_2^2) \quad (2.3)$$

where where m_{body} is body mass, g is gravitational acceleration, Δz is body center of mass height increase from its equilibrium configuration (at near zero pitch and zero roll), m_{beam} is beam mass, L is beam length, K is beam torsional stiffness, and $\Delta\theta_1$ and $\Delta\theta_2$ are beam deflection angles from vertical.

We note that our landscape did not model body-beam interaction after the beams bounced back.

2.4.15 Local minima and system state trajectories on potential energy landscape

For each forward position x of the body relative to the beams, we examined the landscape to determine the pitch and roll local minima and measured their potential energies. Note that for the robot their potential energies did not include height change due to controlled vertical oscillation (see section above). To visualize how the measured state of the system behaved on the landscape, we projected the measured body pitch and roll onto the landscape for each x (Figure 2.14A, 2.15, 2.17A, blue and red dots for trials in which the system was trapped in the pitch mode and transitioned to the roll mode), which formed a system state trajectory over time as traversal progressed. Note that only the end points of the trajectory, which represent the current state, showed

the actual potential energy of the system at the corresponding x. The rest of the visualized trajectory showed how body pitch and roll evolved but, for visualization purpose, was simply projected on the landscape surface. Because roll local minimum does not exist at $K = 28$ mN·m/rad for the robot, for comparison with other K, we defined it to be at (pitch, roll) = (0°, ±42°) based on the minimal body roll required to traverse without beam deflection.

2.4.16 Average potential energy landscape at each beam stiffness

To facilitate observation of statistical trends, we calculated the average potential energy landscape at each K and visualized all trials on it. Average landscape calculation used the average measured lateral position y and body yaw for each x. For the robot, this average potential energy landscape was a good approximation of the actual landscape for each trial, because the robot was constrained by design to have minimal lateral motion or yawing. Despite this, when projected onto the average potential energy landscape, in some trials at high K, a portion of the system state trajectory appeared to momentarily go out of the pitch basin and then re-entered it (Figure 2.15). This was an artifact from landscape averaging. In those trials, the robot body experienced larger yawing due to a slight lateral bending of the plastic pole that suspended the robot resulting from high beam restoring forces. Because such trials are rare in the robot experiment, the average landscape basin was close to that without body yawing. Examination of the actual landscape for each robot trial (see Section 2.4.17) verified that the state trajectory in the pitch mode was almost always in the pitch basin. For the animal that freely moved laterally and yawed, the average landscape was a

much poorer approximation of the actual landscape for each trial.

2.4.17 Percentage of trials in which system is attracted to basin of observed mode on actual landscape

Because the average landscape did not account for trial-to-trial variation, to better quantify how well the potential energy landscape explained the observed locomotor modes, for both the robot and animal, we further calculated the actual (not averaged) potential energy landscape for each trial using the measured position (x, y) and body yaw of that trial. We then counted the number of trials in which the system state either stayed in the pitch basin or transitioned to the roll basin, in accord with the locomotor mode observed, and we calculated the percentage of trajectories attracted to the corresponding basin.

2.4.18 Energy barrier to escape from pitch local minimum

We measured the potential energy barrier that must be overcome to escape from the pitch local minimum. First, at each body forward position x, we considered imaginary straight paths away from the pitch local minimum (Figure 2.13B, *iii*, blue dot) in the full pitch-roll space ($[-180°, 180°]$), parameterized by an angle Ψ relative to the negative pitch direction (body pitched up). Along each imaginary straight path, we obtained a cross section of the potential energy landscape (Figure 2.13B, *iii*, inset). Then, we measured and defined the maximal increase in potential energy in the cross section as the escape barrier along this imaginary straight path, which was a function of Ψ, as shown by a

polar plot (Figure 2.15B). Then, we calculated how escape barrier along different directions away from pitch local minimum changed as traversal progressed (increasing x). We defined pitch-to-roll transition barrier as the lowest escape barrier, which occurred at the saddle point between pitch and roll basins. We measured how pitch-to-roll transition barrier and the location of saddle point in the pitch-roll space changed as x increased. For the robot, we calculated pitch-to-roll transition barrier using the average landscape at each K. For the animal, we used the average landscape with zero average lateral position and body yaw for simplicity, considering its large trial-to-trial variation in lateral position and body yaw.

2.4.19 Robot system state velocity directions

To measure the direction towards which the robot state trajectory was moving in the pitch-roll space during transition, for each trial, we calculated the velocity vector of the state trajectory in the pitch-roll space from the measured body roll and pitch, low-pass filtered data using a sixth order Butterworth filter. Then, we calculated the polar angle of this velocity vector relative to the pitch-roll axes of the landscape. To focus on the transition, for each trial in which pitch-to-roll transition occurred, we only considered the portion of the trial occurring over the x range from start of beam contact to the onset of transition (Figure 2.9, vertical dashed lines (i)-(ii)). For trials in which pitch-to-roll transition did not occur, we considered the portion of the trial within the average x range where transition was observed at higher K ($x = [-69, -39]$ mm). For each K, we pooled data of trials in which the system was trapped in the pitch mode and those in which the system transitioned to the roll mode to calculate their

respective distribution (polar histogram) of velocity directions (Figure 2.15D, blue and red). We also measured the directions of the saddle point between the pitch and roll basins and the local maximum along the pitch-up and pitch-down directions, averaged over the x range in which transition was observed (Figure 2.15D, yellow and gray dashed lines).

2.4.20 Animal active body and limb adjustments

We observed high speed videos of animal experiments to search for evidence of the animal using active adjustments to make transition. For each K, we counted the percentage of trials in which the animal repeatedly flexed its head relative to the body, differentially used its hind legs, or did both (Wang, Othayoth, and Li, 2021).

2.5 Results

Before encountering the beams, both the robot and animal moved forward with a near horizontal body posture. After beam contact, both the robot and animal started traversing by pushing against the beams, with the body pitched up. As beam stiffness K increased, pitch-to-roll transition probability increased for both the robot and animal (Figure 2.12; $P < 0.0001$, mixed-design chi-squared test). At low beam torsional stiffness K, neither transitioned to the roll mode even with body oscillation. At the highest beam torsional stiffness K, both always transitioned, except for the robot without oscillation. In addition, for the robot at high K (255 mN·m/rad), pitch-to-roll transition probability increased with oscillation frequency f (Figure 2.12B) and thus with kinetic energy fluctuation (Figure 2.10A). At the highest K tested (344 mN·m/rad), pitch-to-roll transition probability reached one for all $f > 0$ tested. For simplicity, below we first describe robot results followed by animal results.

We tested the first hypothesis–i.e, the self-propelled system state is attracted to local minimum basins on a potential energy landscape–by reconstructing the robot's potential energy landscape and evaluating how its system state behaved on the landscape (Figure 2.13). Using the measured physical and geometric parameters of the body and beams, we calculated the robot's system potential energy (sum of body and beam gravitational energy and beam elastic energy) as a function of body pitch, roll, and forward position x relative to the beams. For simplicity, we first examine results at $K = 255$ mN·m/rad. Before the body contacted the beams (Figure 2.13A, i), pitching or rolling increased body gravitational energy (because body center of mass was below rotation axes,

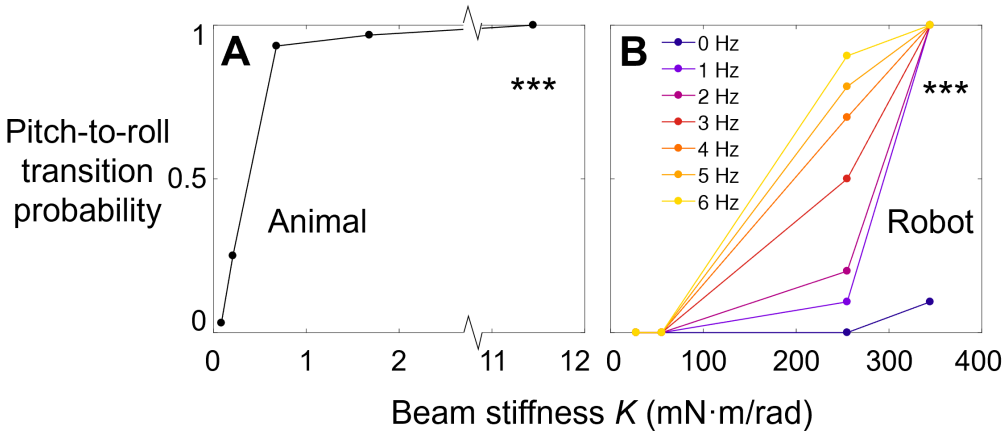

Figure 2.12: Pitch-to-roll transition probability of animal (A) and robot (B) as a function of beam stiffness K . For robot, we varied oscillation frequency f to vary kinetic energy fluctuation. *** indicates a significant dependence on K (animal: mixed-effects chi-squared test, $P < 0.0001$, $\chi^2 = 297.4$; robot: chi-squared test, P < 0.0001, $\chi^2 = 247.1$). $n = 64$, 60, 60, 62, 64 trials for animal and $n = 70$ trials at each K for robot. Reproduced from Othayoth, Thoms, and Li, 2020.

Figure 2.11). Thus, the potential energy landscape over body pitch-roll space had a global minimum at zero pitch and zero roll, i.e., when the body was horizontal (Figure 2.13B, i). As the body moved closer and interacted with the beams (Figure 2.13A, ii, iii), the global minimum evolved into a "pitch" local minimum at a finite pitch and zero roll (Figure 2.13B, ii, iii, blue). Meanwhile, two "roll" local minima emerged at near zero pitch and a finite positive or negative roll (Figure 2.13B, ii, iii, red, for rolling right or left), whose energies were lower than the pitch local minimum. Hereafter, we refer to these local minimum basins as pitch and roll basins [1].

[1] A fourth basin also emerged with its local minimum at a finite positive pitch and zero roll, corresponding to the body pitching down against the beams. However, such a configuration was never observed in the robot or animal.

We discovered that the robot's system state during the observed pitch and roll modes were attracted to the pitch and roll basins, respectively. When the body was far away from the beams, the system state in pitch and roll space settled to the global minimum of the landscape (Figure 2.13B, i). During beam interaction, without oscillation, the system state was trapped in the pitch basin, leading to the body pushing across the beams in a pitched-up orientation with little roll (Figures 2.13A, B, ii, iii). With oscillation, the system stochastically escaped from the pitch basin and crossed a potential energy barrier to reach the roll basin (Figure 2.13B, iii), thereby transitioning from the pitch to the roll mode (Figure 2.13B, ii, iii'). We examined system state trajectory on the landscape reconstructed for each trial. Whether the robot was trapped in the pitch mode (blue trajectories) or transitioned to the roll mode (red trajectories), its system state was attracted to the corresponding basin in nearly all trials (99%, not significantly different from 1, $P > 0.15$, Student's t-test, Figure 2.15A, iii). Because of this strong attraction, the measured system potential energy closely matched the observed mode basin's local minimum energy throughout traversal (Figure 2.16iii, solid vs. dashed curves). All these findings held true at other K (near 100%, Figures 2.15A, 2.16). Together, these robot results supported our first hypothesis that the self-propelled system's state is attracted to a local minimum basin on a potential energy landscape and that locomotor transition from one mode to another can be viewed as the system state escaping from one basin and settling into another.

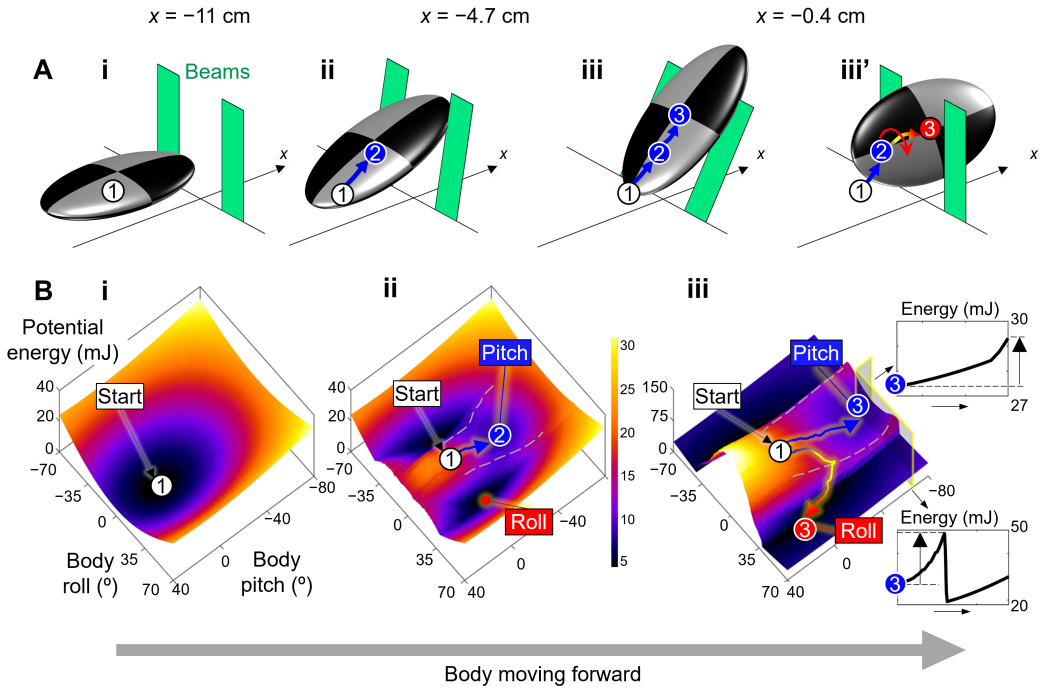

Figure 2.13: Robot locomotor transitions on a potential energy landscape. Results are shown at $K = 255$ mN·m/rad. (A) Snapshots of body before and during interaction with two beams in pitch (i, ii, iii) and roll (iii') modes. (B) Snapshots of landscape over body pitch-roll space before (i) and during (ii, iii) interaction. Representative system state trajectories are shown for being trapped in pitch basin (blue) and transitioning to roll basin (red). Insets in (iii) define potential energy barriers to escape from pitch local minimum in pitch-up and positive roll directions. Dashed gray curves on landscape show boundaries between pitch and roll basins. Note that landscape evolves as body moves forward (increasing x), and only part of landscape over pitch-roll space is shown to focus on pitch and roll basins. Reproduced from Othayoth, Thoms, and Li, 2020.

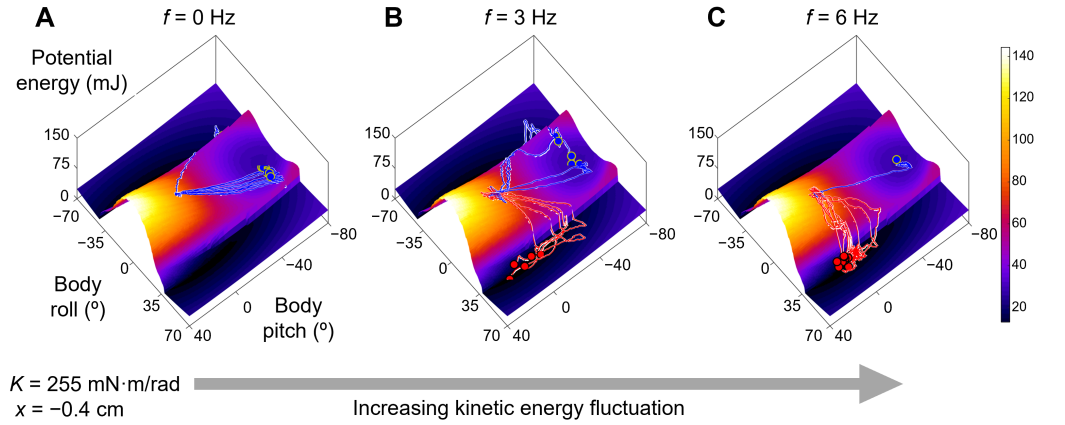

Figure 2.14: Robot locomotor transitions are stochastic and become more likely as kinetic energy fluctuation increases. Comparison of state trajectory ensemble on average landscape (snapshot at x = -0.4 cm) across oscillation frequencies: (A) f = 0 Hz; (B) f = 3 Hz; (C) f = 6 Hz. Results are shown at K = 255 mN·m/rad. Blue and red curves show trials trapped in pitch basin and transitioning to roll basin, respectively. Trials in which body rolls left are flipped to rolling right considering lateral symmetry. n = 10 trials at each f. Only part of landscape over pitch-roll space is shown to focus on pitch and roll basins. Blue trajectories exiting pitch basin is an artifact of landscape averaging. Reproduced from Othayoth, Thoms, and Li, 2020.

Next, we tested the second hypothesis that when comparable to the potential energy barrier, kinetic energy fluctuation from oscillatory self-propulsion helps the system escape from a landscape to make locomotor transitions. We first observed how kinetic energy fluctuation affected the robot's escape from a basin. Again, we examine results at K = 255 mN·m/rad first for simplicity. As f increased (which increased kinetic energy fluctuation), the system was more likely to escape from the pitch basin it was initially attracted to and reach the roll basin (Figure 2.14), resulting in more likely pitch-to-roll transitions (Figure 2.12B, K = 255 mN·m/rad).

Figure 2.15: Robot tends to transition to roll basin when kinetic energy fluctuation is comparable to potential energy barrier to escape pitch local minimum and towards direction of lower barrier. (A) Average potential energy landscape over pitch-roll space (snapshot at x = 8 mm) with ensemble of state trajectories. Blue and red curves show trials trapped in pitch basin and transitioning to roll basin, respectively. Note that landscape evolves as body moves forward (increasing x) and only part of the landscape over pitch-roll space is shown to focus on the pitch and roll basins. Top right number on each landscape shows percentage of trials in which system state is attracted to pitch/roll basin corresponding to observed mode. Blue trajectories exiting pitch basin is an artifact of landscape averaging. (B) Polar plot of potential energy barrier to escape from pitch local minimum (blue dot) along all directions in pitch-roll space (snapshot at x = -53 mm). Pitch-to-roll transition barrier is defined as minimal escape barrier (arrows in iv), which occurs at saddle point between pitch and roll basins (yellow dot). (C) Pitch-to-roll transition barrier as a function of x. Gray band shows x range in which pitch-to-roll transition is observed (mean ± s.d.). Green circle/line in B, D shows measured average kinetic energy fluctuation of 2.3 mJ at highest f = 6 Hz tested (Figure 2.10). (D) Probability distribution of state velocity directions in pitch-roll space in the x range where transition is observed (gray band in C). Blue and red are data from trials trapped in pitch basin and transitioning to roll basin, respectively. Trials in which body rolls left are flipped to rolling right considering lateral symmetry. Black dashed lines and gray shaded sectors show angular direction of maximal escape barriers (mean ± s.d) along pitch up and down directions. Yellow dashed line and shaded sector show angular direction of minimal escape barrier (mean ± s.d), which occurs at saddle point. Columns i-iv are at K = 28, 55, 255, and 344 mN·m/rad. Data shown in A, C and D are for all f tested (n = 70 trials) at each K. Reproduced from Othayoth, Thoms, and Li, 2020.

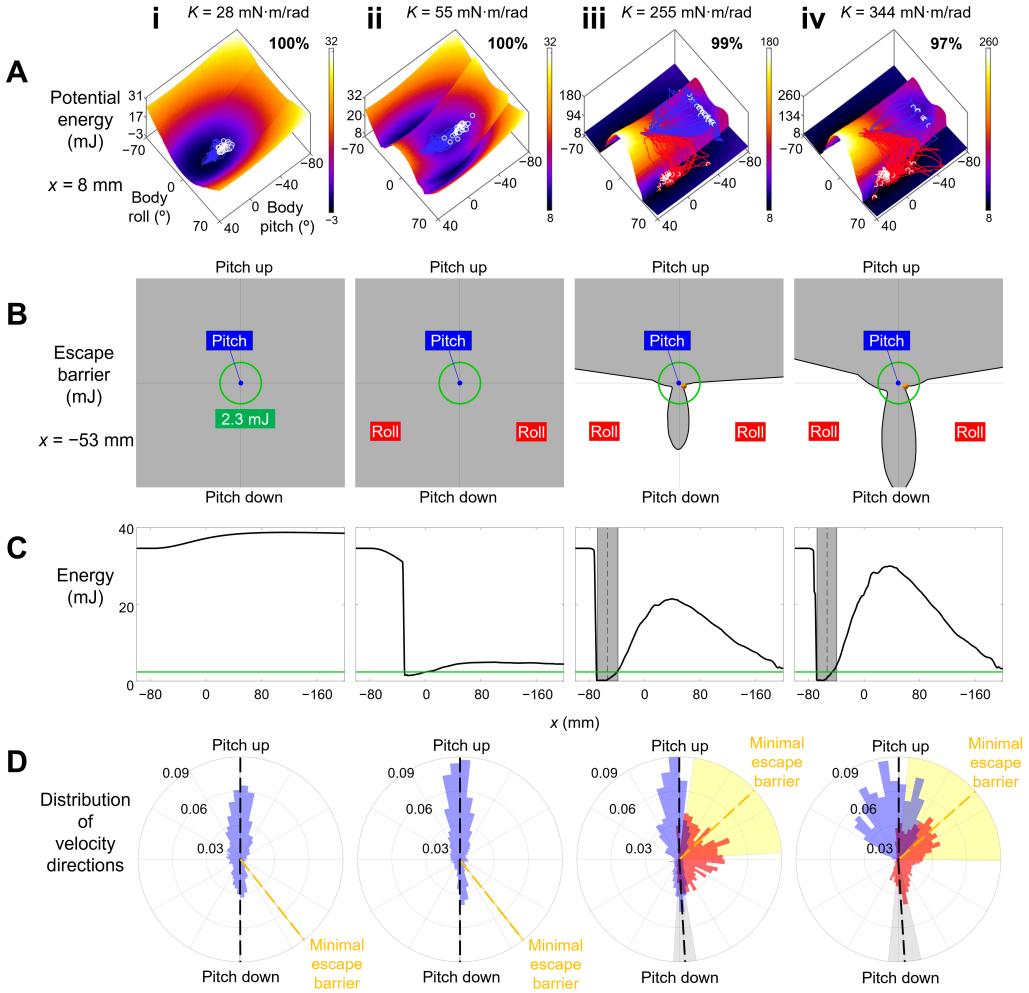
A
i
K = 28 mN·m/rad
100%
ii
K = 55 mN·m/rad
100%
iii
K = 255 mN·m/rad
99%
iv
K = 344 mN·m/rad
97%
Potential energy (mJ)
x = 8 mm
Body roll (°)
Body pitch (°)
B
Escape barrier (mJ)
x = −53 mm
Pitch up
Pitch down
Pitch
Roll
2.3 mJ
C
Energy (mJ)
x (mm)
D
Distribution of velocity directions
Minimal escape barrier

Then, we compared the minimal potential energy barrier to escape from the pitch local minimum with the average kinetic energy fluctuation at $f = 6$ Hz (Figure 2.15C, iii). The escape barrier depended on both towards which direction the system moved in the pitch-roll space (Figure 2.13B, iii, insets, Figure 2.15B, iii) and body forward position x relative to the beams (Figure 2.15C, iii). Minimal escape barrier occurred at the saddle point between the pitch and roll basins (Figure 2.15C, yellow dot), which we defined as pitch-to-roll transition barrier. Only within a small range of x was average kinetic energy fluctuation at $f = 6$ Hz (Figure 2.15C, iii, green) sufficient for overcoming pitch-to-roll transition barrier (Figure 2.15C, iii, black). This range matched remarkably well with the x range over which pitch-to-roll transition was observed with increasing likelihood with f (gray band showing mean $\pm$ s.d. from all trials across f). All these findings held true at $K = 344$ mN·m/rad. At $K = 28$ mN·m/rad, minimal escape barrier far exceeded kinetic energy fluctuation, consistent with the absence of transition. Together, these robot results supported our second hypothesis that when comparable to the potential energy barrier, kinetic energy fluctuation from oscillatory self-propulsion helps the system escape from a landscape to make locomotor transitions.

Finally, we tested the third hypothesis that escape from a basin is more likely towards a direction along which the escape barrier is lower, by examining the direction towards which the robot's system state moved during interaction. At each K, when the body was not in contact with the beams, the escape barrier was large along all directions in the pitch-roll space (e.g., x = -80 mm). As the body moved forward (increasing x), the escape barrier towards the direction of roll basins reduced drastically, becoming comparable to or even smaller than average kinetic energy fluctuation at f = 6 Hz (green circle) at the saddle point (yellow dot). By contrast, escape barrier in the direction of pitching up or down was always greater than average kinetic energy fluctuation (Figure 2.15B). Examination of how the system state moved on the landscape and probability distribution of system state velocity directions in the pitch-roll space (Figure 2.15D) showed that escape was more aligned with the direction of the saddle point between pitch and roll basins, i.e., escape was more likely towards the direction of lower barrier. This is intuitive because in other directions escape barrier was higher and often exceeded kinetic energy fluctuation. Together, these robot observations supported our third hypothesis.

Comparison of robot observations across K further suggested a concept of favorability for locomotor transitions. As K increased, pitch-to-roll transition became more likely (Figure 2.15A), saturating at one for all $f > 0$ tested at the highest K (Figure 2.12B). Intuitively, when the beams were flimsy, the body pushed across (trapped in the pitch mode) as if nothing were there; when the beams were rigid, the body could not push across and must roll. Thus, the likelihood of pitch-to-roll transition is positively correlated with how favorable transitioning to the roll mode is relative to staying in the pitch mode.

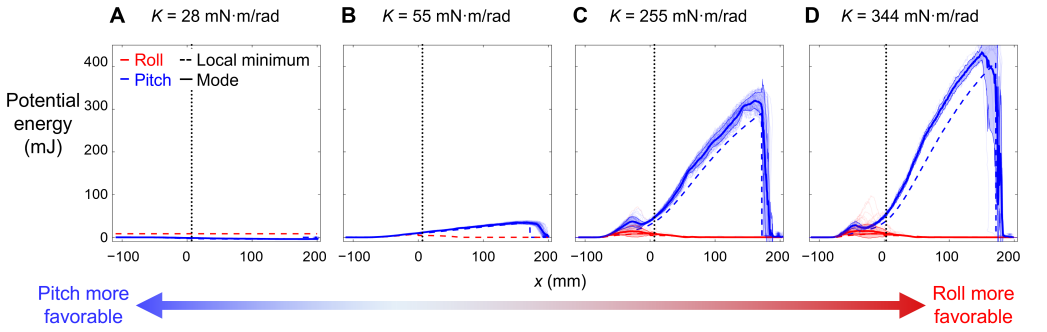

Figure 2.16: Favorability measure for robot. Potential energy of measured pitch and roll modes (solid, mean ± s.d.) and of pitch and roll local minima (dashed) as a function of x. Measured data are for all f tested ($n = 70$ trials) at each K. Blue and red show trials trapped in pitch basin and transitioning to roll basin, respectively. Columns i-iv are at $K = 28$, 55, 255, and 344 mN·m/rad. Dotted line at $x = 8$ mm shows location of snapshots in Figure 2.15A. Reproduced from Othayoth, Thoms, and Li, 2020.

To provide a measure of favorability, we compared whether the pitch or roll basin was lower during traversal, measured at their respective local minimum (Figure 2.16). At low K (28 mN·m/rad), the pitch basin remained the global minimum basin throughout traversal (Figure 2.16i), indicating that the pitch mode was more favorable. As K increased, the pitch basin became increasingly higher than the roll basin (Figure 2.16ii-iv), indicating that the roll mode became increasingly more favorable. At small $K = 55$ mN·m/rad for $x > 0$, although the roll mode was more favorable (Figure 2.16ii), kinetic energy fluctuation was smaller than the transition barrier (Figure 2.15C, ii); thus, transition did not occur (Figure 2.15A, ii). We emphasize that the negative correlation between the probability of staying in or transitioning to a mode and its relative basin height is only an emergent outcome of the transition physics. The passive robot does not directly feel how high or how low an adjacent basin is; whether it escapes and makes a transition only depends on the basin in which it currently

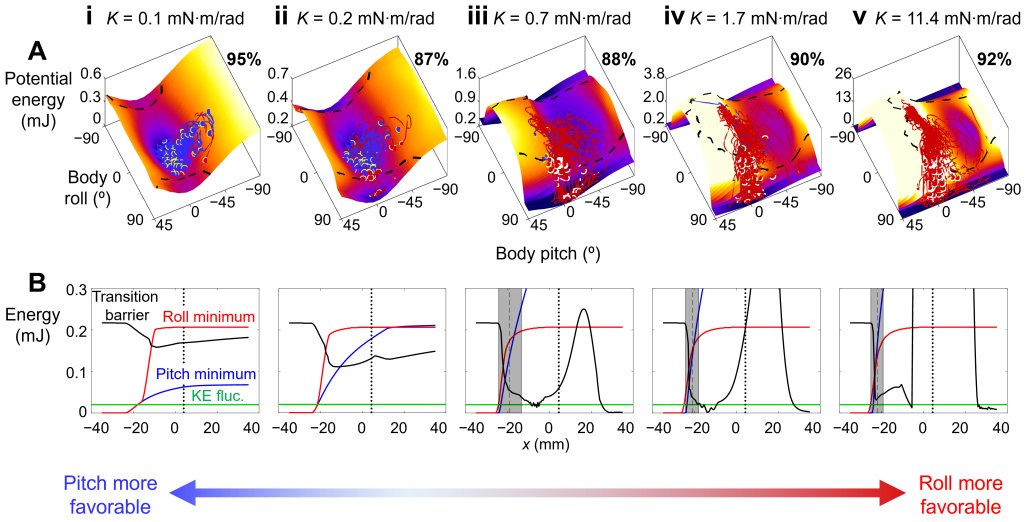

Figure 2.17: Animal tends to transition to roll basin when kinetic energy fluctuation is comparable to potential energy barrier to escape pitch basin and when roll basin is more favorable. (A) Potential energy landscape over pitch-roll space (snapshot at $x = 4$ mm, dotted lines in B) with ensemble of state trajectories. Dashed black curves on landscape show boundary of pitch basin. Note that landscape evolves as body moves forward (increasing x) and only part of landscape over pitch-roll space is shown to focus on pitch and roll basins. We set color map scale to saturate at high energy to highlight landscape basins. (B) Potential energy of pitch and roll local minima and pitch-to-roll transition barrier as a function of x. Green line is measured average kinetic energy fluctuation of 0.02 mJ. Columns i-v are at $K = 0.1$, 0.2, 0.7, 1.7, and 11.4 mN·m/rad ($n = 64$, 60, 60, 62, and 64 trials). Reproduced from Othayoth, Thoms, and Li, 2020.

resides. Exactly how favorability difference between basins emerges from the local dynamics of escaping from a basin remains to be understood.

Similar to the feedforward-controlled robot, the animal's system state during the observed pitch or roll mode was attracted to the corresponding basin of the potential energy landscape (Figure 2.17A, 90% of trials at all K). In addition, pitch-to-roll transition mostly occurred when both average kinetic energy fluctuation became comparable to transition barrier and the roll mode became

more favorable than the pitch mode (Figure 2.17B). These similar observations were remarkable because, for the animal that displayed larger lateral motion and yawing, leg motion, and individual variation, the landscape (which was averaged from all trials) provided a much coarser approximation of the system than for the simpler, well-controlled robot. These animal results supported our first and second hypotheses. We did not test the third hypothesis in the animal, considering that the measured system state velocity was noisy and the animal had higher lateral and yaw motion during traversal.

These results showed that physical interaction with the terrain also played a major role in the animal's probabilistic locomotor transitions, even when active behavior was likely at play. In some trials, the animal transitioned even when its average kinetic energy fluctuation was smaller than transition barrier (Figure 2.17B). In addition, the animal occasionally transitioned to the less favorable roll mode at low K (Figure 2.17A, i, ii, red trajectories). Further, the animal often flexed its head relative to the body and used the two hind legs differentially (Wang, Othayoth, and Li, 2021) during beam interaction (23%, 63%, 89%, 79%, and 85% of the trials at the five K's). All these were evidence that the animal's transition involved active behavior (see discussion). Unlike the robot that was pulled forward at a constant speed (pulling force always exceeded beam resistive force), the animal had a finite ability to push forward and may rely more on such active behavior to facilitate transition (Wang, Othayoth, and Li, 2021).

2.6 Discussion

In summary, using a transition between two representative modes in a model system, we demonstrated that an energy landscape approach helps understand how stochastic transitions of animals and robots across locomotor modes statistically emerge from physical interaction with complex 3-D terrain. We discovered that kinetic energy fluctuation from oscillatory self-propulsion helps the system cross barriers on a potential energy landscape to make locomotor transitions. This provided compelling evidence about why variation in movement can lead to stochastic outcome (Stephens et al., 2011) and can be advantageous when locomotor behavior is separated into distinct modes. This also explained early observations of surprising ability to traverse unstructured terrain of bandwidth-limited, rapid-running insects (Sponberg and Full, 2008) and feedforward-controlled legged robots (Altendorfer et al., 2001), as both have substantial body oscillation during locomotion. However, we view this way of "vibrate like a particle" as only one of a suite of transition strategies. Animals and robots may use other strategies to make transitions, such as plan anticipatory actions (Gart and Li, 2018) and use random search (Xuan and Li, 2020b) to overcome barriers, use sensory feedback adjustments to move towards lower barriers or reduce barriers (Wang, Othayoth, and Li, 2021), or even change morphology to modify landscape topology to introduce or eliminate certain modes (Han et al., 2021).

We posit that there is an "energy landscape dominated" regime of locomotion, where along certain directions there exist large potential energy barriers

that are comparable to or exceed kinetic energy and/or mechanical work generated by each propulsive cycle or motion. This may happen when propulsive forces are either limited by physiological, morphological, and environmental (e.g., low friction) constraints or do not well align with directions along which large barriers occur. In complex terrain with many large obstacles (Gart and Li, 2018; Han et al., 2021; Li et al., 2015; Wang, Othayoth, and Li, 2021) and even during strenuous maneuvers (Li et al., 2019; Othayoth and Li, 2021; Xuan and Li, 2020b; Xuan and Li, 2020a), these situations are frequent. In this regime, not only does energy landscape modeling provide a useful statistical physics approach for understanding locomotor transitions across modes, but it may also allow comparison across systems (different animal species, robots, terrain, and modes) to discover general physical principles. Outside of this regime, energy landscape modeling is not useful—for example, not for ballistic jumping over small obstacles with kinetic energy far exceeding potential energy barriers.

We discovered that distinct attractive basins of the potential energy landscape can lead to stereotyped locomotor modes and transitions in both the animal and feedforward-controlled robot. Because our potential energy landscape is directly derived from first principles (as opposed to fitting a model to behavioral data (Mearns et al., 2020; Stephens et al., 2008; Wiltschko et al., 2015), this result provided compelling evidence that behavioral stereotypy of animals emerges from their neural and mechanical systems directly interacting with the physical environment (Berman, 2018; Brown and Bivort, 2018). In addition, our approach should inform how direct physical interaction with the environment constrains behavioral hierarchy (Berman, 2018; Brown and Bivort, 2018). For example, for grass-like obstacle traversal, starting with our

coarse-grained landscape here resulting from a rigid body interacting with rigid "beams" on torsional springs, we can add degrees of freedom describing head flexion (Wang, Othayoth, and Li, 2021), body bending and twisting, articulated leg motions, and more realistic beam obstacles with cantilever bending and spatial heterogeneity. This will reveal more nuanced pathways of transitioning between fine-grained locomotor modes that have a variety of body and appendage configuration and terrain responses (e.g., flexing the head and tucking the legs to roll into the gap (Wang, Othayoth, and Li, 2021), separating beams laterally, etc.). Analyzing the disconnectivity (Wales, 2003) of basins of such a more complete, high-dimensional energy landscape will reveal the hierarchy ("treeness" (Berman, Bialek, and Shaevitz, 2016)) of locomotor modes in complex terrain.

2.6.1 Towards understanding emergent behaviour in natural environments

More broadly, these considerations suggest that our energy landscape approach provides a means towards first-principle, physical understanding of the organization of locomotor behavior, filling a critical knowledge gap. The field of movement ecology (Nathan et al., 2008) makes field observations of trajectories of animals as a point mass moving and making behavioral transitions in natural environments (e.g., (Suraci et al., 2019)), whose physical interactions are difficult to measure. Recent progress in quantitative ethology has advanced understanding of the organization of behavior (Berman, Bialek, and Shaevitz, 2016; Berman, 2018; Brown and Bivort, 2018; Mearns et al., 2020; Wiltschko et al., 2015), often by quantifying kinematics in homogeneous, near featureless

laboratory environments (Berman, Bialek, and Shaevitz, 2016; Cande et al., 2018; Mearns et al., 2020; Stephens et al., 2008). Our work highlights the importance and feasibility of, and opens new avenues for, studying how the organization of behavior is constrained by an animal's direct physical interaction with realistic environments (Li, Zhang, and Goldman, 2013). Doing so will help inform how animal behavior evolves in nature; it will also simplify robot design, control, and planning to generate robust locomotor transitions in complex terrain, which may be otherwise intractable in the large locomotor-terrain parameter space. This is analogous to rugged free energy landscapes allowing divide-and-conquer in protein folding (Dill and MacCallum, 2012).

Our empirically discovered physical principles of locomotor transitions are surprisingly similar to those of microscopic systems (Figure 2.18), especially multi-pathway protein folding transitions where predictive energy landscape theories have been very successful (Dill et al., 2008; Onuchic and Wolynes, 2004; Wales, 2003). Thus, we envision our energy landscape as the beginning of a statistical physics theory that will quantitatively predict global structures and emergent dynamics of multi-pathway locomotor transitions in the energy landscape dominated regime. An immediate next step towards this is to model conservative forces using potential energy landscape gradients and add stochastic, non-conservative propulsive and dissipative forces that perturb the system to "diffuse" across landscape barriers (analogous to (Bryngelson and Wolynes, 1989; Socci, Onuchic, and Wolynes, 1996)). Doing this may also elucidate how escape dynamics from a basin locally leads to emergent favorability difference between basins. These physical principles may help reveal how animals, and

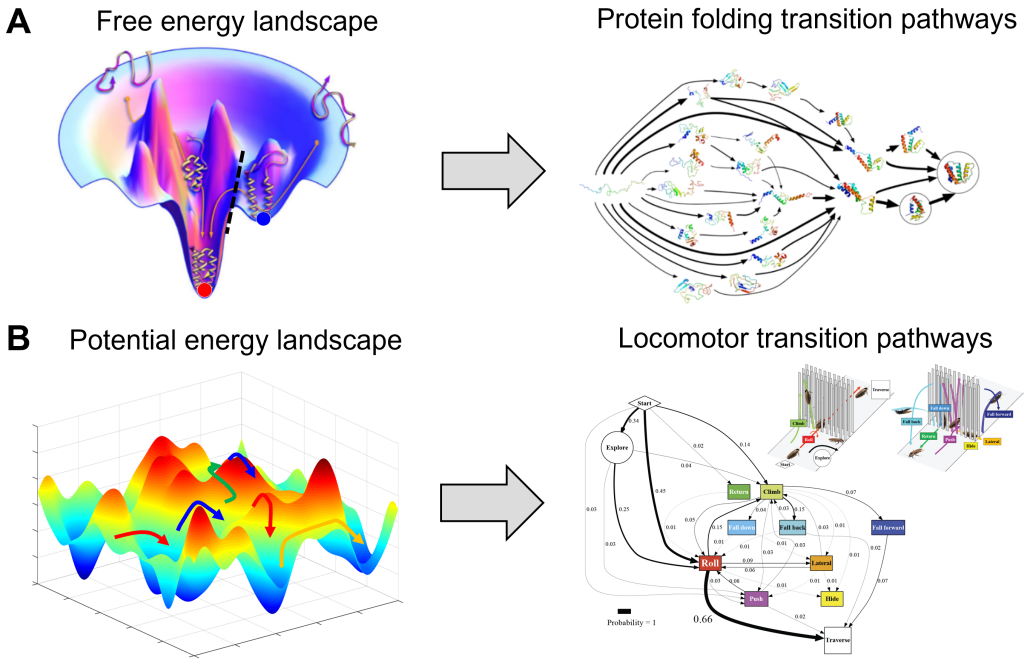

Figure 2.18: Comparison of energy landscape between protein-folding transitions and locomotor transition. (A) Energy landscape theories help understand physical principles and predict global structures and emergent properties of probabilistic protein folding transitions via multiple pathways. Image credits: A, left panel Reproduced from (Dill and MacCallum, 2012); A, right panel reproduced from (Voelz et al., 2012). (B) We envision energy landscape modeling as a beginning of a statistical physics approach for understanding and predicting probabilistic, multi-pathway locomotor transitions in complex terrain (Li et al., 2015). Reproduced from Othayoth, Thoms, and Li, 2020.

how robots should, use local force sensing to control motion to facilitate locomotor transitions on the landscape. Further, although it seems obvious that near-equilibrium statistical thermodynamics does not directly apply here, an energy landscape approach to locomotor transitions in complex terrain provides opportunities to test and develop new theories of few-body active matter (Savoie et al., 2019).

Finally, our energy landscape approach provides a conceptual way of thinking about locomotor modes beyond near-steady-state, limit-cycle-like behavior (e.g., walk, run, climb (Blickhan and Full, 1993; Goldman et al., 2006; Kuo, 2007)) by adding metastable behavior (Byl and Tedrake, 2009) locally attracted to landscape basins (e.g., pitch and roll modes here, which are far-from-steady maneuvers). We foresee the creation of new dynamical systems theories of terrestrial locomotion (Holmes et al., 2006) that produce transitions across locally attractive landscape basins as well as between limit-cycle attractors (Diederich, Schumm, and Cruse, 2002; Geyer, Seyfarth, and Blickhan, 2006). They will enable using physical interaction to design, control, and plan basins funneled into one another to compose (Burridge, Rizzi, and Koditschek, 1999) locomotor transitions to perform high-level tasks in the real world. Terradynamics of locomotor-terrain interaction starting from first principles (Li, Zhang, and Goldman, 2013) such as illustrated here will facilitate this progress.

Chapter 3

Propelling and perturbing appendages together facilitate strenuous ground self-righting

This chapter is a published paper by Ratan Othayoth and Chen Li in *eLife* (2021) (Othayoth and Li, 2021).

3.1 Summary

Terrestrial animals must self-right when overturned on the ground, but this locomotor task is strenuous. To do so, the discoid cockroach often pushes its wings against the ground to begin a somersault which rarely succeeds. As it repeatedly attempts this, the animal probabilistically rolls to the side to self-right. During winged self-righting, the animal flails its legs vigorously. Here, we studied whether wing opening and leg flailing together facilitate strenuous ground self-righting. Adding mass to increase hind leg flailing kinetic energy increased the animal's self-righting probability. We then developed a robot with similar strenuous self-righting behavior and used it as a physical model

for systematic experiments. The robot's self-righting probability increased with wing opening and leg flailing amplitudes. A potential energy landscape model revealed that, although wing opening did not generate sufficient kinetic energy to overcome the high pitch potential energy barrier to somersault, it reduced the barrier for rolling, facilitating the small kinetic energy from leg flailing to probabilistically overcome it to self-right. The model also revealed that the stereotyped body motion during self-righting emerged from physical interaction of the body and appendages with the ground. Our study demonstrated the usefulness of potential energy landscape for modeling self-righting transitions.

3.2 Author contributions

Ratan Othayoth designed robotic physical model, performed animal and robot experiments, analyzed and validated results, created visualizations, and wrote the manuscript. Chen Li conceived and designed study, supervised the project, obtained funding and reviewed and edited the manuscript. I acknowledge Qihan Xuan for preliminary potential energy landscape modelling of ground self-righting.

3.3 Introduction

Ground self-righting is a critical locomotor capability that animals must have to survive (for a review, see Li et al., 2019). The longer an animal is flipped over and stranded, the more susceptible it is to risks like predation, starvation, desiccation (Steyermark and Spotila, 2001), and limited mating success (Penn and Brockmann, 1995). Thus, it is crucial for animals to be able to self-right at a high probability because it can mean the difference between life or death. Similarly, ground self-righting is critical for the continuous operation of mobile robots (for a review, see Li et al., 2017).

Ground self-righting is a strenuous task. For example, to self-right, cockroaches must overcome potential energy barriers seven times greater than the mechanical energy required per stride for steady-state, medium speed running (8 body lengths s^{-1}) (Kram, Wong, and Full, 1997) or, exert ground reaction forces eight times greater than that during steady-state medium speed running (5 body lengths^{-1}) (Full, Yamauchi, and Jindrich, 1995). Often, animals struggle to self-right quickly and needs multiple attempts (Brackenbury, 1990; Domokos and Várkonyi, 2008; Hoffman, 1980; Koppányi and Kleitman, 1927; Li et al., 2019; Silvey, 1973) to self-right due to constraints from morphology, actuation, and the terrain (Domokos and Várkonyi, 2008; Faisal and Matheson, 2001; Golubović et al., 2017; Li et al., 2019; Steyermark and Spotila, 2001).

Ground self-righting has been studied in a diversity of animals, including insects (Brackenbury, 1990; Delcomyn, 1987; Faisal and Matheson, 2001; Frantsevich and Mokrushov, 1980; Li et al., 2019; Sherman, Novotny, and Camhi, 1977; Zill, 1986), crustaceans (Davis, 1968; Silvey, 1973) , mollusks (Hoffman,

1980; Weldon and Hoffman, 1979; Zhang et al., 2020), and vertebrates (Ashe, 1970; Bartholomew and Caswell, 1951; Creery and Bland, 1980; Domokos and Várkonyi, 2008; Golubović A, 2015; Koppányi and Kleitman, 1927; Malashichev, 2016; Pellis, Pellis, and Teitelbaum, 1991; Robins et al., 1998; Vince, 1986; Winters et al., 1986). A diversity of strategies have been described, including using appendages such as legs, wings, tail, and neck and deforming the body substantially. Often, rather than using a single type of appendages or just deforming the body without using appendages, animals use them together to propel and perturb the body to destabilize from the upside-down state (Brackenbury, 1990; Davis, 1968; Domokos and Várkonyi, 2008; Faisal and Matheson, 2001; Hoffman, 1980; Li et al., 2019). In particular, vigorous appendage flailing is a ubiquitous behavior observed across a diversity of species (Ashe, 1970; Brackenbury, 1990; Davis, 1968; Delcomyn, 1987; Domokos and Várkonyi, 2008; Faisal and Matheson, 2001; Hoffman, 1980; Kleitman and Koppanyi, 1926; Koppányi and Kleitman, 1927; Li et al., 2019; Zill, 1986). Some of these animals also use other appendages or the body to propel against the ground (Brackenbury, 1990; Davis, 1968; Domokos and Várkonyi, 2008; Faisal and Matheson, 2001; Hoffman, 1980; Li et al., 2019). Such vigorous appendage flailing, at a first glance appears to be wasteful.

Here, we study how propulsive and perturbing appendages together contribute to successful strenuous ground self-righting. Our model system is the discoid cockroach's strenuous ground self-righting using wings (Li et al., 2019)) (Figure 3.1). The overturned animal opens and pushes its wings against the ground in an attempt to self-right, resulting in its body pitching forward (Figure 3.1Ai). Because the two opened wings and head form a triangular base of

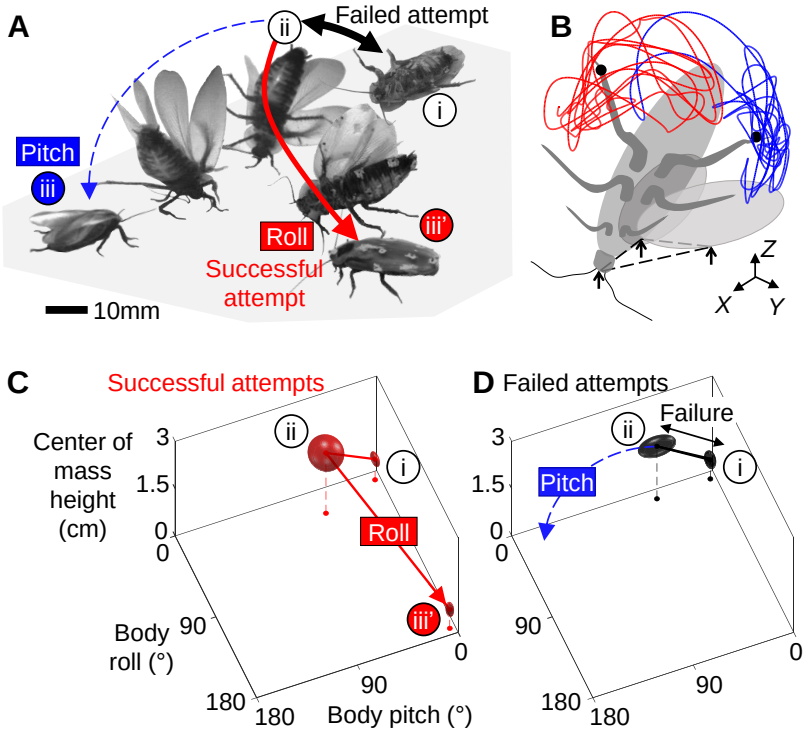

Figure 3.1: Strenuous, leg-assisted, winged ground self-righting of discoid cockroach. (A) Representative snapshots of animal successfully self-righting by pitch (blue) and roll (red) modes after multiple failed attempts (black arrow). See Figure 1—video 1 for a typical trial, in which the animal makes multiple failed attempts to pitch over the head and eventually rolls to self-right. (B) Schematic of metastable state with a triangular base of support (dashed triangle) formed by ground contacts of head and two wing wedges, with vigorous leg flailing. Red and blue curves show representative trajectories of left and right hind leg tips from a trial. x-y-z is lab frame. (C, D) Stereotyped body motion during successful (C) and failed (D) self-righting attempts in body pitch, body roll, and center of mass height space. i, ii, and iii in A, C, and D show upside-down (i), metastable (ii), and upright (iii, iii') states. Ellipsoids show means (center of ellipsoid) $\pm$ s.d. (principal semi-axis lengths of ellipsoid) of body pitch, body roll, and center of mass height at the beginning, highest center of mass height, and end of the attempt. For failed attempts, the upside-down state at the end of the attempt is not shown because it overlaps with the upside-down state at the start of the attempts (i). Data from Li et al., 2019. Reproduced from Othayoth and Li, 2021

support, in which the center of mass projection falls (Figure 3.1Aii, B), this intermediate state is metastable. However, wing pushing rarely pitches the animal all the way over its head to self-right (the pitch mode, Figure 3.1Aii-iii, blue). Thus, the animal often opens and closes its wings (hereafter referred to as an attempt) multiple times, resulting in its body repeatedly pitching up and down, but it fails to self-right (Figure 3.1A, black arrows). Eventually, the animal almost always self-rights by rolling sideways over one of the wings (the roll mode; Figure 3.1Aii-iii', red). Although wings are the primary propulsive appendages in this self-righting strategy, the animal also vigorously flails its legs mediolaterally, even when body pitching nearly prevents them from reaching the ground (Figure 3.1B, dashed curves). The legs occasionally scrape the ground, the abdomen occasionally flexes and twists, and the wings often deform passively under load (Li et al., 2019). For simplicity, we focused on the perturbing effects of the more frequent leg flailing (but see discussion of these other perturbing motions). Another curious observation is that, although the animal can in principle rotate its body in arbitrary trajectories to self-right, the observed body motion is stereotyped (Figure 3.1) (Li et al., 2019).

A recent potential energy landscape approach to locomotor transitions (Othayoth, Thoms, and Li, 2020; Othayoth et al., 2021b) provides a modeling framework to understand how propelling and perturbing appendages together contribute to strenuous ground self-righting. A previous study modeling ground self-righting of turtles in two dimensions (the transverse plane in which the body rolls) suggested that, when trapped in a gravitational potential energy well, modest kinetic energy from perturbing appendages (legs and neck) helps overcome the small potential energy barriers (Domokos and Várkonyi, 2008). A

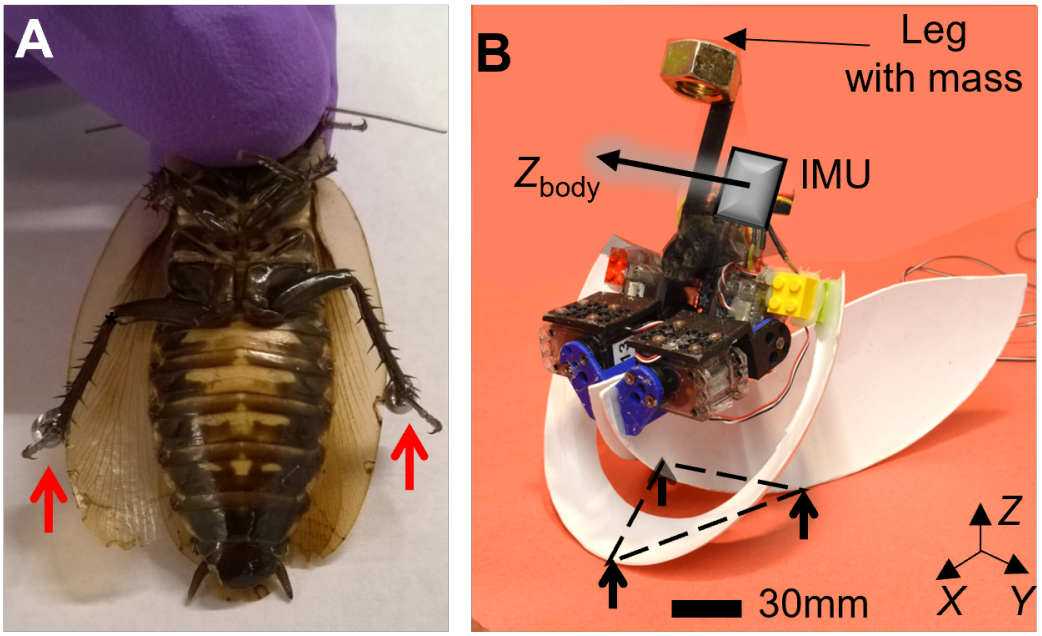

Figure 3.2: Animal leg modification and robotic physical model. (A) Discoid cockroach with modified hind legs with stainless steel spheres attached. (B) Robotic physical model in metastable state with a triangular base of support (dashed triangle), formed by ground contacts of head and two wing edges. Black arrow shows body Z-axis, Z_{body}. Reproduced from Othayoth and Li, 2021.

recent study of cockroaches took an initial step in expanding potential energy landscape modeling of ground self-righting to three dimensions (Li et al., 2019). However, due to frequent camera occlusions, this study was unable to measure the complex 3-D motions of appendages and only modeled the animal as a rigid body. For turtles with a rigid shell interacting with the ground, modeling self-righting with a rigid body is a good first-order approximation. However, this approximation is no longer good for modeling winged self-righting of the discoid cockroach because wing opening will change potential energy landscape.

Inspired by these insights and limitations, we hypothesized that the discoid cockroach's wing opening reduces the barriers to be sufficiently low for small

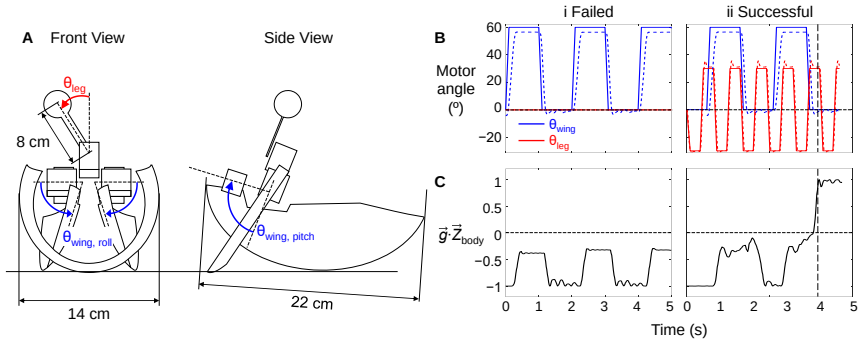

Figure 3.3: Robot wing and leg actuation and body orientation measurement. (A) Schematic of leg-assisted, winged self-righting robot from front and side views with geometric dimensions. Front view illustrates wing rolling and leg oscillation and side view illustrates wing pitching. Wing pitching and rolling are by the same angle, synchronized, and together compose wing opening. (B) Motor angles of wings (blue) and leg (red) as a function of time. Solid and dashed curves are commanded and measured motor actuation profiles, respectively. (C) Projection of gravitational acceleration vector "g"onto body Z-axis "Z" body as a function of time, measured using onboard IMU. Vertical dashed line shows the instant when the robot self-righted. In B, C, columns i and ii are for a representative failed and successful trial, respectively. Reproduced from Othayoth and Li, 2021.

kinetic energy from leg flailing to overcome. This hypothesis predicted that the greater the wing opening and leg flailing are, the more likely self-righting is to occur. We first tested this prediction in the animal, by directly modifying the hind leg inertia to increase kinetic energy from leg flailing (Figure 3.2A) and studying how it impacted self-righting probability. Then, we developed a robotic physical model (Figure 3.2B) to systematically test the prediction using repeatable experiments over a wide range of wing opening and leg oscillation amplitudes. In addition, we modeled the escape from the metastable state to self-right as a probabilistic barrier-crossing transition on an evolving potential energy landscape of the self-deforming robot/animal, facilitated by kinetic energy. The landscape is the gravitational potential energy of the robot in its body

pitch-roll space. Because self-righting could in principle occur via both roll and pitch modes, we analyzed the potential energy barriers on landscape and the kinetic energy from wing opening (primary propulsion) and leg flailing (secondary perturbation) along roll and pitch directions. Considering the effects of wing opening and leg flailing separately gave new insight into the physical mechanism of self-righting. Finally, we examined whether the observed stereotypy of the animal's body motion can be explained by the potential energy landscape.

We designed and controlled our robotic physical model to achieve similar, strenuous self-righting behavior as the animal's, where both wing and leg use are crucial (see discussion). The robot consisted of a head, two wings, a leg, and motors to actuate the wings and leg (Figure 2B). To emulate the animal's wing opening, both robot wings opened by rolling and pitching about the body by the same angle (defined as wing opening amplitude, θ_{wing}; Figures 3.2B, 3.3). To simplify leg flailing of the animal, the robot used an actuated inverted pendulum (leg) which oscillated in the coronal plane by the same angle to both sides (defined as leg oscillation amplitude, θ_{leg}; Figures 3.2B, 3.3). We opened and closed the robot's wings (hereafter referred to as an attempt) repeatedly while oscillating its legs to generate repeated attempts observed in the animal. The robot's leg oscillation was feedforward-controlled, considering that the animal's leg flailing motion did not correlate with wing opening motion (see Materials & Methods for detail). Sufficiently large or sufficiently asymmetric wing opening alone guarantees self-righting (Li et al., 2016; Li et al., 2017)). Here, to study the effect of using both wings and legs under the most strenuous condition, we chose to open both wings symmetrically and only used sufficiently small θ_{wing} with which the robot did not always self-right with wing opening alone. We

emphasize that our goal was not to simply achieve successful self-righting in a robot, but use the robot as a test platform to systematically vary wing opening and leg flailing in a controlled manner.

We chose to focus potential energy landscape modeling on the robotic physical model because it offers two advantages. First, the animal's complex 3-D motion with many degrees of freedom is difficult to quantify. It would take ∼540 hours (∼12 working weeks) to track our animal dataset (∼5 seconds per trial at 200 frames/s, with 3 markers on the body, each wing, and each leg) to quantify 3-D motion required for calculating the potential energy landscape. In addition, wing motion is often impossible to quantify due to occlusion under the body. By contrast, the robot's simpler mechanical design, controlled actuation, and an onboard inertial measurement unit (IMU) sensor allowed easier reconstruction of its 3-D motion. Second, the animal's wing opening and leg flailing are highly variable (Xuan and Li, 2020a) and cannot be controlled. This results in the potential energy landscape varying substantially from trial to trial and makes it difficult to evaluate how the system behaved probabilistically on the landscape. By contrast, the robot's controlled variation of wing opening and leg flailing allowed us to do so. Considering that body rolling is induced by centrifugal force from leg flailing, we compared the ratio of leg centrifugal force to leg gravitational force between the animal and robot and verified they are dynamically similar (see Materials and Methods for detail). In addition, because the animal and robot are geometrically similar, their potential energy barriers also scale as expected (Table 2). Thus, we argue that the physical principles discovered for the robot are applicable to the animal.

3.4 Methods–Animal Experiments

3.4.1 Animals

We used 30 adult male *Blaberus discoidalis* cockroaches (Figure 3.2A) (Pinellas County Reptiles, St Petersburg, FL, USA), as females were often gravid and under different load-bearing conditions. Prior to experiments, we kept the animals in individual plastic containers at room temperature (24 ^{o}C) on a 12h:12h light: dark cycle and provided water and food (rabbit pellets) ad libitum. Animals weighed 2.6 $\pm$ 0.2 g and measured 5.3 $\pm$ 0.2 cm in length, 2.3 $\pm$ 0.1 cm in width, and 0.8 $\pm$ 0.1 cm in thickness. All data are reported as mean $\pm$ s.d. unless otherwise specified.

3.4.2 Leg modification

To study the effect of leg flailing, we directly modified both hind legs of the animal. We attached stainless steel spheres of diameter 0.32 cm and mass 0.14 g (5% of body weight, 180% of leg weight (McMaster-Carr, Elmhurst, IL, USA) to the tibia-tarsus joint of both hind legs (Figure 3.2A) using ultraviolet curing glue (BONDIC, Ontario, Canada). We verified that the added mass increased the average kinetic energy during leg flailing (Figure 3.6, see Section 3.4.6 'Kinetic energy measurement').

3.4.3 Experiment protocol

We used a flat, wooden surface (60 cm $\times$ 60 cm) covered with cardstock and walled with transparent acrylic sheets as the righting arena. Four 500 W work

lights (Coleman Cable, Waukegan, IL, USA) illuminated the arena for high-speed imaging. We maintained the arena at an ambient temperature of 40 ± 2C during experiment. We used two synchronized cameras (Fastec IL5, Fastec Imaging, San Diego, CA, USA) at 200 frames s^{-1} and 200 µs shutter time to record the self-righting maneuver from top (1200 × 1080 pixels) and side (1200 × 400 pixels) views, with a small lens aperture to maximize the focal depth of field.

For each trial, we first started video recording, held the animal upside-down by its pronotum, and gently released it from a height of ≈ 1 cm above the center of the righting arena. The small drop was to ensure that the animal did not begin leg searching, a common strategy used to self-right (Camhi, 1977), before it was released. The animal was given 10 seconds to attempt to self-right during each trial. After it self-righted or 10 seconds elapsed, the animal was picked up, and video recording was stopped. After each trial, we returned the animal to its container and continued testing a different animal. This way, each animal was allowed to rest for ≈ 30 minutes before its next trial to minimize the effects of fatigue (Camhi, 1977).

We tested 30 animals, each with five trials with its hind legs intact and then modified, resulting in a total of 300 accepted trials ($N = 30$ animals, $n = 150$ trials for each leg treatment). We excluded trials in which the animal collided with the walls of the righting arena or moved out of both camera views.

3.4.4 Self-righting performance

For each animal trial, we watched the videos to determine whether the animal self-righted. Because the animal did not always immediately begin to self-right

when placed on the arena (Camhi, 1977; Li et al., 2019), we defined the beginning of the self-righting attempt as the instant when the animal began moving its body or appendages to self-right. We defined the animal to have successfully self-righted if it attained an upright orientation with all six legs on the ground within 10 s of starting its attempt. We identified the trials in which animal succeeded in self-righting using the leg-assisted, winged strategy. For each animal and each leg treatment, we defined and measured self-righting probability as the number of trials that self-righted using winged attempts divided by the total number of trials. We counted the trials that used the legged strategy as failed. We then calculated average self-righting probability for each leg treatment by averaging across all animals.

3.4.5 Preference of self-righting strategies

We verified that the animal's preference of winged and legged self-righting strategies (see Footnote 1) did not change with leg modification. To compare the animal's preference of winged and legged self-righting strategies before and after leg modification, for each trial, we examined the videos to identify winged and legged self-righting attempts and measured the percentage of time spent on each strategy. Then, for each leg treatment and each animal, we averaged it across all the trials from that animal. For each treatment, we then averaged across each animal to calculate the average percentage of time spent on each strategy (Figure 3.5).

3.4.6 Kinetic energy measurement

To measure the animal's pitch and roll kinetic energy during self-righting, in a separate experiment, we used three high speed cameras (Photron FASTCAM Mini UX-100) to record the animal self-righting at 2000 frames s^{-1} and a resolution of 1280 $\times$ 1024 pixels, first with its hind legs intact (N = 2 animals, n = 2 trials) and then modified (N = 2 animals, n = 2 trials).

We used DeepLabCut (Mathis et al., 2018) to track the tip and femur-tibia joint of both hind legs, head anterior tip, abdomen posterior tip, and body midpoint (Figure 3.6A, B). We then used Direct Linear Transformation software DLTdv5 (Hedrick, 2008b) to reconstruct 3-D motion of the tracked points and used a sixth order Butterworth filter with a cut-off frequency of 25 Hz to filter their 3D positions.

To calculate kinetic energy, we approximated the animal body as an ellipsoid cut into two parts at 38% of total length from the anterior end, connected by a hinge joint (thorax-abdomen joint, Figure 3.6A). The smaller part represented the animal's head and thorax, and the larger part represented its abdomen. We assumed uniform mass distribution for both parts. We used the geometric center of the body parts when their fore-aft axes are aligned to approximate body center of mass . For both hind legs, we approximated the coxa-femur and tibia-tarsus segment as rigid rods. One end of the rod representing coxa-femur segment was connected to the body at the midpoint of thorax-abdomen joint, and the other end connected to the rod representing tibia-tarsus segment, both via spherical joints (Figure 3.6A, B, thick black lines connected by blue dots). For modified hind legs, we approximated the stainless steel spheres at the leg

tip as a point mass attached to the free end of the tibia-tarsus rod (Figure 3.6A, B).

We defined pitch and roll kinetic energy as the sum of kinetic energy from translational and rotational velocity components from all body parts that contribute to pitching and rolling motion, respectively. We obtained pitch and roll kinetic energy by summing contributions from the body ellipsoid parts and the hind leg segments. For each part, we measured its rotational velocity components about the animal's body fore-aft (X_{body}) and lateral (Y_{body}) principal axes, and we measured the translational velocity components of its center of mass along the fore-aft and lateral directions (Figure 3.6B, red vs. blue arrows). For the sphere attached to modified leg, we measured its translational velocities. Because vertical translational velocity and yaw angular velocity did not contribute to motion along the pitch or roll direction, we did not consider them. For each of the ellipsoid parts and rigid rods, we calculated its pitch and roll kinetic energy as follows:

$$KE_{pitch,j} = \frac{1}{2} I_{yy,j} \omega_{y,j}^2 + \frac{1}{2} m_j v_{x,j}^2 \tag{3.1}$$

$$KE_{roll,j} = \frac{1}{2} I_{xx,j} \omega_{x,j}^2 + \frac{1}{2} m_j v_{y,j}^2 \tag{3.2}$$

where $I_{xx,j}$ and $I_{yy,j}$ are the moments of inertia the j^{th} object measured about the animal's body fore-aft (X_{body}) and lateral (Y_{body}) principal axes, respectively, m_j is the mass of j^{th} object, $\omega_{x,j}$ and $\omega_{y,j}$ are the rotational velocities of the j^{th} object about body fore-aft and lateral principal axes, and $v_{x,j}$ and vy, j are the translational velocity of the center of mass of the j^{th} object along fore-aft and

lateral directions, respectively (Figure 3.6B). For both hind leg segments, we used the mass reported in (Kram, Wong, and Full, 1997) (0.07 g for coxa-femur segments and 0.01 g for tibia-tarsus segment). To calculate the mass of the two body parts, we assumed body density to be uniform.

We calculated the pitch and roll kinetic energy of the added spherical mass as follows:

$$KE_{pitch,sphere} = \frac{1}{2} m_{sphere} v_{x,sphere}^2 \tag{3.3}$$

$$KE_{roll,sphere} = \frac{1}{2} m_{sphere} v_{y,sphere}^2 \tag{3.4}$$

where m_{sphere} is the added spherical mass, and v_x, sphere and v_y, sphere are the translational velocity components of the sphere along fore-aft and lateral directions, respectively. We considered kinetic energy from the added spherical mass only for animal with modified legs.

We obtained the pitch and roll kinetic energy of the intact animal from equations (3.1) and (3.2) respectively. For the modified animal, we added equations (3.1) and (3.3) to obtain total pitch kinetic energy and added (3.2) and (3.4) to obtain total roll kinetic energy. For each trial, we first averaged the measured kinetic energy along pitch and roll directions over the recorded interval (2.5 s) for each trial. Then for each leg treatment, we further averaged it across all the trials of that treatment (intact: $N = 2$ animals, $n = 2$ trials; modified: $N = 2$ animals, $n = 2$ trials).

3.4.7 Relationship between wing opening and leg flailing

We examined whether the animal's leg flailing during self-righting was more feedforward-driven or more towards a feedback-controlled reflex coordinated with wing opening. To do so, we measured the correlation between wing opening and leg flailing motions as well as their self-correlations (Figure 3.7). Because wing opening was difficult to measure due to occlusion of wings by the body during self-righting, we used abdomen tip height as a proxy for wing opening, considering that abdomen tip height typically increased as wings opened. For each hind leg, we used its leg tip height as a proxy of the flailing motion (Figure 3.6). To check whether the height of abdomen tip and hind leg tips were correlated to each other and to themselves, we measured the normalized cross-correlations between each pair of these variables and the normalized autocorrelation of each of them (Figure 3.7). Normalized cross correlation h between two signals f (t) and g(t) is defined as

$$h(t) = \frac{\int_{-\infty}^{\infty} f^*(\tau - t)g(\tau)d\tau}{\sqrt{\int_{-\infty}^{\infty} |f(\tau)|^2 d\tau . \int_{-\infty}^{\infty} |g(\tau)|^2 d\tau}} \tag{3.5}$$

where t is the time lag between $f(t)$ and $g(t)$ and is a variable, τ is the variable of integration, and $f*(t)$ is the complex conjugate of $f(t)$. When $f(t) = g(t)$, $h(t)$ is the normalized autocorrelation.

All normalized cross correlations plots lacked a prominent peak whose value was close to 1, and all normalized autocorrelations plots had a prominent peak only at zero lag. This showed that abdomen tip height did not correlate with itself or with either of the two hind leg tips heights (Figure 3.7A, B, F). This

meant that wing opening and leg flailing motions were not correlated to each other during self-righting. However, the normalized cross correlation between both hind legs had recurring oscillations as the lag increased in magnitude (Figure 3.7). This suggested that leg flailing had some rhythm, despite a large temporal variation and difference between the two hind legs (Delcomyn, 1987; Sherman, Novotny, and Camhi, 1977; Zill, 1986).

3.5 Methods–Robotic physical modelling

3.5.1 Design and actuation

The robot consisted of a head, two wings, a leg, and four motors to actuate the wings and one to actuate the leg (Table 1, Figures 3.2B, Figure 3.3). The head and wings were cut from two halves of a thin ellipsoidal shell thermoformed (Formech 508FS, Middleton, WI, USA) from 0.16 cm thick polystyrene plastic sheet (McMaster-Carr, Elmhurst, IL, USA). We connected different parts using joints 3-D printed using PLA (Ultimaker 2+, Geldermalsen, Netherlands) (Figure 3.2B). We used DC servo motors (Dynamixel XL-320, ROBOTIS, Lake Forest, CA, USA) to actuate both the wings and the leg.

To measure the robot's 3-D orientation (roll, pitch, and yaw angles), we attached an inertial measurement unit (IMU) (BNO055, Adafruit, New York, NY, USA) near its center of mass determined from the robot CAD model. We used the Robot Operating System (Version: melodic) ((Quigley et al., 2009)) to send actuation signals for the wing and leg motors and record IMU data. To ensure a constant voltage for repeatable experiments, we used an external 8 V voltage source (TP3005DM, TEK Power, Montclair, CA, USA) to power the robot. We used fine flexible wires (30 AWG, 330-DFV, Vishay Sensor, USA) for powering robot and sending/acquiring signals and ensured that they were loose and did not interfere with robot motion.

3.5.2 Similarity to animal

To examine whether the robotic physical model was similar to the animal and reasonably approximated its self-righting motion, we examined how well they

Table 3.1: Mass distribution of the robot.

Component	**Mass (g)**
Head	13.4
Leg rod	4.3
Leg added mass	51.5
Leg motor	28.6
Two wings	57.4
Two wing pitch motors	56.0
Two wing roll motors	48.8
Total	260.0

were geometrically similar and their leg flailing motions were dynamically similar. To evaluate geometric similarity, we compared their dimensions. For geometrically similar objects, length l should scale with mass m and density ρ as $l \propto (m/\rho)^{1/3}$ (Alexander, 2006). Following this, potential energy should scale as $E \propto m \cdot (m/\rho)^{1/3} \propto m^{4/3}\rho^{-1/3}$.The robot, which was 90 times as much heavy and 2.3 times as much dense as the animal with modified legs (Table 3.2) was expected have dimensions $(90/2.63)^{1/3} = 3.4$ times those of the animal. For the animal, m includes the added mass from leg modification because we used the same for calculating the potential energy landscape. Because gravitational potential energy is proportional to mass and center of mass height, the potential energy barriers should scale by a factor of $90^{4/3} \times 2.63^{-1/3} = 305$ (Table 2). We found that the robot's length, thickness, and pitch potential energy barriers scaled up roughly as expected (Table 2). The larger scaling factor for robot's width and roll potential energy barrier is due to the robot being designed wider to make self-righting via rolling more strenuous.

To evaluate dynamic similarity between the robot and animal, we calculated Froude Number for their leg flailing. Here, we used the following definition of

Table 3.2: Comparison between animal and robot.

Parameter		**Animal**	**Robot**	**Ratio**
Body length 2a (mm)		53	260	4.9
Body width 2b (mm)		23	220	9.6
Body thickness 2c (mm)		8	43	5.4
Mass attached to leg (g)		0.14	51.5	368
Total mass m* (g)		2.84	260	90
Density ρ ($\times 10^{-3} g \cdot mm^{-3}$)		0.88	2.05	2.3
Expected length scale factor $(m/\rho)^{1/3}$		1.47	5.06	3.4
Expected potential energy scale factor $m^{4/3}/\rho^{1/3}$		4.28	1306	305
Maximum pitch potential energy barrier (mJ)		0.58	282	486
Maximum roll potential energy barrier (mJ)		0.19	244	1284
Froude number for leg flailing Fr	Intact legs	0.37	0.78	2.1
	Modified legs	1.27		0.61

* Includes mass attached to the legs.

Froude number (Biewener, 2003):

$$Fr = \frac{\text{Inertial force from leg flailing}}{\text{Gravitational force of leg}} = \frac{mv^2/r}{mg} = \frac{v^2}{rg} \tag{3.6}$$

where m is the mass of the animal or robot leg(s), plus the added mass attached it for the modified animal, v is the leg translational velocity along the body lateral principal axis, g is gravitational acceleration, and r is leg length.

We found that the Froude numbers for the robot and both the intact and modified animals were similar (within a factor of two). This dynamic similarity demonstrated that the robot provided a good physical model for studying the animal's self-righting.

3.5.3 Experiment protocol

For robot experiments, we used a level, flat, rigid wooden surface (60 cm $\times$ 60 cm) covered with sandpaper as the righting arena. We used two synchronized

webcams (Logitech C920, Logitech, Newark, CA, USA) to record the experiment from top and side views at 30 frames s-1 and a resolution of 960 × 720 pixels. Using the onboard IMU, we recorded the robot body orientation relative to the lab coordinate system (X-Y-Z in Figure 3.2B) at ≈ 56 Hz and synchronized them with the motor actuation timings angles (Figure 3.3, bottom right).

Before each trial, we placed the robot upside-down (Figure 3.9Ai) on the arena, with its wings closed and leg aligned with the body midline and started video recording. We then actuated the robot to repeatedly open and close its wings at 2 Hz and oscillate its legs at 2.5 Hz to self-right. Because the animal was likely to move its leg before wings at the start of self-righting (59% of intact leg trials and 81% of modified leg trials), for non-zero robot leg oscillation amplitudes, the first wing opening was started after completing one cycle of leg oscillation (0.4 s). If the robot did not self-right after five wing opening attempts (10 s), we powered down the robot, stopped video recording, and reset the robot for the next trial. We tested self-righting performance of the robot by systematically varying leg oscillation amplitude θ_{leg} (0°, 15°, 30°, 45°) and wing opening amplitude θ_{wing} (60°, 72, 83°). We collected five trials for each combination of θ_{wing} and θ_{leg}. This resulted in a resulted in a total of 60 trials with 134 attempts.

To reconstruct the robot's 3-D motion, in a separate experiment, we characterized how the wing and leg actuation angles changed over time during an attempt (Figure 3.3). We attached BEETag markers (Crall et al., 2015) to the body frame and to each link actuated by the motors and tracked their positions using two calibrated high speed cameras (Fastec IL5, Fastec Imaging, San Diego, CA, USA) at 500 frame $s{-}1$ and a resolution of 1080 × 1080 pixels,

as the robot actuated its wings and legs to self-right. We obtained 3-D kinematics of the markers using the Direct Linear Transformation method DLTdv5 (Hedrick, 2008b). We then measured the rotation of the link actuated by each motor about its rotation axis as a function of time during an attempt. Because the wings were controlled to roll and pitch by the same angle, we used the average measured wing actuation profile of all the four motors (two for wing pitching and two for wing rolling). The actual wing opening and leg oscillation angles were smaller than the commanded (solid blue and red) due to the inertia of robot body components attached to each motor.

3.5.4 Self-righting performance

We defined the beginning of the righting attempt as the instant when the robot first started opening its wings and measured this instance from the commanded motor actuation profile (Figure 3.3Bii). We defined the robot to have successfully self-righted if it attained an upright orientation within 10 seconds (five attempts). We used the IMU to measure the projection of the gravity acceleration vector $\mathbf{g}$ onto the body Z-axis $\mathbf{Z}_{body}$ as a function of time. This allowed us to determine when the robot became upright. We then counted the number of successful and failed attempts for each trial. For each trial, we defined self-righting probability as the ratio of the number of successful attempts to the total number of attempts of that trial. At each wing opening and leg oscillation amplitude, we then averaged it across all trials of that treatment to obtain its average self-righting probability. Among all the 134 attempts observed across all 60 trials, 44 attempts succeeded (12, 15, and 17 attempts at $\theta_{wing} = 60°$, 72°, and 83°, respectively), and 90 attempts failed (46, 27, and 17 attempts at

θ_{wing} = 60°, 72°, and 83°, respectively).

3.5.5 Robot 3-D motion reconstruction

For each robot trial, we measured the robot's 3-D orientation in the lab frame using Euler angles (yaw α, pitch β, and roll γ, Z-Y'-X" Tait-Bryan convention). We divided each trial temporally into 0.01 s intervals and used the measured motor actuation angles and body 3-D orientation (Figure 3.3 B, C) at each interval to reconstruct the robot's body shape and 3-D orientation, respectively. Because the IMU measured only the 3-D orientation of the robot, we constrained the robot's center of mass to translate only along the vertical direction (Figure 3.2B, Z-axis of lab frame) while maintaining contact with the ground. We then used the reconstructed 3-D motion of the robot to obtain the translational and rotational velocity components of all robot parts.

3.5.6 Kinetic energy measurements

For each robot trial, we measured pitch and roll kinetic energy for all attempts. We defined pitch and roll kinetic energy as the kinetic energy of the entire robot due to translational and rotational velocities along body fore-aft and lateral directions, respectively. Because vertical translation and yawing do not contribute to body pitching or rolling towards self-righting, we did not consider vertical velocities or rotational velocities about the vertical axis. Considering that the five motors, leg, and mass added to the leg could be approximated as regular, symmetric shapes with uniform mass distribution (motors and leg as solid cuboids and added mass as a solid sphere), the moment of inertia at the center of mass of each part could be directly calculated. Then, we calculated

the total pitch and roll kinetic energy of the motors and leg with added mass as:

$$KE_{pitch} = \sum_{j=1}^{k}(\frac{1}{2}I_{yy,j}\omega_{y,j}^2 + \frac{1}{2}m_j v_{x,j}^2) \tag{3.7}$$

$$KE_{roll} = \sum_{j=1}^{k}(\frac{1}{2}I_{xx,j}\omega_{x,j}^2 + \frac{1}{2}m_j v_{y,j}^2) \tag{3.8}$$

where j enumerates the five motors, leg, and mass added to the leg, $I_{xx,j}$ and $I_{yy,j}$ are the moments of inertia of object j about the body fore-aft and lateral principal axes (measured at the part's center of mass), m_j is the mass of object j, and $v_{x,j}$ and $v_{y,j}$ are translational velocities of object j along fore-aft and lateral directions of robot, and ω_x and ω_y are rotational velocities of object j about fore-aft and lateral directions of the robot, respectively. For both the wings and head with complex shapes, we imported their CAD model and approximated them with uniformly distributed point mass clouds and calculated the pitch and roll kinetic energy of each part as:

$$KE_{pitch,cloud} = \frac{m}{2k}\sum_{j=1}^{k} v_{x,j}^2 \tag{3.9}$$

$$KE_{roll,cloud} = \frac{m}{2k}\sum_{j=1}^{k} v_{y,j}^2 \tag{3.10}$$

where m is the total mass of the wing or head, k is the number of point masses in the point cloud, and $v_{x,i}$ and $v_{y,i}$ are the velocity components of the i_{th} point mass along the body fore-aft and lateral principal axes.

To obtain total pitch and roll kinetic energy, we summed the pitch and roll kinetic energy of all the parts. To compare pitch and roll kinetic energy at each combination of wing opening and leg oscillation amplitudes, we first averaged

the total pitch and roll kinetic energy respectively over the phase when wings were fully open in the first attempt of each trial to avoid bias from the large rolling kinetic energy during successful self-righting in later attempts. We then averaged these temporal averages across the five trials at each combination of wing opening and leg oscillation amplitudes (Figure 3.8A, B).

3.6 Methods–Potential energy landscape modelling

3.6.1 Model definition

The gravitational potential energy of the animal or robot is:

$$E = mgz_{CoM} \tag{3.11}$$

where m is the total mass of the animal or robot, g is gravitational acceleration, z_{CoM} is center of mass height from the ground. To determine the robot's center of mass, we used a CAD model of the robot (Figures 3.2A, Figure 3.3) and measured the 3-D positions and orientations of all robot body parts for a given body orientation and wing opening (see consideration of leg oscillation below). We approximated the animal body as a rigid ellipsoid, with the animal's center of mass at the body geometric center, and its wings as slices of an ellipsoidal shell. Because the animal or robot did not lift off during self-righting, in the model we constrained the lowest point of the animal or robot to be always in contact with the ground.

The potential energy depended on body pitch and roll, wing opening angle, and leg oscillation angle. Because the effect of leg oscillation was modelled as a part of kinetic energy, for simplicity, we set the leg to be held fixed in the middle when calculating the potential energy landscape. We verified that potential energy landscape did not change considerably (roll barrier changed only up to 13%) when the leg moved. Because we used Euler angles for 3-D rotations, change in body yaw did not affect center of mass height. Because the robot's initial wing opening was negative (-6°) due to body weight, in our model

calculations, we varied wing opening angle within the range [-10°, 90°] with a 0.5° increment. For each wing opening angle, we then varied both body pitch and roll within the range [-180°, 180°] with a 1° increment and calculated z_{CoM} to obtain the system potential energy (Figure 3.3). Because the animal or robot did not pitch backward significantly, in the figures we do not show landscape for body pitch < -90°; the full landscape maybe visualized using data and code provided (Othayoth and Li, 2021a).

3.6.2 System state trajectories on potential energy landscape

To visualize how the robot's measured system state behaved on the landscape, we first discretized each righting attempt into time intervals of 0.01 s. For each interval, we used the measured the wing opening angle (Figure 3.3, dashed blue curves) to calculate the potential energy landscape. We then projected the measured body pitch and roll onto the landscape to obtain the system state trajectory over time. Note that only the end point of the trajectory, which represented the current state, showed the actual potential energy of the system at the corresponding wing opening angle. The rest of the visualized trajectory showed how body pitch and roll evolved but, for visualization purpose, was simply projected on the landscape surface. The exact system state trajectories are shown in Figure 3.11.

3.6.3 Potential energy barrier measurements

We measured the potential energy barrier that must be overcome to escape from metastable basin to transition to an upright basin (Figure 3.9C, 3.13).

For each wing opening angle (Figure 3.13B, dashed blue), at each time interval, we considered imaginary straight paths away from the metastable local minimum (Figure 3.9B, white dot) in the body pitch-roll space, parameterized by the polar angle ψ from the positive pitch direction (body pitching up, Figure 3.9Ci). Along each path, we obtained a cross section of the landscape. Then, we defined and measured the potential energy barrier along this path as the maximal increase in potential energy in this cross section. Finally, we plotted the potential energy barrier as a function of ψ (Figure 3.9C). We defined the roll barrier as the lowest potential energy barrier within $\psi = \pm$ [45°, 135°], because both roll upright minima always lay in this angular range. We defined the pitch barrier as the potential energy barrier at $\psi = 0°$ towards the pitch local minimum. Finally, we measured both pitch and roll barriers as a function of wing opening angle (Figure 3.13, Figure 3.14).

3.6.4 Comparison of kinetic energy and potential energy barriers

To understand how wing opening and leg oscillation together contribute to the robot's self-righting, we compared the measured kinetic energy and potential energy barriers along both pitch and roll directions throughout each attempt. For each attempt, we measured kinetic energy minus potential energy barrier over time along both pitch and roll directions (Figure 3.15, 3.16 A-C). We then examined whether there was a surplus or deficit of kinetic energy to overcome the potential energy barrier in both pitch and roll directions, comparing between successful and failed attempts (Figure 3.15D, 3.16D). To examine how maximal surplus varied with wing opening and leg oscillation amplitudes, for

each combination of the two, we recorded the maximal surplus when the wings are held fully open in each attempt and averaged it across all attempts (Figure 3.15E vs. 3.16E).

3.6.5 Data analysis and statistics

We tested whether the animal's percentage of time spent on winged and legged self-righting attempts and self-righting probability changed with leg modification using a mixed-effects ANOVA, with leg treatment as the fixed factor and individual as a random factor to account for individual variability. We tested whether the animal's pitch and roll kinetic energy depended on leg modification using ANOVA with leg treatment a fixed-factor. We tested whether the animal's self-righting probability depended on leg treatment using a mixed-effect ANOVA with leg treatment as a fixed factor and individual as a random factor.

We tested whether the robot's self-righting probability, number of attempts required to self-right, pitch and roll kinetic energy depended on leg oscillation amplitude at each wing opening amplitude using a chi-squared test for probability and an ANOVA for the rest, with wing opening magnitude as a fixed factor. We tested whether kinetic energy minus potential energy barrier along the pitch and roll directions depended on leg oscillation amplitude at each wing opening amplitude, using ANOVAs with leg oscillation amplitude as the fixed factor. We also tested whether they depended on wing opening amplitude at each leg oscillation amplitude, using ANOVAs with wing opening amplitude as the fixed factor. To test whether kinetic energy minus potential energy barrier differed between successful and failed attempts, we used an ANOVA with the attempt outcome (success or failure) as the fixed factor.

3.7 Results

3.7.1 Leg flailing facilitates animal winged self-righting

As leg modification increased the animal's average kinetic energy in both pitch and roll directions (by 2 and 10 times, respectively; Figures 3.4A, 3.6; $P < 0.05$, ANOVA), its probability of self-righting using wings increased (Figure 3.4B; $P < 0.0001$, mixed-effect ANOVA). These observations supported our hypothesis. Leg modification did not change the animal's relative preference of using winged and legged self-righting strategies (Figure 3.5). In addition, wing opening and leg flailing did not show temporal correlation. Furthermore, the approximate time period of leg flailing (100 ms) was comparable to combined sensory feedback (6-40 ms (Ritzmann et al., 2012) and neuromuscular (45 ms (Sponberg and Full, 2008)) delays. These, combined with the fact that previous studies observed minimal proprioceptive sensory input from legs during flailing (Camhi, 1977; Delcomyn, 1987; Zill, 1986), indicate that leg flailing was more feedforward-driven than a feedback-controlled reflex coordinated with wing opening (Figure 3.6). Moreover, large trial-to-trial variations in the number of attempts required to self-right showed that the animal's self-righting was stochastic (Figure 3.7).

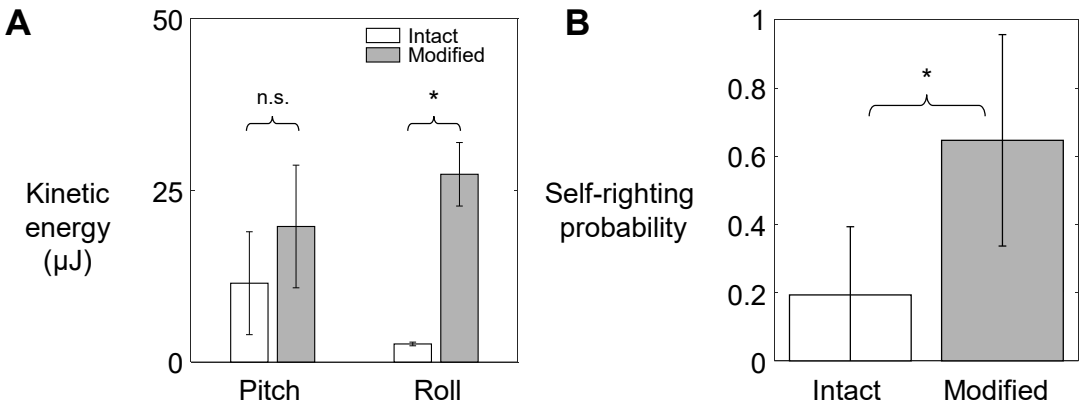

Figure 3.4: Animal's kinetic energy and self-righting probability. Comparison of (A) average pitch and roll kinetic energy and (B) self-righting probability between intact animals and animals with modified hind legs. Error bars in show ± s.d. Asterisk indicates a significant difference ($P < 0.05$) and n.s. indicates none. Statistical tests: Pitch kinetic energy: $P = 0.34$, $F_{1,1} = 1.53$, ANOVA. Roll kinetic energy: $P = 0.02$, $F_{1,1} = 50.35$, ANOVA. Probability: $P < 0.0001$, $F_{1,29} = 93.38$, mixed-effect ANOVA. Sample size: (A) $N = 2$ animals, $n = 2$ trials. (B) Intact: $N = 30$ animals, $n = 150$ trials. Modified: $N = 30$ animals, $n = 150$ trials. Reproduced from Othayoth and Li, 2021.

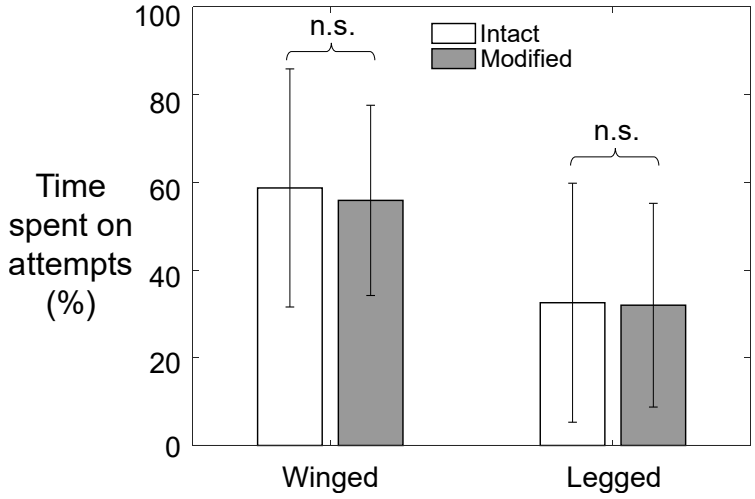

Figure 3.5: Comparison of average percentage of time spent on winged and legged self-righting attempts between animals with intact and modified legs. Error bars show ± s.d. n.s. indicates no significant difference. Winged: $P = 0.19$, $F_{1,269} = 1.71$; legged: $P = 0.78$, $F_{1,269} = 0.07$ mixed-effect ANOVA. Sample Size: $N = 30$ animals, $n = 150$ trials for each treatment. Reproduced from Othayoth and Li, 2021.

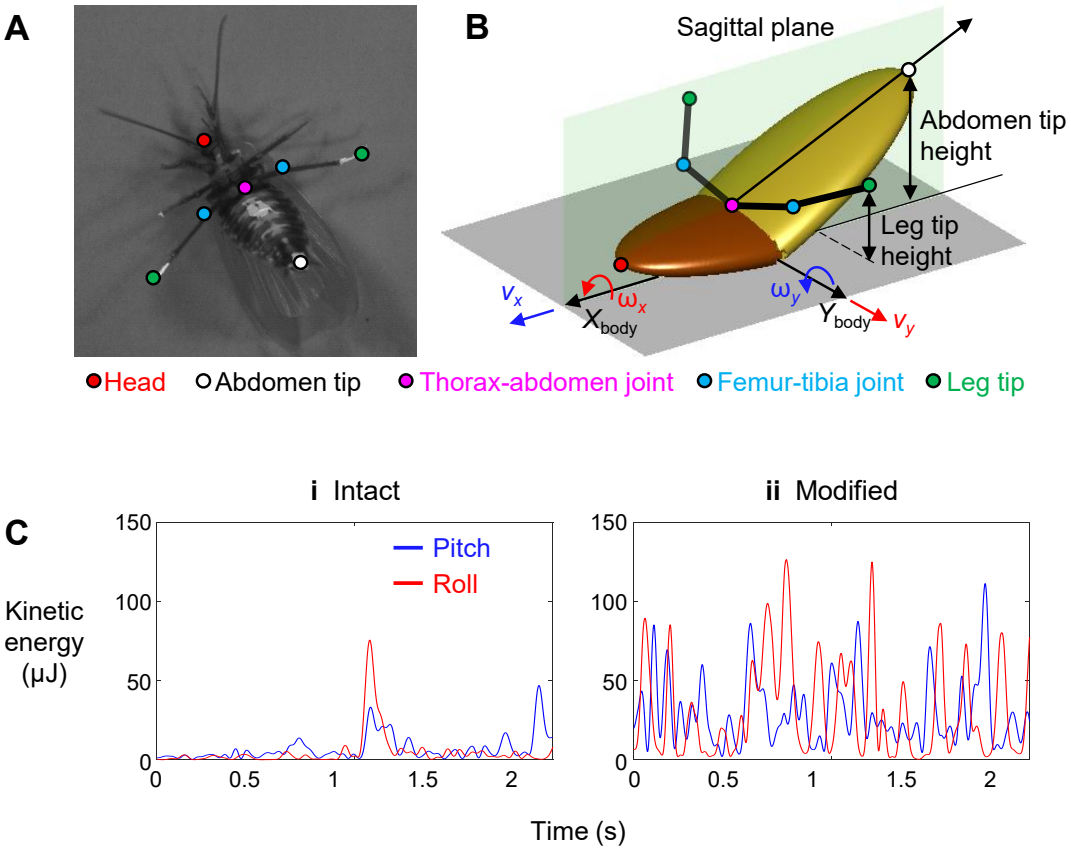

Figure 3.6: Animal kinetic energy calculation. (A) Representative snapshot of body and appendage with definition of markers tracked. (B) Multi-body model of animal for calculating pitch and roll kinetic energy. Red and blue arrows show velocity components that contribute to pitch and roll kinetic energy, respectively. (C) Pitch and roll kinetic energy as a function of time for animal with (i) intact and (ii) modified hind legs from a representative trial. Reproduced from Othayoth and Li, 2021.

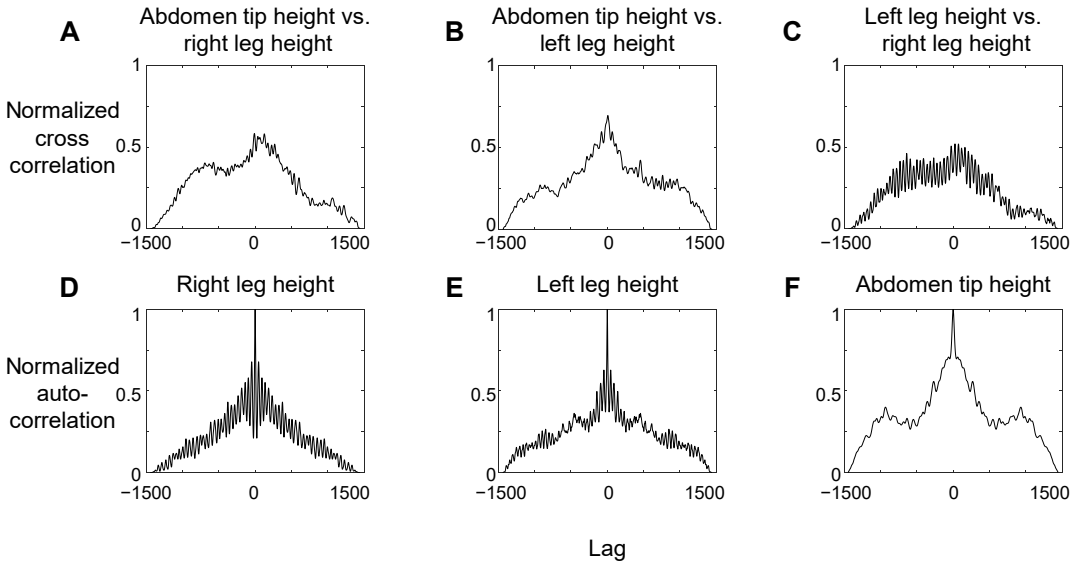

Figure 3.7: Correlation between animal's body and leg motion. (A-C) Pairwise normalized cross correlations between left hind leg tip height, right hind leg tip height, and abdomen tip height, as a function of lag between each pair of variables. (D-F) Normalized autocorrelation of left hind leg tip height, right hind leg tip height, and abdomen tip height as a function of lag between a variable and itself. $N = 1$ animal, $n = 1$ trial. Reproduced from Othayoth and Li, 2021.

3.7.2 Wing opening and leg flailing together facilitate robot self-righting

The robot's self-righting performance increased with both wing opening amplitude θ_{wing} and leg oscillation amplitude θ_{leg} (Figure 3.8). Similar to the animal, the robot's self-righting was stochastic, with large trial-to-trial variation in the number of attempts required to self-right and body pitching and rolling motions (Figures 3.11, 3.12). For each θ_{wing} tested, as θ_{leg} increased, average roll kinetic energy increased (Figure 3.8B; $P < 0.0001$, ANOVA) and the robot's self-righting probability increased (Figure 3.8C; $P < 0.0001$, Nominal logistic regression), reaching one at higher θ_{leg}. Meanwhile, the number of attempts required for self-righting decreased (Figure 3.8D; $P < 0.05$, ANOVA). At the maximal θ_{leg} tested (45°), the robot always self-righted (3.8C) and always did so in the first wing opening attempt (Figure 3.8D). Together, these results demonstrated that wing opening and leg flailing together facilitate the robot's self-righting performance over the wide range of parameter space tested.

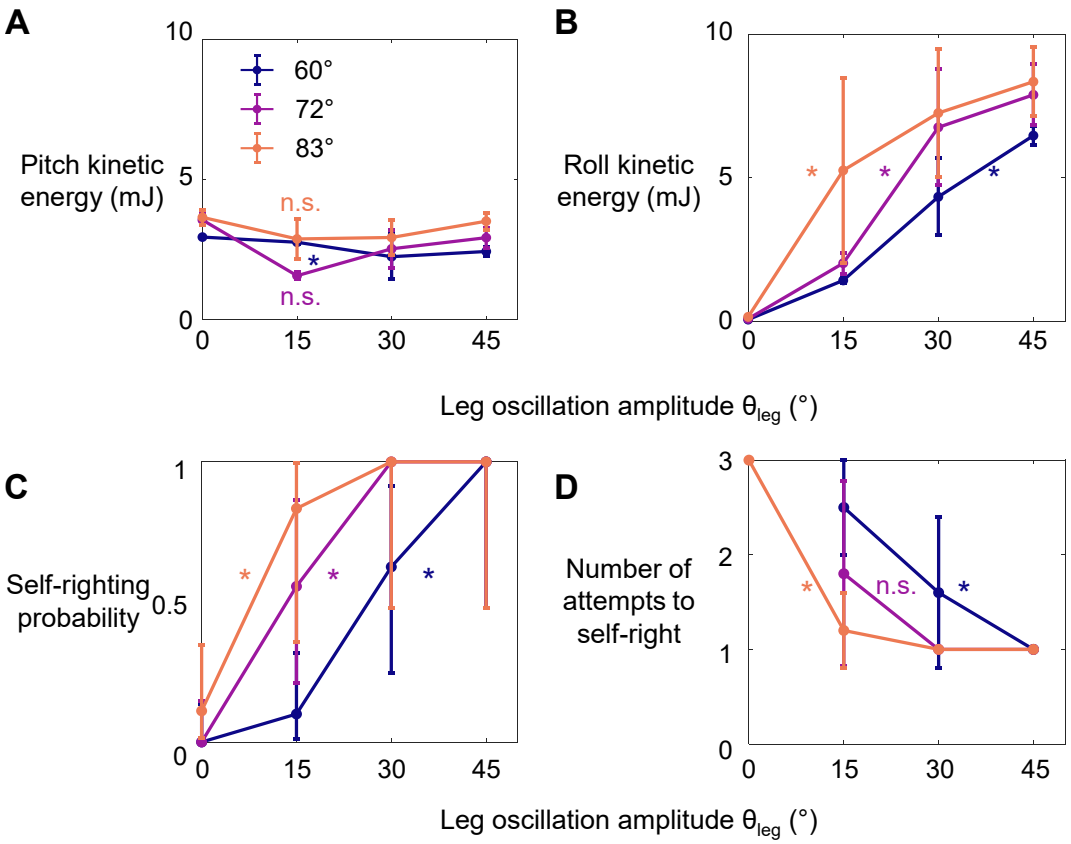

Figure 3.8: Robot's kinetic energy and self-righting performance. (A, B) Average pitch and roll kinetic energy during self-righting as a function of leg oscillation amplitude θ_{leg} at different wing opening amplitudes θ_{wing}. (C, D) Self-righting probability and average number of attempts required to self-right as a function of θleg at different θ_{wing}. Error bars in A, B, and D are ± s.d., and those in C are confidence intervals of 95%. Asterisks indicate a significant dependence ($P < 0.05$) on θ_{leg} at a given θ_{wing} and n.s. indicates none. See Figure 4 source data for detail of statistical tests. Sample size: Kinetic energy: $n = 20$ attempts at each wing opening amplitude. Self-righting probability and number of attempts: $n = 58$, 42, and 34 attempts at $\theta_{wing} = 60°$, 72°, and 83°. For kinetic energy, only the first attempt from each trial is used to measure the average to avoid bias from large pitching or rolling motion during subsequent attempts that self-right. Reproduced from Othayoth and Li, 2021.

Figure 3.9: Robot's self-righting motion and potential energy landscape. (A) Snapshots of reconstructed robot upside down (i), in metastable state (ii), self-righting by pitch (iii) and roll (iii') modes, and upright afterwards (iv, iv'). (B) Snapshots of potential energy landscape at different wing opening angles corresponding to (A) i, ii, iii. Dashed curves are boundary of upside-down/metastable basin. Green dots show saddles between metastable basin and the three upright basins. Gray curves show constant potential energy contours. Black, dashed blue, and red curves are representative trajectories of being attracted to and trapped in metastable basin, self-righting by pitch mode, and self-righting by roll mode, respectively. i, ii, iii in (A, B) show upside-down (1), metastable (2), and upright (3iii, iii') states. (C) Polar plot of potential energy barrier to escape from upside-down or metastable local minimum along all directions in pitch-roll space. Ψ is polar angle defining direction of escape in body pitch-roll space. Green arrow in (i) shows direction of upright minima at pitch = 180° ($\Psi = 0°$). Black circle shows scale of energy barrier (100 mJ). Blue and red arrows in (ii) define pitch and roll potential energy barriers. Blue and red error bars in (iii) show average maximal pitch and roll kinetic energy, respectively. Reproduced from Othayoth and Li, 2021.

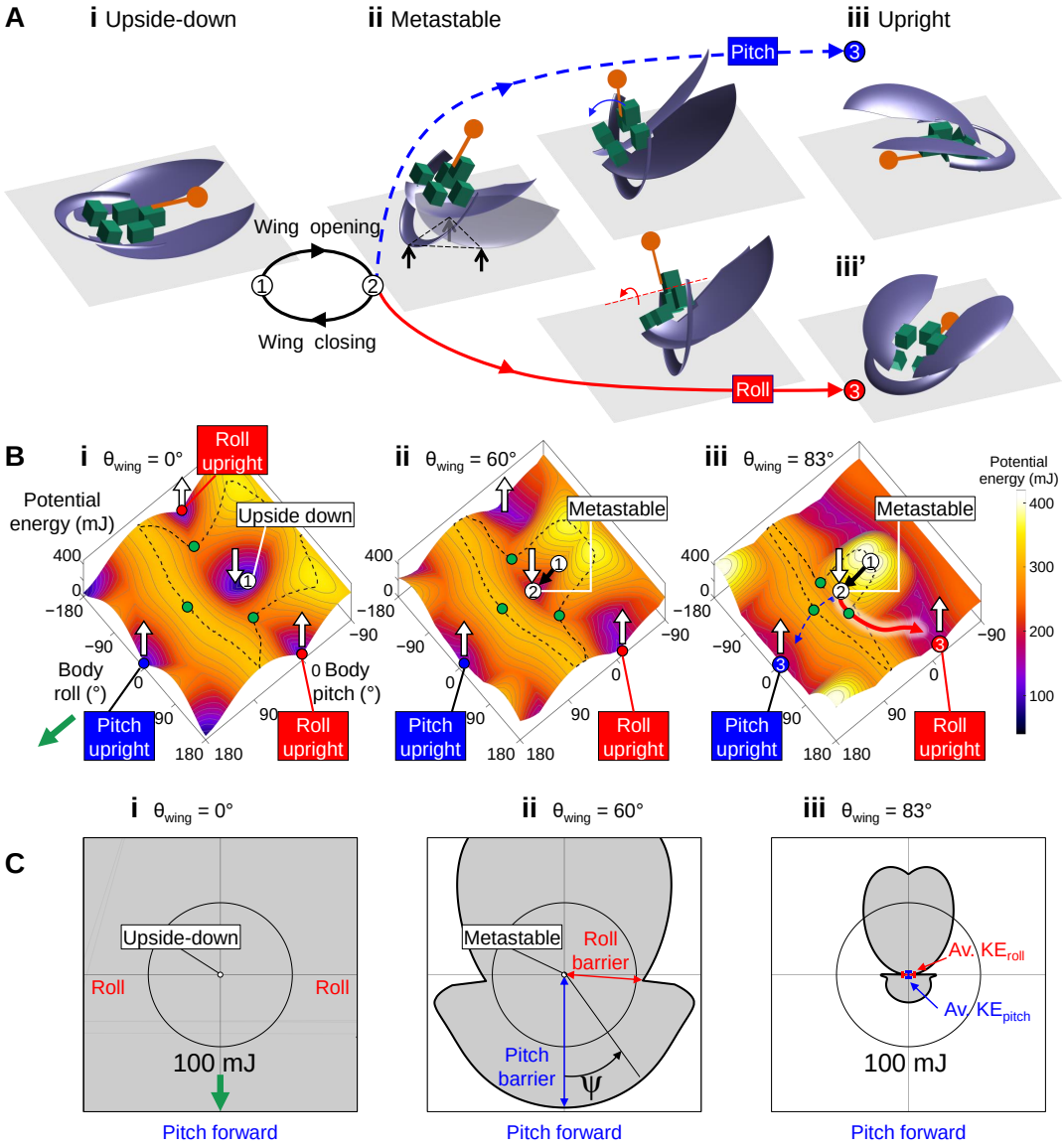
A
i Upside-down
ii Metastable
iii Upright
Pitch
3
Wing opening
1
2
Wing closing
iii'
Roll
3
B
i θwing = 0°
Roll upright
Potential energy (mJ)
Upside down
400
0
−180
−90
Body roll (°)
0
90
180
Body pitch (°)
Pitch upright
Roll upright
ii θwing = 60°
Metastable
iii θwing = 83°
Metastable
Potential energy (mJ)
400
300
200
100
C
i θwing = 0°
Upside-down
Roll
Roll
100 mJ
Pitch forward
ii θwing = 60°
Metastable
Roll barrier
Pitch barrier
ψ
Pitch forward
iii θwing = 83°
Av. KEroll
Av. KEpitch
100 mJ
Pitch forward

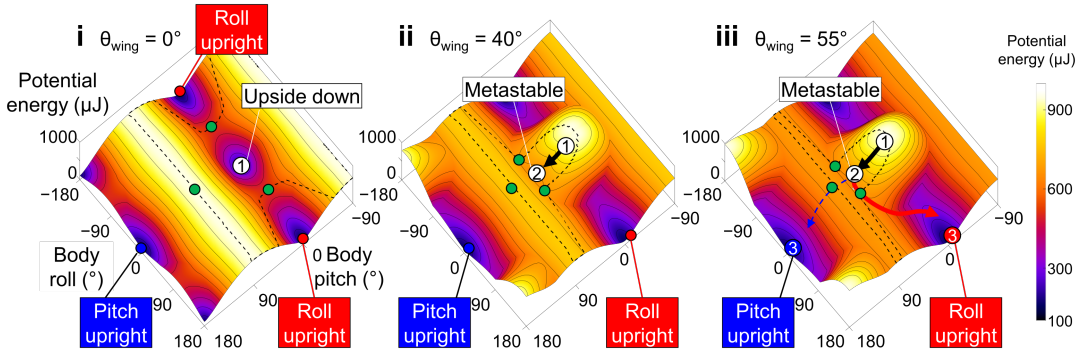

Figure 3.10: Animal's potential energy landscape. Snapshots of potential energy landscape at different wing opening angles. Black curve is representative trajectories of failed attempts and dashed blue and red curves are for successful attempt by pitch mode and self-righting by roll mode, respectively. Thin black curves on landscape are constant potential energy contours. Dashed black curves show boundary of upside-down/metastable basins. Green dots show saddles between metastable basin and the three upright basins. Reproduced from Othayoth and Li, 2021.

3.7.3 Robot self-righting resembles animal's

The robot's winged self-righting behavior resembled that of the discoid cockroach in multiple aspects (Figures 3.1, 3.9A, 3.10). First, it often took the robot multiple attempts (Figure 3.8D) to self-right probabilistically (Figure 3.8C). In addition, as the wings opened, the robot's body pitched up (Figure 3.9Ai), and the head and two opened wings formed a triangular base of support in which the center of mass projection fell (metastable state, Figure 3.9Aii). In failed attempts, after the wings opened fully, the robot was unable to escape this metastable state by either pitching over the head or rolling sideways and fell back to the ground upside-down as the wings closed (Figure 3.9A). In successful attempts, the robot escaped the metastable state and always self-righted by rolling to either side (Figure 3.9Aiii'-iv', red). Moreover, the robot never lifted off the ground during self-righting. Finally, the robot's motion trajectories in the space of body pitch, roll, and center of mass height were stereotyped for both failed and successful attempts (Figures 3.11, 3.12), although they are also stochastic with trial-to-trial variations in body pitch and roll.

3.7.4 Robot and animal have similar evolving potential energy landscapes

For both the animal and robot, the potential energy landscape over body pitch-roll space were similar in shape, and both changed in a similar fashion as the wings opened (Figures 3.9, 3.10). This is expected because the animal and robot were geometrically similar (Table 2). When the wings were fully closed, the potential energy landscape had a local minimum at near zero body pitch and roll (Figure 3.9Bi). This is because either pitching or rolling of the body from being

upside-down increases center of mass height and thus gravitational potential energy. Hereafter, we refer to this local minimum basin as the upside-down basin. The landscape also had three other local minima corresponding to the body being upright . One local minimum at (body pitch, roll) = (180°, 0°) could be reached from the upside-down basin by pitching forward (Figure 3.9A, blue dot). Two local minima at (body pitch, roll) = (0°, ±180°) could be reached by rolling left or right (Figure 3.9Aiii'-iv', red and blue curves are for roll and pitch modes respectively). Hereafter, we refer to these basins as pitch and roll upright basins, respectively. Transition from one basin to another required overcoming the potential energy barrier separating them (Figure 3.9B, dashed black curve). As the wings opened, both the robot's and animal's potential energy landscape and its equilibria changed (Figure 3.9B, 3.10). The upside-down basin evolved into a metastable basin around a local minimum with a positive pitch and zero roll (Figures 3.9Bii, 3.10Aii, white dot). This local minimum corresponded to the metastable state with the triangular base of support (Figures 3.9Aii, 3.1B). The more the wings opened, the higher the pitch of this local minimum was. To self-right via either the pitch (Figures 3.9Aiii-iv, 3.1Aiii-iv) or roll (Figures 3.9Aiii'-iv', 3.1Aiii'-iv') mode, the system state must escape from the metastable basin to reach either the pitch or a roll upright basin (e.g., Figure 3.9Biii, blue and red curves).

3.7.5 Self-righting transitions are destabilizing, barrier-crossing transitions on landscape

Reconstruction of the robot's 3-D motion on the potential energy landscape revealed that its self-righting transitions are probabilistic barrier-crossing transitions (Figure 3.11). Except when the robot was upright, upside-down, or metastable, it was always statically unstable and its system state was strongly attracted to one of these three local minima basins. At the beginning of each attempt, the system state was in the upside-down basin. As the wings opened, it was attracted towards the metastable basin that emerged. In failed attempts, the system state was trapped in the metastable basin and unable to escape it (Figure 3.11, black curves). In successful attempts, it crossed a potential energy barrier (Figure 3.9B, dashed black curve) to escape the metastable basin and reach a roll upright basin (Figure 3.11, white curves). These observations are in accord with the animal's center of mass height measurements at the beginning, maximal pitch, and end of each attempt from the previous study (Li et al., 2019) projected onto the animal's potential energy landscape (Figure 3.2 C, D).

Figure 3.11: Robot state trajectories on potential energy landscape. (A) θ_{wing} = 60°. (B) θ_{wing} = 72°. (C) θ_{wing} = 83°. Columns i and ii show successful (white) and failed (black) self-righting attempts, respectively. n is the number of successful/failed attempts at each θ_{wing}. Note that only the end point of the trajectory, which represented the current state, showed the actual potential energy of the system at the corresponding wing opening angle. The rest of the visualized trajectory showed how body pitch and roll evolved but, for visualization purpose, was simply projected on the landscape surface. Gray lines show energy contours. Green dots show saddles between metastable basin and the three upright basins. Reproduced from Othayoth and Li, 2021.

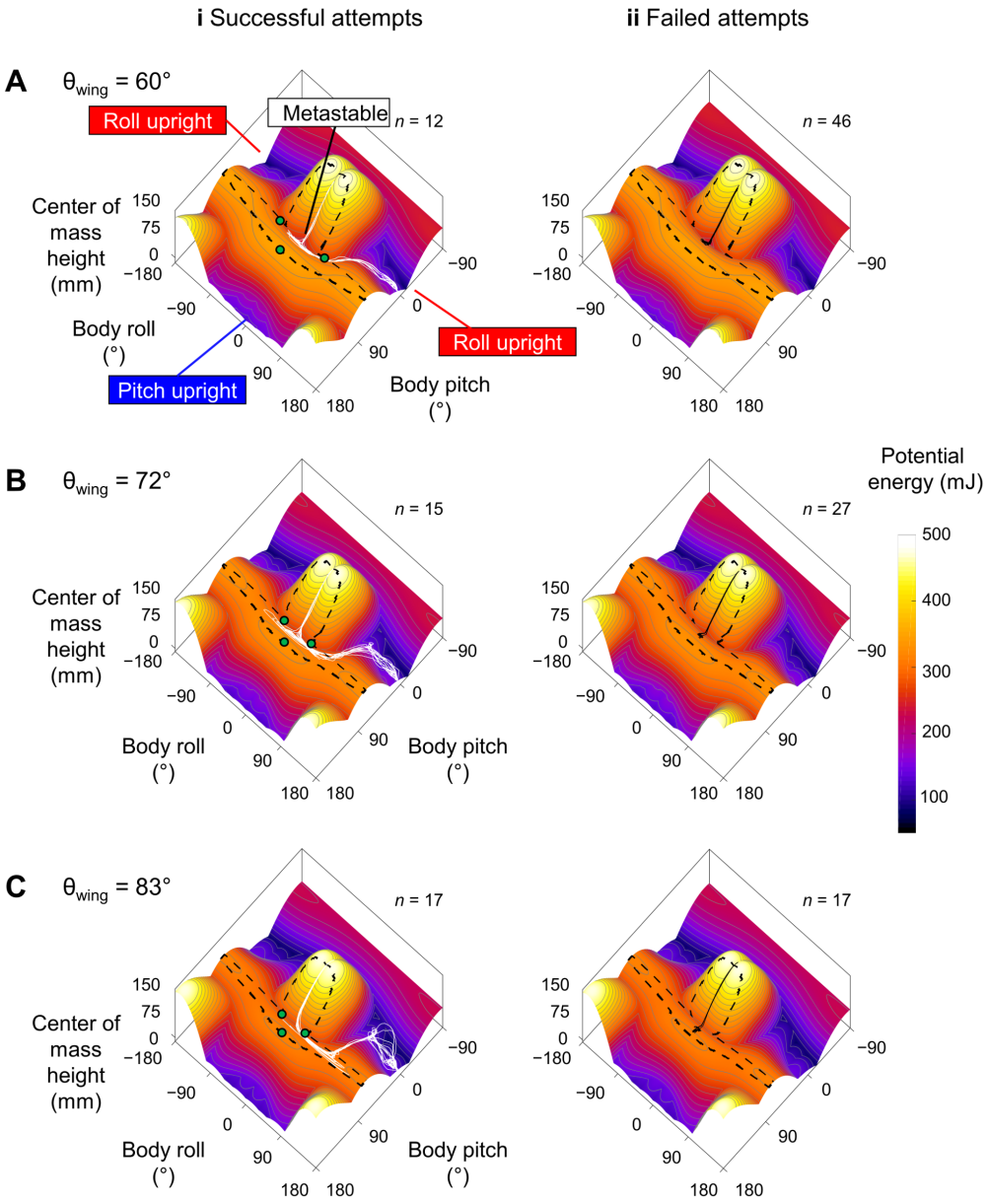
i Successful attempts
ii Failed attempts
A
θwing = 60°
Roll upright
Metastable
n = 12
n = 46
Center of mass height (mm)
150
75
0
−180
Body roll (°)
−90
0
90
180
Body pitch (°)
−90
0
90
180
Pitch upright
Roll upright
B
θwing = 72°
n = 15
n = 27
Potential energy (mJ)
500
400
300
200
100
C
θwing = 83°
n = 17
n = 17

3.7.6 Self-righting via rolling overcomes smaller barrier than via pitching

For both the animal and robot, the potential energy landscape model allowed us to quantify the potential energy barrier for self-righting via the pitch and roll modes. The barrier to escape the metastable state to self-right varied with the direction along which the system moved in the body pitch-roll space (Figures 3.9C, 3.13C, 3.14). We defined the pitch and roll barriers as the minimal barriers to escape from the metastable local minimum towards the pitch and roll upright basins (Figure 3.9C, blue and red arrow). At all wing opening angles up to 90°, the roll barrier was always lower than the pitch barrier (Figures 3.9C, 3.13C, 3.14C).

3.7.7 Barrier reduction by wing opening facilitates self-righting via rolling

For both the animal and robot, as wing opening angle increased, both the pitch and roll barrier decreased monotonically (Figure 3.13C). As the wings opened to the range of θ_{wing} tested (Figure 3.13C, gray band), the pitch barrier was still much greater than the average pitch kinetic energy (Figure 3.13C, 3.14C, solid curve vs. dashed blue line). By contrast, the roll barrier was lowered to a similar level as the average roll kinetic energy (Figure 3.13C, solid curve vs. dashed red line). This explained why the modified animal, with its higher average kinetic energy, self-righted at a higher probability than the intact animal (Figure 3.14 solid vs. dashed lines). These findings demonstrated that, even though wing opening did not generate sufficient kinetic energy to self-right by pitching (Figure 3.13C), it reduced the roll barrier so that self-righting became

possible using small, perturbing roll kinetic energy from leg flailing.

To further confirm this, we compared the robot's kinetic energy with potential energy barrier along the pitch and roll directions respectively during each attempt (Figures 3.15, 3.16). The robot's pitch kinetic energy was insufficient to overcome even the reduced pitch barrier in both failed and successful attempts (Figure 3.16). By contrast, as wing opening and leg flailing amplitudes increased, the robot's roll kinetic energy more substantially exceeded the roll barrier during successful attempts (Figure 3.15; $P < 0.001$, nominal logistic regression), and the surplus enabled it to self-right via rolling.

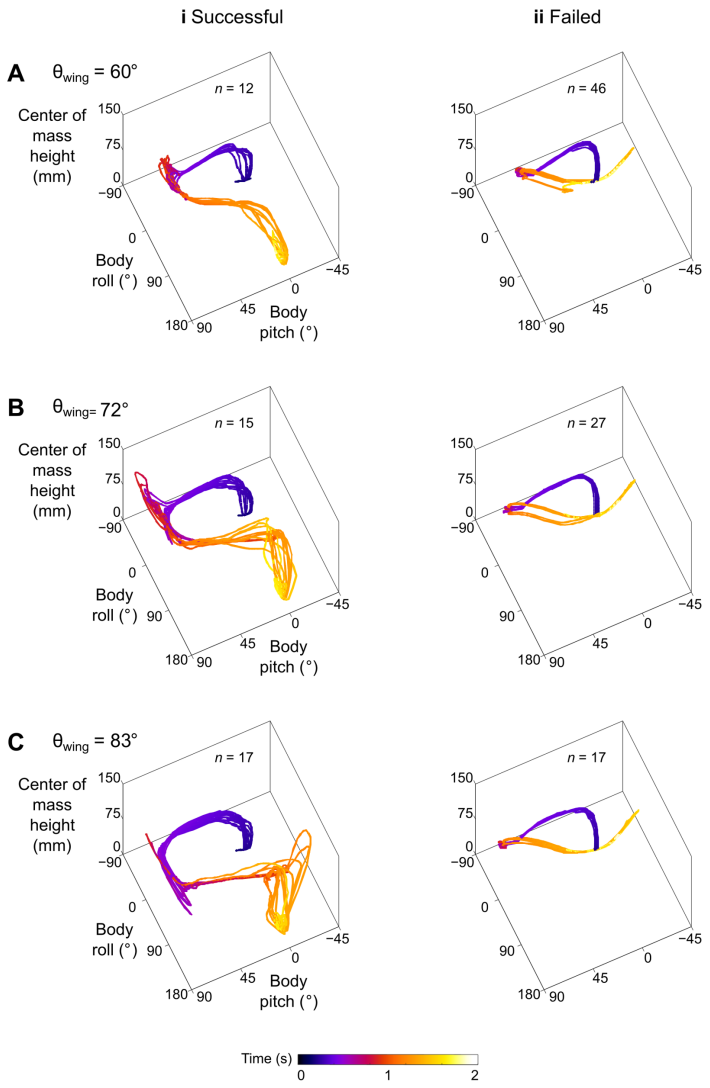

Figure 3.12: Robot's stereotyped body motion during self-righting. State trajectories in body pitch, body roll, and center of mass height space. (A) $\theta_{wing} = 60°$. (B) $\theta_{wing} = 72°$. (C) $\theta_{wing} = 83°$. Columns i and ii show successful and failed self-righting attempts, respectively. n is the number of successful or failed attempts at each θ_{wing}. Reproduced from Othayoth and Li, 2021.

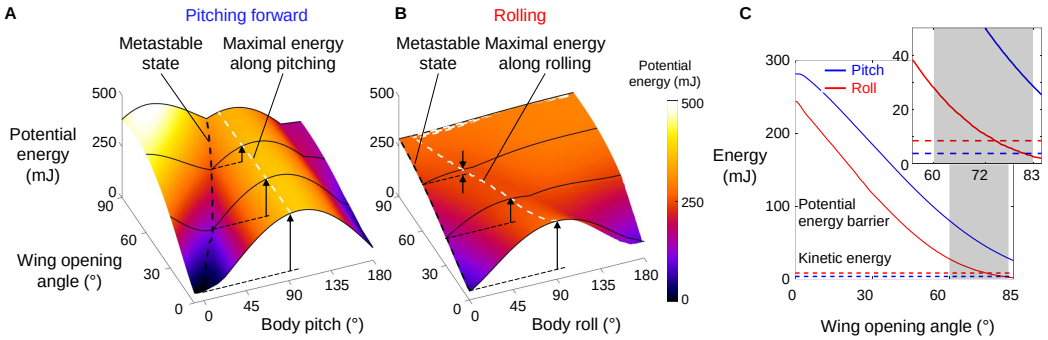

Figure 3.13: Robot's potential energy barriers for self-righting via pitch and roll modes. (A) Potential energy during self-righting via pitch mode as a function body pitch and wing opening angle. (B) Potential energy during self-righting via roll mode as a function of body roll and wing opening angle. Dashed white curves in A and B show energy of metastable state. Dashed black curve in A and B shows maximal energy when pitching forward or rolling from metastable state, respectively. Vertical upward arrows define pitch (A) and roll (B) barriers at a few representative wing opening angles. (C) Pitch (blue) and roll (red) barrier as a function of wing opening angle. Blue and red dashed lines show average maximal pitch and roll kinetic energy, respectively. Gray band shows range of wing opening amplitudes tested. Inset shows the same data magnified to better show kinetic energy. Reproduced from Othayoth and Li, 2021.

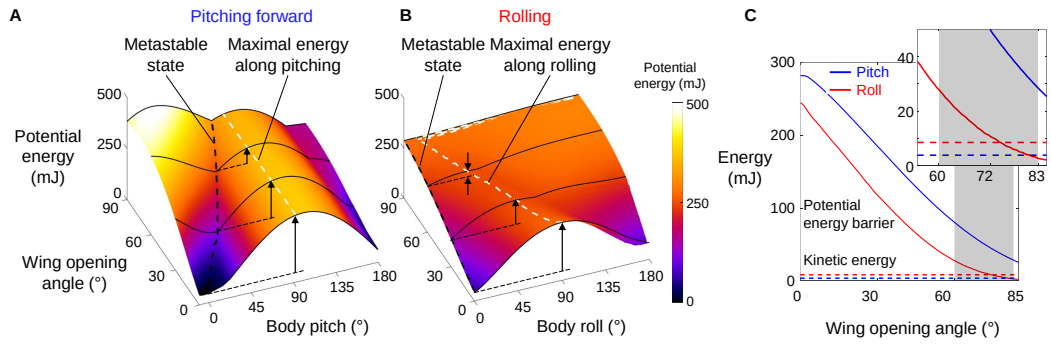

Figure 3.14: Animal's potential energy barriers for self-righting via pitch and roll modes. (A) Potential energy of self-righting via pitch mode as a function body pitch and wing opening amplitude. (B) Potential energy of self-righting via roll mode as a function of body roll and wing opening amplitude. Dashed white curves in A and B show energy of metastable state. Dashed black curve in A and B shows maximal energy when pitching forward or rolling from metastable state, respectively. Vertical arrows define pitch (A) and roll (B) barriers at a few representative wing opening angles. (C) Pitch (blue) and roll (red) barrier as a function of wing opening angle. Dashed and solid horizontal lines show the intact (dashed) and modified (solid) animal's average pitch kinetic energy (blue) and average roll kinetic energy (red), respectively. Inset shows the same data magnified to better show kinetic energy. Reproduced from Othayoth and Li, 2021.

Figure 3.15: Comparison between robot's kinetic energy and potential energy barrier along roll direction. (A) Roll kinetic energy, (B) roll potential energy barrier, and (C) roll kinetic energy minus potential energy barrier along roll direction over time for a representative successful and failed attempt. Between two vertical dashed lines is when wings are held fully open. (D) Surplus along roll direction over time for all attempts from all trials. The attempts are grouped along vertical axis, based on increasing leg oscillation amplitude θ_{leg}. For each θ_{leg}, the attempts are further grouped along by different wing opening amplitudes θ_{wing} (increasing along upward direction). Columns (i) and (ii) are successful and failed attempts. Asterisk indicates significant difference in roll kinetic energy minus potential energy barrier between successful and failed attempts. (E) Average of maximal roll kinetic energy minus potential energy barrier, as a function of wing opening amplitude and leg oscillation amplitude. Red and blue show surplus and deficit of roll kinetic energy minus potential energy barrier, respectively. $n = 134$ attempts. See Figure 7—source data 1 for results of statistical tests. Reproduced from Othayoth and Li, 2021.

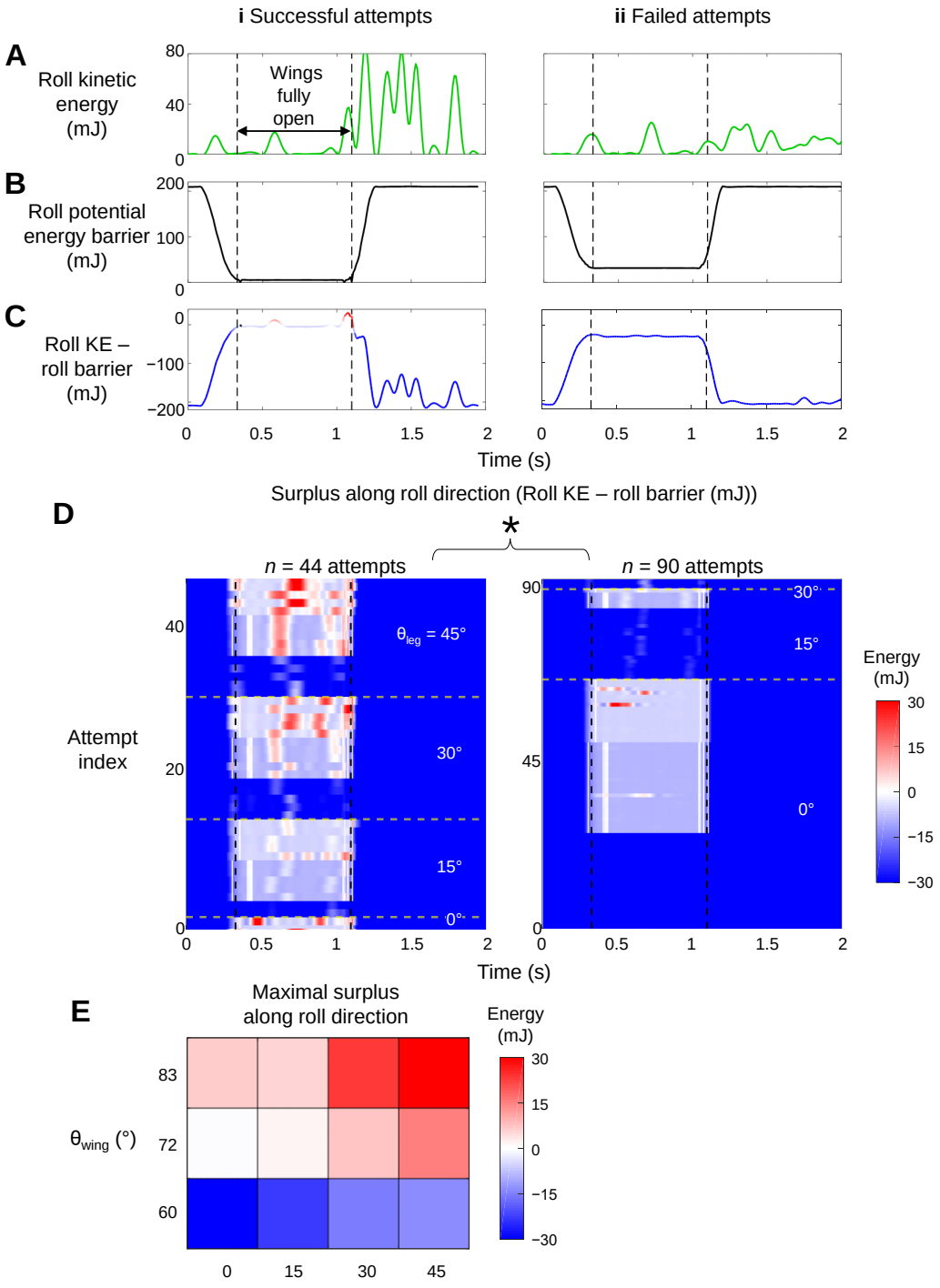
i Successful attempts
ii Failed attempts
A
Roll kinetic energy (mJ)
Wings fully open
B
Roll potential energy barrier (mJ)
C
Roll KE – roll barrier (mJ)
Time (s)
D
Surplus along roll direction (Roll KE – roll barrier (mJ))
*
n = 44 attempts
n = 90 attempts
Attempt index
θleg = 45°
30°
15°
0°
Energy (mJ)
Time (s)
E
Maximal surplus along roll direction
θwing (°)
Energy (mJ)

Figure 3.16: Comparison between robot's pitch kinetic energy and pitch potential energy barrier. (A) Kinetic energy, (B) potential energy barrier, and (C) kinetic energy minus potential energy barrier as a function of time for a representative successful (i) and failed (ii) attempt. Between two vertical dashed lines is when wings are held fully open. (D) Pitch kinetic energy minus potential energy barrier as a function of time of all attempts from all trials. Along vertical axis, attempts are grouped into increasing leg oscillation amplitude θ_{leg}. For each θ_{leg}, attempts are further grouped into increasing wing opening amplitudes θ_{wing}. Columns (i) and (ii) are successful and failed attempts. Asterisk indicates significant difference in pitch kinetic energy minus potential energy barrier between successful and failed attempts. (E) Average of maximal pitch kinetic energy minus potential energy barrier when wings are fully open as a function of θ_{wing} and θ_{leg}. Red and blue show surplus and deficit of pitch kinetic energy minus potential energy barrier, respectively. n = 134 attempts. See Figure 7—source data 1 for results of statistical tests. Reproduced from Othayoth and Li, 2021.

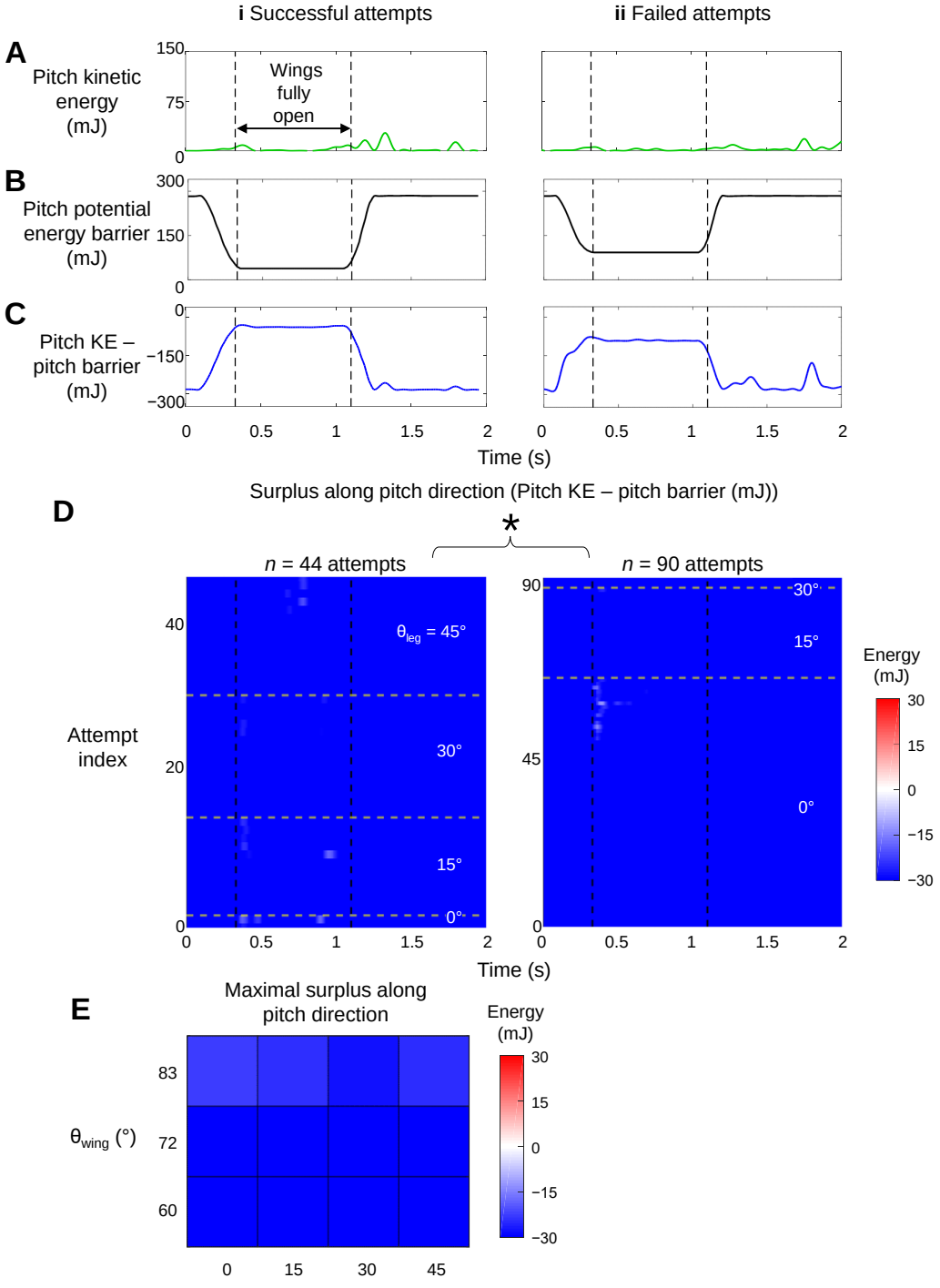
i Successful attempts
ii Failed attempts
A
Pitch kinetic energy (mJ)
Wings fully open
150
75
0
B
Pitch potential energy barrier (mJ)
300
150
0
C
Pitch KE – pitch barrier (mJ)
0
−150
−300
0
0.5
1
1.5
2
Time (s)
D
Surplus along pitch direction (Pitch KE – pitch barrier (mJ))
*
n = 44 attempts
n = 90 attempts
θleg = 45°
30°
15°
0°
Attempt index
40
20
0
90
45
Energy (mJ)
30
15
0
−15
−30
E
Maximal surplus along pitch direction
θwing (°)
83
72
60
0
15
30
45

3.8 Discussion

We integrated animal experiments, robotic physical modeling, and potential energy landscape modeling to discover the physical principles of how the discoid cockroach use propelling and perturbing appendages (wings and legs, respectively) together to achieve strenuous ground self-righting. Ground self-righting transitions are stochastic, destabilizing barrier-crossing transitions on a potential energy landscape. Even though propelling appendages cannot generate sufficient kinetic energy to cross the high potential energy barrier of this strenuous locomotor task, they modify the landscape and lower the barriers in other directions sufficiently so that kinetic energy from perturbing appendages can help cross them probabilistically to self-right. Compared to only using propelling or perturbing appendages alone, using them together makes self-righting more probable and reduces the number of attempts required, increasing the chance of survival.

Although the intact animal's average kinetic energy from hind leg flailing was not sufficient to overcome the potential barrier at the range of wing opening observed, it still self-righted at a small but finite probability (Figure 3.4B). This was likely because of the additional kinetic energy from flailing of fore and mid legs, small forces from legs scraping the ground, as well as abdominal flexion and twisting and passive wing deformation under load (Li et al., 2019), both of which induce lateral asymmetry and tilts the potential energy landscape towards one side and lowers the roll barrier. This consideration further demonstrates the usefulness of co-opting a variety of appendages for propulsion and perturbation simultaneously to achieve strenuous ground self-righting. Such exaptation

(Gould and Vrba, 1982) of multiple types of appendages that evolved primarily for other locomotor functions for self-righting is likely a general behavioral adaptation and should be adopted by terrestrial robots.

3.8.1 Stereotyped motion emerges from physical interaction constraint

Our landscape modeling demonstrated that the stereotyped body motion during strenuous leg-assisted, winged self-righting in both the animal and robot is strongly constrained by physical interaction of the body and appendages with the environment. The stereotyped repeated body pitching up and down during failed attempts and rolling during successful attempts directly result from the strong attraction of the system state to the landscape basins, which directly arise from physical interaction of body/appendages with the ground. This finding suggested that potential energy landscape modeling can be used to understand stereotyped ground self-righting strategies of other species (Ashe, 1970; Domokos and Várkonyi, 2008; Golubović et al., 2013; Li et al., 2019; O'Donnel, 2018) and even infer those of extinct species (analogous to (Gatesy, Bäker, and Hutchinson, 2009)). Similarly, it will inform the design and control of self-righting robots (e.g., Caporale et al., 2020; Kessens, Smith, and Osteen, 2012).

Although only demonstrated in a model system, the potential energy landscape approach can in principle be applied to more complex and different self-righting behaviors, as well as on ground of different properties (Sasaki and Nonaka, 2016), to understand how propelling and perturbing effects work together. For example, as the ground becomes more rugged with larger asperities, the

landscape becomes more rugged with more attractive basins (Figure 3.17). In addition, for leg-assisted, winged self-righting, we can add degrees of freedom for fore and mid leg flailing, abdomen flexion and twisting, and even passive wing deformation due to load (Li et al., 2019) to create fine-grained potential energy landscapes to understand how these motions may emerge from physical interaction constraints. We can also understand legged self-righting by modeling how the legs and deformable abdomen (Li et al., 2019) affect the potential energy landscape when wings are not used. This broad applicability will be useful for comparative studies across species, strategies, and even environments, such as understanding why some cockroach species' self-righting is more dynamic than others (Li et al., 2019). However, this approach does not apply to highly dynamic self-righting strategies, such as those using jumping (Bolmin et al., 2017; Kovac et al., 2008) where kinetic energy far exceeds the potential energy barrier.

3.8.2 Towards potential energy landscape theory of self-righting transitions

The potential energy landscape model here does not describe self-righting dynamics. Recent dynamic modeling using multi-body dynamics simulations (Xuan and Li, 2020b) and dynamical templates (Xuan and Li, 2020a) in our lab revealed that wing-leg coordination affects self-righting by changing the mechanical energy budget (Xuan and Li, 2020a) and that the randomness in the animal's motion helps it self-right (Xuan and Li, 2020b). However, these approaches have their limitations: multi-body dynamic simulations are effectively experiments on a computer; dynamical templates are increasingly challenging to develop as system degrees of freedom increases. Further development of a potential energy

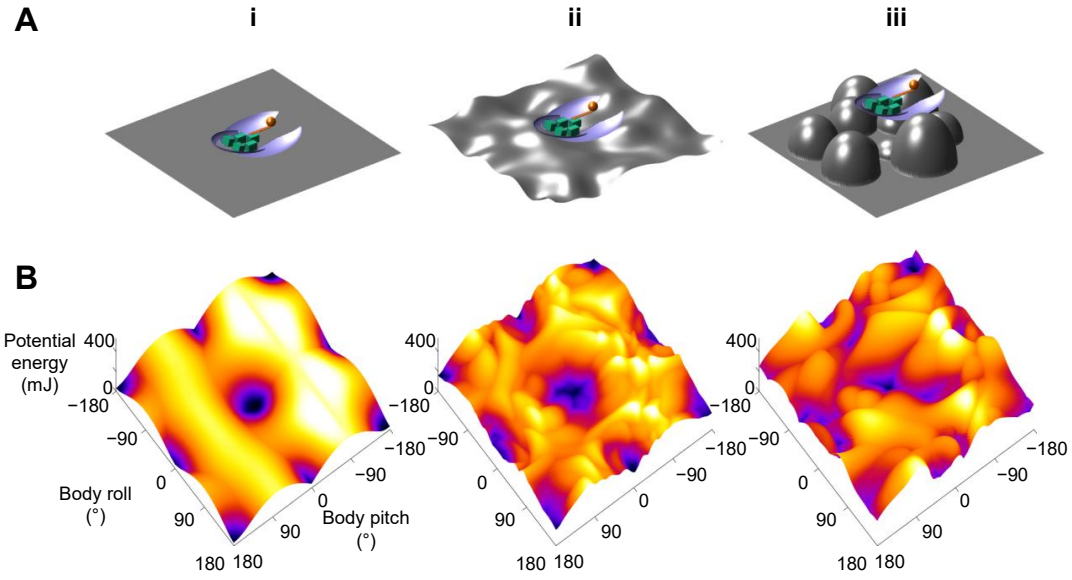

Figure 3.17: Dependence of potential energy landscape on ground geometry. (A) Grounds of different geometry. (i) Flat ground. (ii, iii) Uneven ground with small (ii) and large (iii) asperities compared to animal/robot size. (B) potential energy landscapes for self-righting on corresponding ground. In ii and iii, landscape is not invariant to robot body translation as in i. Landscape is show for robot at the geometric center of the terrain with wings closed. Robot shown for scale. Reproduced from (Othayoth and Li, 2021).

landscape theory that adds stochastic, non-conservative forces to predict how the system "diffuses" across landscape barriers (analogous to Socci, Onuchic, and Wolynes, 1996) may be a relatively simple yet intuitive way to model probabilistic barrier-crossing dynamics.

Chapter 4

Tracking and reconstructing large obstacle interaction of small animals using a terrain treadmill

This chapter is a paper by Ratan Othayoth*, Blake Strebel*, Yuanfeng Han, Evains Francois, and Chen Li (*equal contributions) under review in *The Journal of Experimental Biology* (2021) (Othayoth et al., 2021a).

4.1 Author Contributions

Ratan Othayoth implemented 2-D tracking and 3-D reconstruction, analyzed data, created visualizations, and wrote the paper; Blake Strebel designed and constructed the treadmill, implemented the treadmill control system, and wrote an early draft; Yuanfeng Han designed the treadmill and assisted construction; Evains Francois collected animal data for testing treadmill performance; Chen Li. oversaw the study, designed the treadmill, created visualizations, and wrote the paper.

4.2 Introduction

In nature, terrestrial animals often move through spatially complex, three-dimensional terrain ((Dickinson et al., 2000). Small animals are particularly challenged to traverse many obstacles comparable to or even larger than themselves (Kaspari et al., 1999). By contrast, the majority of laboratory studies of terrestrial locomotion have been performed on flat surfaces (Alexander and Jayes, 1983; Blickhan and Full, 1993; Cavagna, Thys, and Zamboni, 1976; Diederich, Schumm, and Cruse, 2002; Ferris, Louie, and Farley, 1998; Full and Tu, 1990; Koditschek, Full, and Buehler, 2004; Li, Hsieh, and Goldman, 2012; Minetti et al., 2002; Moritz and Farley, 2003; Spagna et al., 2007; Spence et al., 2010), either rigid or with various surface properties (friction, slope, solid area fraction, stiffness, damping, ability to deform and flow, etc.).

Recent laboratory studies have begun to advance our understanding of animal locomotion in complex terrain with obstacles (Birn-Jeffery and Daley, 2012; Blaesing, 2004; Collins et al., 2013; Daley and Biewener, 2006; Dürr and Schilling, 2018; Gart et al., 2018; Gart and Li, 2018; Harley, English, and Ritzmann, 2009; Kohlsdorf and Biewener, 2006; Li et al., 2015; Olberding, McBrayer, and Higham, 2012; Parker and McBrayer, 2016; Sponberg and Full, 2008; Theunissen, Vikram, and Dürr, 2014; Tucker and Mcbrayer, 2012). Because of typical laboratory space constraints, the terrain arenas used in these studies are usually no larger than a few dozen body lengths in each dimension. Thus, they only allow experiments at relatively small spatiotemporal scales beyond 10 body lengths and 10 movement cycles. It remains a challenge to study animal locomotion in complex 3-D terrain with large obstacles at larger

spatiotemporal scales.

Experiments at large spatiotemporal scales are usually realized by treadmills to keep the animal (including humans) stationary relative to the laboratory (Buchner et al., 1994; Darken, Cockayne, and Carmein, 1997; Full, 1987; Herreid and Full, 1984; Jayakumar et al., 2019; Kram et al., 1998; Stolze et al., 1997; Watson, Ritzmann, and Pollack, 2002; Weinstein and Full, 1999). However, only small obstacles can be directly mounted on such treadmills (Voloshina et al., 2013); larger obstacles have to be dropped onto the treadmill during locomotion (Park, Wensing, and Kim, 2015; Snijders et al., 2010). Furthermore, such linear treadmills allow only untethered movement along one direction. Alternatively, spherical treadmills use lightweight spheres of low inertia suspended on air bearing (kugels) to allow small animals to rotate the spheres as they freely change their movement speed and direction, (Bailey, 2004; Okada and Toh, 2000; Ye, Dowd, and Comer, 1995). However, the animal is tethered, and obstacles cannot be used.

Previous members of our lab created a terrain treadmill (Figure 4.1A, B) that enabled large spatiotemporal scale, high-resolution observations of small animal locomotion in complex terrain with large obstacles. The terrain treadmill design was inspired by a celestial globe model. The terrain treadmill consists of a transparent, smooth, hollow, outer sphere rigidly attached to a concentric, solid, inner sphere using a connecting rod (Figure 4.1A). Terrain modules can be attached to the inner sphere (Figure 4.1) to simulate obstacles that small animals encounter in natural terrain. The outer sphere is placed on an actuator system consisting of three actuated omni-directional wheels (Figure 4.1A). An overhead camera captures videos of the animal moving on top of the inner

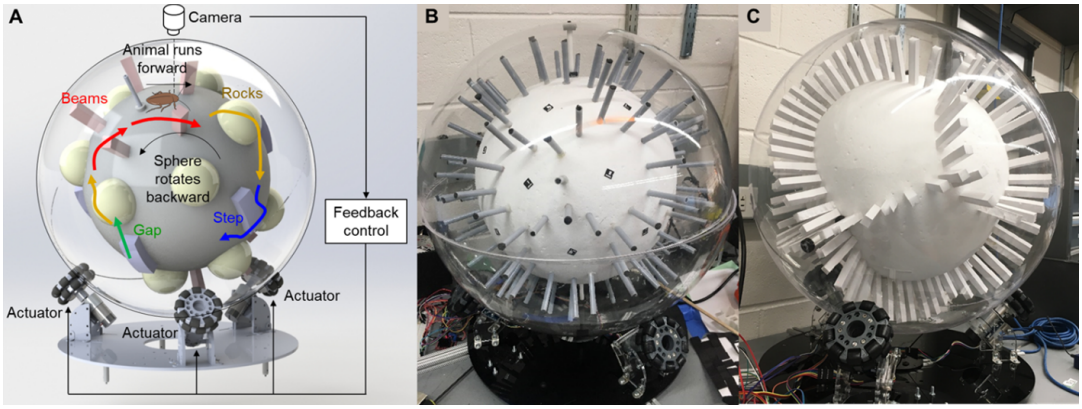

Figure 4.1: Terrain treadmill. (A) Design of terrain treadmill. Colored elements show example modular terrain that can be used. (B, C) Terrain treadmill, with (B) sparsely and (C) densely spaced vertical pillars as example terrain modules. ArUCo markers attached on the inner sphere are also shown in (B, C). The treadmill was designed and manufactured by Blake Strebel and Yuanfeng Han. Images courtesy of Blake Strebel.

sphere, with an ArUCo (Garrido-Jurado et al., 2014) marker attached on its body. The animal's position estimated from tracking the marker is used by a feedback controller to actuate the connected spheres with the opposite velocity to keep the animal on top (Figure 4.3D, E) as it moves through the obstacle field (Figures 4.3A-C, 4.4A, B,).

We used discoid cockroaches (*Blaberus discoidalis*) to test the treadmill's ability to elicit free locomotion and measure animal-terrain interaction over large spatiotemporal scales. We put the animal inside the outer sphere and then sealed it. To pick and place the animal onto the inner sphere, we attached a square magnet (16mm side length, 3.5g) on the animal's dorsal side, with an ArUCo marker attached to it for tracking (4.4A, B). We used a larger magnet to pick up and move the animal to the top of the treadmill and dropped it onto the inner sphere. We then started the control program to keep the animal on

top. The images recorded by the camera were then sent to the ROS program, which first saved each frame in its native format (a bagfile) and then processed the image to track the marker position. Based on the tracked and then filtered marker position, which were used to calculate the velocity of the animal through forward kinematics, motor velocities required to keep the animal centered on were calculated and commanded to the motors.

The terrain treadmill elicited sustained locomotion of discoid cockroaches (N = 5 animals, n = 12 trials, sparse obstacles) through both sparse (Figure 4.1B) and cluttered (Figure 4.1C) pillar obstacle. Even with cluttered obstacles, where gaps between obstacles were smaller than animal body width, the treadmill was able to elicit continuous trials, in which the animal moved through pillars for 25 minutes ($\approx$ 2500 stride cycles) over 67 m ($\approx$ 1500 body lengths). For 83% of the experiment duration, the terrain treadmill contained the animal within a circle of radius 4 cm (0.9 body length) centered about the image center (Figure 4.2D, E) even at locomotion speeds of up to 10 body length/s (peak speed of 50 cm/s). A Kalman filter (Harvey, 1990) estimated the position of animals and reduced the noise and error in marker tracking. The Kalman filter continued to estimate the animal's position even when the marker was obscured from body rolling (Figure 4.3A) or the outer sphere's seam. In addition, the animal freely explored and visited almost the entire obstacle field (Figure 4.4C, D).

4.3 Methods

My specific contribution to this work was that I developed methods for tracking and reconstruction of 3-D motion during large obstacle interaction of small animals. These methods enabled estimation of different metrics such as body velocities and antennal planar orientation relative to the body heading (Figures 4.4, 4.2,).

4.3.1 Data analysis

Previously, after each experiment, the recorded images were saved as bagfiles. The bagfiles were retrieved processed using custom MATLAB code to extract the saved images for post processing.

4.3.2 Measuring animal movement in obstacle field

To measure the animal's movement relative to the pillar obstacle field, we first measured the movement of the pillar obstacle field (i.e., treadmill rotation) relative to the camera. We attached 31 ArUCo markers to the inner sphere, with one each at the center of hexagonal and pentagonal regions of the soccer ball pattern projected on the sphere (Figure 4.2A). We then separately created a map of all markers attached on the inner sphere (referred to as marker map) using ArUCo Marker-mapper application. Because each marker and its four corners were fixed relative to the coordinate frame attached to the inner sphere (i.e., T_3 is known, Figure 4.2A), when one of the markers on sphere is tracked (i.e., T_1 can be measured, Figure 4.2A), the relative pose between sphere body frame and the camera (Figure 4.2A, T_4) can be computed. When more than

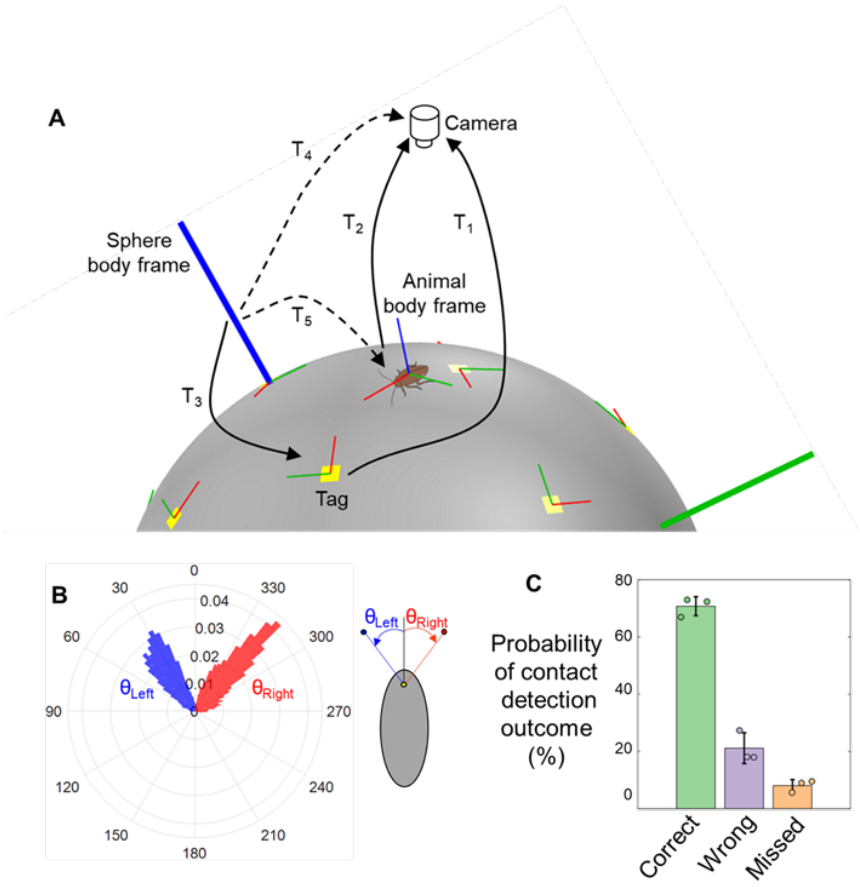

Figure 4.2: Measuring motion of animal exploring sparse pillar fields. (A) Coordinate frame transformation to measure animal motion relative to sphere. Solid black arrows are relative 3-D poses (T_1, T_2 and T_3) that are known or measured directly from acquired images. Dashed arrows are the two relative 3-D poses (T_4 and T_5) that are calculated from measurements to obtain animal motion relative to the sphere. Yellow squares with red and green lines show the markers attached to the sphere and their x and y axes, respectively. Thick green and blue lines show the y and z axes of the frame attached to the inner sphere. (B) Histogram of left (θ_{left}, blue) and right (θ_{right}, red) antenna planar orientation relative to body heading (see schematic on right for definition). (C) Accuracy of antenna-pillar contact detection outcomes. $N = 3$ animals, $n = 3$ trials. Reproduced from Othayoth et al., 2021a.

one marker on the sphere is detected, relative pose of sphere and camera can be computed by solving the Perspective-n-points problem (Lepetit, Moreno-Noguer, and Fua, 2009), which estimates camera pose from a known set of 3D points (marker corners) and the corresponding 2D coordinates in the image. The 'solvePnP' program in in image processing toolboxes in MATLAB or OpenCV may be used to for this purpose. Because the animal's movement relative to the camera (Figure 4.2A, T_2) is directly available from tracking via the calibrated camera, the animal's pose relative to the sphere body frame and hence relative to the terrain obstacle field can be calculated (Figure 4.2A, T_5). Because the ArUCo marker attached to the animal is not necessarily at its center of mass, a constant position and orientation offset must be manually determined and added.

4.3.3 Unwrapped 2-D trajectory

Considering that the sphere diameter is $\approx 9\times$ that of animal body length, we approximated the immediate region surrounding the animal to be flat and estimated the animal's equivalent 2-D planar trajectory. To obtain the 2-D trajectory, we integrated the body forward and lateral translational velocities and body yaw angular velocity (Figure 4.4F-G) over time, with the initial position at origin and body forward axis along x axis. Because during portions of a trial the animal body marker was not tracked for a long duration, we did not consider those video frames. As a result, each trial was assumed to be composed of multiple segments, and each of their equivalent 2-D trajectories were assumed to have the same initial conditions as described above (Figure 4.4E).

4.4 Results

4.4.1 Free locomotion at large spatiotemporal scales

For 83% of the experiment duration, the terrain treadmill contained the animal within a circle of radius 4 cm (0.9 body length) centered about the image center (Figure 4.2D, E) even at locomotion speeds of up to 10 body length/s (peak speed of 50 cm/s). In addition, over the course of 12 trials, the animal freely explored and visited almost the entire obstacle field (Figure 4.4C, D). Finally, the animal's motion relative to the treadmill was used to estimate metrics such as body velocity components (Figure 4.2F-H), antenna planar orientation relative to the body heading (Figure 4.2B), and unwrapped 2-D trajectories (Figure 4.4E).

4.4.2 Animal-obstacle interaction

We measured and reconstructed the animal-terrain interaction for 12 trials in which the animal freely explored the sparse obstacle field (Figure 4.4). The ArUCo markers attached on the animal and the inner sphere, allowed measuring and reconstructing animal motion relative to obstacle field (see 'Measuring animal movement in obstacle field' in Methods). Because lighting was not optimized, the pillar shadow resulted in substantial variation of the background, and because the left and right antenna are visually similar and often moved rapidly, automated antenna tracking was accurate in only $\approx$ 40% of frames after rejecting inaccurately tracked data (see 'Automated animal tracking' in Methods). However, this can be improved with refinement of our experimental setup in future (see Discussion).

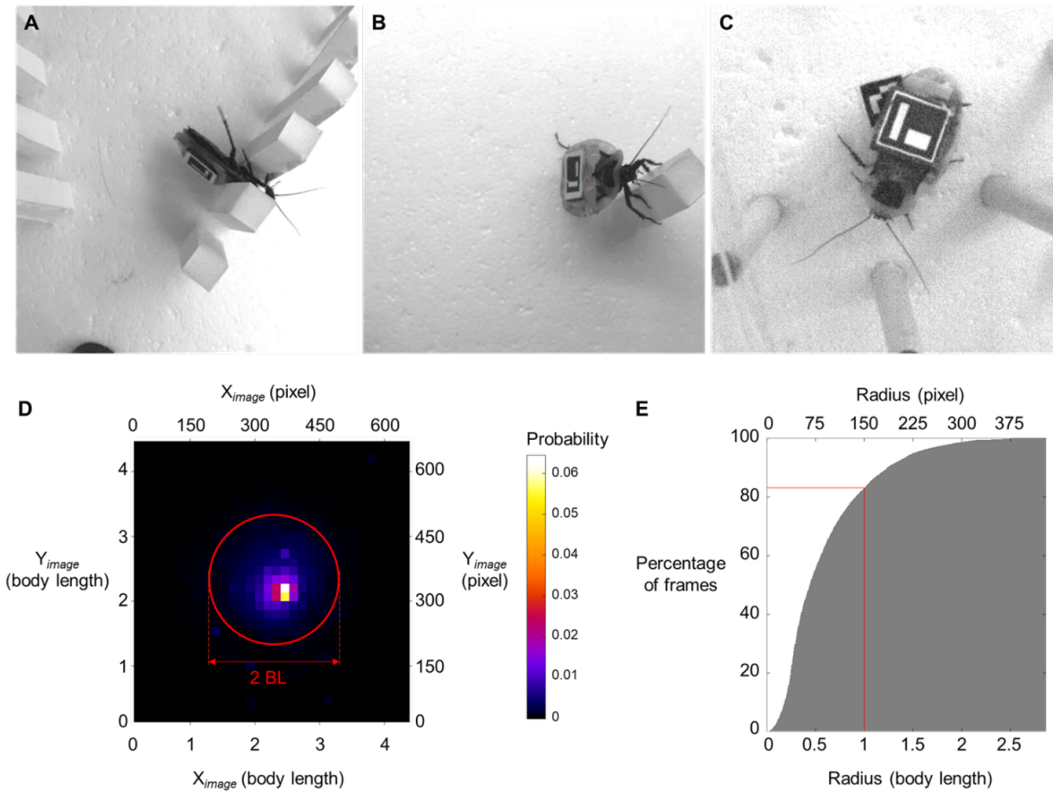

Figure 4.3: Animal behavior and performance of the treadmill. (A-C) Representative snapshots of behaviors including (A) body rolling, (B) body pitching and pillar climbing, and (C) antennal sensing observed during free exploration of terrain. (D) Probability of animal's detected location in the image. Red circle of radius 2 animal body lengths is centered at the image center. (E) Cumulative histogram of animal's radial position (in body lengths) from the center of the image. Vertical and horizontal red lines show a radius of red circle in (A) and the percentage of frames in which animal's position was maintained within this circle. $N = 5$ animals, $n = 12$ trials. Reproduced from Othayoth et al., 2021a.

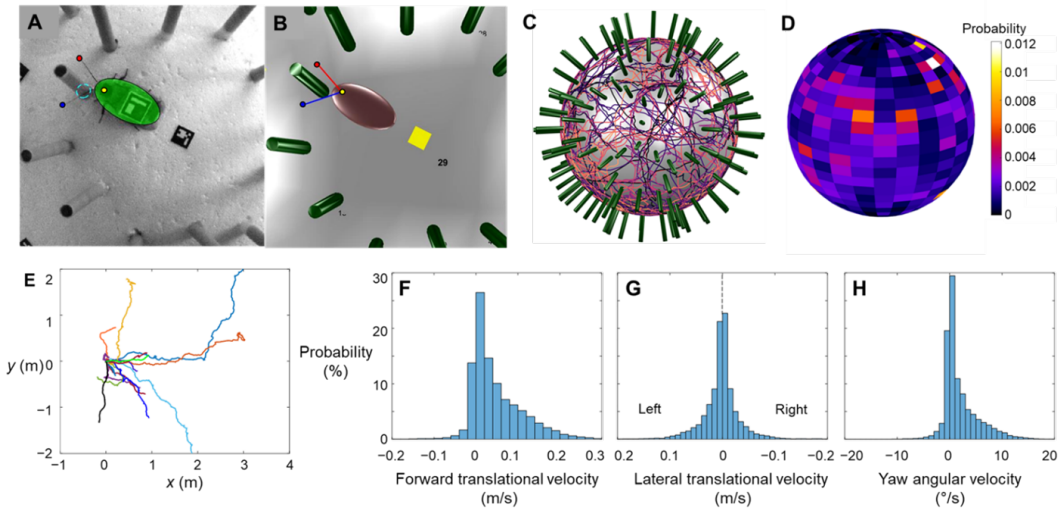

Figure 4.4: Representative metrics and 3-D reconstruction of animal exploring sparse pillar obstacle field. (A, B) Representative snapshot and reconstruction of animal moving through sparse pillar obstacle field. Transparent green ellipsoid in (A) and brown ellipsoid in (B) show approximated animal body. Red and blue dots show antenna tips. Yellow dot shows the tracked point on animal's head. Dashed cyan circle is the base of the two pillars with which the animal's antenna is interacting. (C, D) Ensemble of trajectories (D) and probability density distribution of animal center of mass (E) during free exploration of sparse pillar obstacle field, $N = 5$ animals, $n = 12$ trials. (E) Unwrapped 2-D trajectories of animal, obtained by integrating forward and lateral translational velocities and yaw angular velocity over duration of trial. (F-H) Histogram of animal's (F) forward and (G) lateral translational velocities and (H) yaw angular velocity. Reproduced from Othayoth et al., 2021a.

We then detected which pillar the animal's antennae contacted (Figure 4.4A, B) by measuring the minimum distance from each antenna to all nearby pillars. To determine which pillar the antenna interacted with, we determined whether any pillars where within 3 cm from both antennae and which among them were closest to both antennae. We also manually identified the antenna pillar contact, which served as the ground truth. The antenna-pillar contact detected automatically was accurate in over 70% of the contact instances (Figure 4.2C).

4.4.3 Multiple behaviors and behavioral transitions

In addition to walking or running while freely exploring the obstacle field, the animal displayed other behaviors during interaction with the terrain. For example, when moving in dense obstacle field, the animal often rolled its body in to the narrow gap between the pillars (Figure 4.3A) to traverse and occasionally climbed up the pillars Figure 4.3B). In sparse obstacle field, the animal often swept its antennae during free exploration (Figure 4.3C). The animal also transitioned between these behaviors and occasionally stopped moving.

4.5 Discussion

A reconfigurable laboratory platform allowed large spatiotemporal scale measurements of small animal locomotion through complex terrain with large obstacles. Compared to existing locomotion arenas, our device increased the limits of experiment duration by $\sim 100\times$ and traversable distance by $100\times$. Such large spatiotemporal scales may be useful for studying spatial navigation and memory (Collett, Chittka, and Collett, 2013; Varga et al., 2017) in terrain with large obstacles, and the larger spatial resolution may be useful for studying interaction of the animal (body, appendages, sensors) with the terrain in detail (Cowan, Lee, and Full, 2006; Dürr and Schilling, 2018; Okada and Toh, 2006). There may also be opportunities to advance neuromechanics of large obstacle traversal by combining the terrain treadmill with miniature wireless data backpacks (Hammond et al., 2016) for studying muscle activation (Sponberg and Full, 2008) and neural control (Mongeau et al., 2015; Watson, Ritzmann, and Pollack, 2002). The treadmill design may be scaled down or up to suit animals (or robots) of different sizes. Our treadmill enables large spatiotemporal scale studies of how locomotor behavior emerges from neuromechanical interaction with terrain with large obstacles.

Our study is only a first step and the terrain treadmill can use several improvements in the future to realize its potential. First, we will add more cameras from different views to minimize occlusions and diffused lighting from different directions to minimize shadows, as well as increase camera frame rate to accommodate rapid antenna and body movement, to achieve more reliable tracking of the animal body and antenna through cluttered obstacles during which 3-D body

rotations are frequent. Second, feedback control of the sphere can be improved to use not only position but also velocity of the animal to better maintain it on top. This will be particularly useful if the animal suddenly accelerates or decelerates when traversing obstacles. Furthermore, for longer duration experiments, animal could be perturbed when at rest to elicit movement by automatically moving the treadmill. Finally, we need to take into account how locomotion on the spherical treadmill may affect the animal's sensory cues as compared to moving on stationary ground (Buchner et al., 1994; Stolze et al., 1997)

Chapter 5

Conclusion

5.1 General remarks

In this dissertation, we reported the results of integrated biological, robotic, and physics studies of beam obstacle traversal and ground self-righting. The reported results supported the hypotheses of physical interaction-mediated locomotor transitions that were proposed in Section 1.3.5.

5.1.1 Summary of contributions

The results reported in this dissertation demonstrated the following:

1. Locomotor transitions in beam traversal and self-righting were barrier-crossing transitions on potential energy landscapes (Chapters 2 and 3).

2. Physical interaction during beam obstacle traversal and self-righting was stochastic and led to strong attraction of system state trajectories to the landscape basins (Chapters 2 and 3).

3. Physical interaction via some modes were easier (terradynamically favorable) in both beam traversal and self-righting (Chapters 2 and 3).

4. In both beam traversal and self-righting, the system remained in a favorable mode, or transitioned to a more favorable mode when kinetic energy fluctuation from oscillatory self-propulsion are comparable to the potential energy barrier to be overcome (Chapters 2 and 3). For example, when traversing stiff beams (Chapter 2), animals and robots were more likely to transition to roll mode, as pitch mode required pushing down stiff beams, which was physically difficult. By contrast, animals and robots traversed flimsy beams by pushing them down (pitch mode).

5. When kinetic energy fluctuation was not sufficient to overcome potential energy barrier, changing system configuration lowered potential energy barrier to the levels of available kinetic energy fluctuation, that then induced transition (Chapter 3).

6. Tracking and reconstruction methods developed for an existing 3-D terrain treadmill began to help quantify animal-environment physical and sensory interaction at larger spatiotemporal scales (Chapter 4).

5.1.2 Stereotypyed locomotor transitions

Locomotor modes in both beam traversal (pitch and roll) and self-righting (metastable and roll) are strongly attracted to energy basins on potential energy landscapes, leading to stereotypy in locomotor modes, transitions, and system state trajectories on landscape. Stereotypy emerges directly from animals' and robots' mechanical (and likely neural) systems directly interacting with the physical environment under constraints. In traversal of stiff beams, the animal and the robot are constrained to pitch-up into the gap due to the large

restoring forces from beam deflection.Similarly in self-righting, the metastable triangular base of support that emerges from wing opening constrains the robot from pitching or rolling, but sufficient kinetic energy can induce body rolling. Variations in movement in both model systems lead to stochastic transitions resulting in beam traversal and self-righting and can be advantageous—in our case, for traversal and self-righting—when locomotor behavior is separated into distinct modes.

5.1.3 Kinetic energy: Fluctuation versus Pumping

Kinetic energy fluctuation is usually considered as adverse to the robot performance. Our discovery of kinetic energy fluctuation-driven locomotor transitions suggest that the kinetic energy fluctuation from oscillatory self-propulsion may prove useful to a certain degree when moving in unpredictable natural environments with beam-like obstacles or self-righting; of course, too large a variation or fluctuation may begin to affect robot control. For example, passive vibrations have been shown to facilitate robotic parts alignment (Mohri and Saito, 1994; Swanson, Burridge, and Koditschek, 1995).

We also note that kinetic energy fluctuation is only one possible way to induce transitions. They may also be induced by control strategies that accumulate or "pump" mechanical energy in the system, which can be converted to kinetic energy to induce transitions. For example, previous studies of underactuated robot arms have proposed control strategies in which mechanical energy pumped into the system is appropriately exchanged between system kinetic and potential energies to reach the desired configuration (Spong, 1995; Nakanishi, Fukuda, and Koditschek, 2000). Recently, another study in our lab

(Xuan and Li, 2020a) demonstrated a similar energy accumulation strategy to achieve self-righting.

5.2 Future directions

While the investigation in this dissertation have addressed a few of the knowledge gaps, more questions have been raised than those answered. Here I briefly mention some of the related directions that I find intriguing and are possible extensions of the studies in this dissertation.

5.2.1 Neuromechanical interaction during locomotor transitions

The studies in this dissertation (Othayoth and Li, 2021; Othayoth, Thoms, and Li, 2020) focused on locomotor transitions in the feedforward regime of locomotion (Dickinson et al., 2000; Nishikawa et al., 2007), by eliciting transitions during escape responses in which the role of sensory feedback is diminished due to the inherent neuromechanical delays (Sponberg and Full, 2008). However, an interesting observation from cockroach beam obstacle traversal was that the animal can make barrier-crossing transitions even if kinetic energy fluctuation was not sufficient to overcome potential energy barriers (Chapter 2, Figure 2.17) (Othayoth, Thoms, and Li, 2020). This suggests that transitions may be facilitated by sensory feedback (see Section 5.2). Following this, a recent study from our lab led by Yaqing Wang (Wang, Othayoth, and Li, 2021) demonstrated that during beam traversal cockroaches actively adjust body and appendages which facilitates locomotor transitions.

In addition to these active adjustments, cockroaches may integrate information from antennal sensing (Cowan, Lee, and Full, 2006; Mongeau et al., 2014; Mongeau et al., 2015) and body and leg proprioception (Watson and Ritzmann, 1997; Tuthill and Azim, 2018; Tuthill and Wilson, 2016) during their locomotion (Dickinson et al., 2000; Nishikawa et al., 2007; Holmes et al., 2006). An interesting question that is yet to be answered is how various information from neural and mechanical sensory modalities are integrated (Dickinson et al., 2000; Mongeau et al., 2021; Roth et al., 2016) to elicit or avoid locomotor transitions.

5.2.2 Decision making in natural environments

In addition to animals' internal states (Calhoun, Pillow, and Murthy, 2019) (such as hunger and fear) and the perceived external cues (Kennedy et al., 2014; McFarland, 1977) such as incoming predators and escaping prey, their neuromechanical interaction with the environment (Dickinson et al., 2000) may also influence decision-making in animals (McFarland, 1977). Depending on its goals such as predation, migration, and evasion, an animal must vary its physical interaction with the environment to use the appropriate locomotor modes. For example, during escape responses, transitioning to modes that require overcoming higher potential energy barrier may be terradynamically unfavorable but beneficial by reducing the risk of predation. By contrast, during free exploration of environment during foraging (Viswanathan et al., 2011), an animal may choose to make transitions to access ecological patches with more resources (Fryxell et al., 2008). Conversely, goals may be altered based on the outcome of physical interaction. For example, loss of foothold triggers self-righting response in cockroackes (Sherman, Novotny, and Camhi, 1977). Combining models that

consider the effects of risk (Latty and Beekman, 2010) and rewards (Gillette et al., 2000) perceived by animals with those of physical interaction (e.g., biomechanical templates and anchors (Full and Koditschek, 1999), potential energy landscapes (Othayoth et al., 2021b)) may help better understand how decision making emerges in natural environment. Recent data-driven and optimization-based approaches have begun to represent internal states (Calhoun, Pillow, and Murthy, 2019) and biomechanical risk (Hackett et al., 2020) and hold promise towards understanding the principles of decision making in animals.

5.2.3 Detecting and leveraging terrain affordances

Animals moving in complex natural environments often use physical interaction with terrain components to make locomotor transitions. However, physical interaction in cluttered, obstacle-laden terrain have been traditionally deemed as unfavorable or hostile for robots. As a result, obstacle avoidance (Khatib, 1986) has been the focus of various robot motion planning approaches (Latombe, 2012).

However, obstacles in terrain may be used to generate propulsion (Transeth et al., 2008; Liljeback et al., 2011; Greer et al., 2018; Selvaggio et al., 2020; Qian and Koditschek, 2020). Terrain elements present surfaces against which an animal or a robot can exert forces. Such contact with terrain components deemed as obstacles are often different from those afforded by flat ground (Blickhan and Full, 1993; Holmes et al., 2006) and may have additional advantages. Development of tractable physics models predictive to predict the desired forces (Astley et al., 2020; Holmes et al., 2006; Li, Zhang, and Goldman, 2013) combined with intelligent terrain detection and planning algorithms (Bermudez et al., 2012;

Wu et al., 2016) may enable robots to leverage the affordances provided by their environment to make effective physical interaction and robust locomotor transitions.

5.3 Closing remarks

Working towards the projects explored in this dissertation have helped changed my outlook on doing science and engineering, and to a certain extent, life. These studies gave me an opportunity to acquaint myself with fascinating topics in fields both related and unrelated to locomotion. More importantly, it gave me an opportunity to meet and learn from amazing people of diverse backgrounds. In hindsight, some plans never materialized; some were "not great, but not terrible"; but I'd like to think that most of them worked out better than I anticipated. Nevertheless, it has been a reasonably constructive endeavor for me! I wrap up with a quote from the Twelfth Doctor:

"*Things end. That's all. Everything ends, and it's always sad. But everything begins again too, and that's... always happy. Be happy.*"

References

Aguilar, J. and D.I. Goldman (2016). "Robophysical study of jumping dynamics on granular media". In: *Nat Phys* 12, 278–283. DOI: 10.1038/nphys3568.

Aguilar, J., T. Zhang, F. Qian, M. Kingsbury, B. McInroe, N. Mazouchova, C. Li, R. Maladen, C. Gong, M. Travers, R.L. Hatton, H. Choset, P.B. Umbanhowar, and D.I. Goldman (2016). "A review on locomotion robophysics: The study of movement at the intersection of robotics, soft matter and dynamical systems". In: *Reports Prog Phys* 79.110001. DOI: 10.1088/0034-4885/79/11/110001.

Alexander, R.M. (2006). *Principles of Animal Locomotion*. Princeton University Press.

Alexander, R.M.N. and A.S. Jayes (1983). "A dynamic similarity hypothesis for the gaits of quadrupedal mammals". In: *J Zool* 201, 135–152. DOI: 10.1111/j.1469-7998.1983.tb04266.x.

Altendorfer, R., N. Moore, H. Komsuoglu, M. Buehler, H.B. Brown, D. Mcmordie, U. Saranli, R. Full, and D.E. Koditschek (2001). "RHex: A biologically inspired hexapod runner". In: *Auton Robots* 11, 207–213. DOI: 10.1023/A:1012426720699.

Anderson, P.W. (1972). "More Is Different". In: *Science* 177, 393–396. DOI: 10.1126/science.177.4047.393.

Ashe, V.M. (1970). "The righting reflex in turtles: A description and comparison". In: *Psychon Sci* 20, 150–152. DOI: 10.3758/BF03335647.

Astley, H.C., Dai Mendelson JR, Gong J, Chong C, Rieser B, Schiebel JM, Sharpe PE, Hatton SS, Choset RL, Goldman H, and D.I. (2020). "Surprising simplicities and syntheses in limbless self-propulsion in sand". In: *J Exp Biol* 223. DOI: 10.1242/jeb.103564.

Aydin, Y.O., J.M. Rieser, C.M. Hubicki, W. Savoie, and D.I. Goldman (2019). "Physics approaches to natural locomotion: Every robot is an experiment". In: 109–127. DOI: 10.1016/B978-0-08-102260-3.00006-8.

Bailey, S.A. (2004). "Biomimetic control with a feedback coupled nonlinear oscillator: Insect experiments, design tools, and hexapedal robot application results". In:

Bartholomew, G.A. and H.H. Caswell (1951). "Locomotion in kangaroo rats and its adaptive significance". In: *J Mammal* 32.155. DOI: 10.2307/1375371.

Berman, G.J. (2018). "Measuring behavior across scales". In: *BMC Biol* 16.23. DOI: 10.1186/s12915-018-0494-7.

Berman, G.J., W. Bialek, and J.W. Shaevitz (2016). "Predictability and hierarchy in Drosophila behavior". In: *Proc Natl Acad Sci* 113, 11943–11948. DOI: 10.1073/pnas.1607601113.

Bermudez, P.L.G, R.C. Julian, D.W. Haldane, P. Abbeel, and R.S. Fearing (2012). "Performance analysis and terrain classification for a legged robot over rough terrain". In: *IEEE/RSJ Int Conf Intell Rob Sys*. IEEE, pp. 513–519.

Biewener, A.A. (2003). *Animal Locomotion*. Oxford University Press.

Biewener, A.A. and M.A. Daley (2007). "Unsteady locomotion: Integrating muscle function with whole body dynamics and neuromuscular control". In: *J Exp Biol* 210, 2949–2960. DOI: 10.1242/jeb.005801.

Birn-Jeffery, A.V., Hubicki CM, Blum Y, Renjewski D, Hurst JW, and Daley MA (2014). "Don't break a leg: Running birds from quail to ostrich prioritise leg safety and economy on uneven terrain". In: *J Exp Biol* 217, 3786–3796. DOI: 10.1242/jeb.102640.

Birn-Jeffery, A.V. and M.A. Daley (2012). "Birds achieve high robustness in uneven terrain through active control of landing conditions". In: *J. Exp. Biol* 215, 2117–2127.

Blaesing, B. (2004). "Stick insect locomotion in a complex environment: Climbing over large gaps". In: *J Exp Biol* 207, 1273–1286. DOI: 10.1242/jeb.00888.

Blickhan, R. and R.J. Full (1993). "Similarity in multilegged locomotion: Bouncing like a monopode". In: *J Comp Physiol A* 173, 509–517. DOI: 10.1007/BF00197760.

Bolmin, O., C. Duan, L. Urrutia, A.M. Abdulla, A.M. Hazel, M. Alleyne, A.C. Dunn, and A. Wissa (2017). "Pop! Observing and modeling the legless self-righting jumping mechanism of click beetles". In: 35–47. DOI: 10.1007/978-3-319-63537-8_4.

Bouman, Amanda, Muhammad Fadhil Ginting, Nikhilesh Alatur, Matteo Palieri, David D Fan, Thomas Touma, Torkom Pailevanian, Sung-Kyun Kim, Kyohei Otsu, Joel Burdick, et al. (2020). "Autonomous spot: Long-range autonomous exploration of extreme environments with legged locomotion". In: *2020 IEEE/RSJ Int Conf Intell Rob Sys*. IEEE, pp. 2518–2525.

Brackenbury, J. (1990). "A novel method of self-righting in the springtail Sminthurus viridis (Insecta: Collembola)". In: *J Zool* 222, 117–119. DOI: 10.1111/j.1469-7998.1990.tb04033.x.

Bramble, D.M. and D.E. Lieberman (2004). "Endurance running and the evolution of Homo". In: *Nature* 432, 345–352. DOI: 10.1038/nature03052.

Brost, R.C. (1992). "Dynamic analysis of planar manipulation tasks". In: *IEEE International Conference on Robotics and Automation*, 2247–2254. DOI: 10.1109/ROBOT.1992.219924.

Brown, A.E.X. and B. Bivort (2018). "Ethology as a physical science". In: *Nat Phys* 14, 653–657. DOI: 10.1038/s41567-018-0093-0.

Bryngelson, J.D. and P.G. Wolynes (1989). "Intermediates and barrier crossing in a random energy model (with applications to protein folding)". In: *J Phys Chem* 93, 6902–6915. DOI: 10.1021/j100356a007.

Buchner, H.H., H.H. Savelberg, H.C. Schamhardt, H.W. Merkens, and A. Barneveld (1994). "Kinematics of treadmill versus overground locomotion in horses". In: *Vet Q* 16 Suppl 2. DOI: 10.1080/01652176.1994.9694509.

Burridge, R.R., A.A. Rizzi, and D.E. Koditschek (1999). "Sequential composition of dynamically dexterous robot behaviors". In: *Int J Rob Res* 18, 534–555. DOI: 10.1177/02783649922066385.

Byl, K. and R. Tedrake (2009). "Metastable walking machines". In: *Int J Rob Res* 28, 1040–1064. DOI: 10.1177/0278364909340446.

Calhoun, A.J., J.W. Pillow, and M. Murthy (2019). "Unsupervised identification of the internal states that shape natural behavior". In: *Nat Neurosci* 22, 2040–2049. DOI: 10.1038/s41593-019-0533-x.

Camhi, J.M. (1977). "Behavioral switching in cockroaches: transformations of tactile reflexes during righting behavior". In: *J Comp Physiol* 113, 283–301. DOI: 10.1007/BF00620403.

Cande, J., S. Namiki, J. Qiu, W. Korff, G.M. Card, J.W. Shaevitz, D.L. Stern, and G.J. Berman (2018). "Optogenetic dissection of descending behavioral control in Drosophila". In: *eLife* 7, 1–23. DOI: 10.7554/eLife.34275.

Caporale, J.D., B.W. McInroe, C. Ning, T. Libby, R.J. Full, and D.E. Koditschek (2020). "Coronal plane spine twisting composes shape to adjust the energy

landscape for grounded reorientation". In: IEEE, 8052–8058. DOI: 10.1109/ICRA40945.2020.9197026.

Cavagna, G.A., H. Thys, and A. Zamboni (1976). "The sources of external work in level walking and running". In: *J Physiol* 262, 639–657.

Cayley, G. (1876). "On Aërial Navigation". In: *Annu Reports Aeronaut Soc Gt Britain* 11, 60–94. DOI: 10.1017/S2397930500000552.

Collett, M., L. Chittka, and T.S. Collett (2013). "Spatial memory in insect navigation". In: *Curr Biol* 23:R789–R800. DOI: 10.1016/j.cub.2013.07.020.

Collins, C.E., J.D. Self, R.A. Anderson, and L.D. McBrayer (2013). "Rock-dwelling lizards exhibit less sensitivity of sprint speed to increases in substrate rugosity". In: *Zoology* 116, 151–158. DOI: 10.1016/j.zool.2013.01.001.

Couzin-Fuchs, E., T. Kiemel, O. Gal, A. Ayali, and P. Holmes (2015). "Intersegmental coupling and recovery from perturbations in freely running cockroaches". In: *J Exp Biol* 218, 285–297. DOI: 10.1242/jeb.112805.

Cowan, N.J. and D.E. Koditschek (1999). "Planar image based visual servoing as a navigation problem". In: *Proceedings 1999 IEEE Int Conf Rob Autom.* Vol. 1. IEEE, pp. 611–617.

Cowan, N.J., J. Lee, and R.J. Full (2006). "Task-level control of rapid wall following in the American cockroach". In: *J Exp Biol* 209, 1617–1629. DOI: 10.1242/jeb.02433.

Cowan, N.J., G.A.D. Lopes, and D. E Koditschek (2000). "Rigid body visual servoing using navigation functions". In: *Proc 39th IEEE Conf Decision Control.* Vol. 4. IEEE, pp. 3920–3926.

Crall, J.D., N. Gravish, A.M. Mountcastle, and S.A. Combes (2015). "BEEtag: A low-cost, image-based tracking system for the study of animal behavior and locomotion". In: *PLoS One* 10, 1–13. DOI: 10.1371/journal.pone.0136487.

Creery, B.L. and B.H. Bland (1980). "Ontogeny of fascia dentata electrical activity and motor behavior in the dutch belted rabbit (Oryctolagus cuniculus)". In: *Exp Neurol* 67, 554–572. DOI: 10.1016/0014-4886(80)90126-0.

Daley, M.A. and A.A. Biewener (2006). "Running over rough terrain reveals limb control for intrinsic stability". In: *Proc Natl Acad Sci* 103, 15681–15686. DOI: 10.1073/pnas.0601473103.

Darken, R.P., W.R. Cockayne, and D. Carmein (1997). "Omni-directional treadmill: A locomotion device for virtual worlds". In: *UIST (User Interface Softw Technol Proc ACM Symp*, 213–221.

Davis, W.J. (1968). "Lobster righting responses and their neural control". In: *Proc R Soc B* 170, 435–456. DOI: 10.1098/rspb.1968.0049.

Delcomyn, F. (1987). "Motor activity during searching and walking movements of cockroach legs". In: *J Exp Biol* 133, 111–20.

Dickinson, M.H., C.T. Farley, R.J. Full, M.A.R. Koehl, R. Kram, and S. Lehman (2000). "How animals move: An integrative view". In: *Science* 288, 100–106. DOI: 10.1126/science.288.5463.100.

Dickinson, M.H., F.O. Lehmann, and S.P. Sane (1999). "Wing rotation and the aerodynamic basis of insect right". In: *Science* 284, 1954–1960. DOI: 10.1126/science.284.5422.1954.

Diederich, B., M. Schumm, and H. Cruse (2002). "Stick insects walking along inclined surfaces". In: *Integr Comp Biol* 42, 165–173. DOI: 10.1093/icb/42.1.165.

Diedrich, F.J. and W.H. Warren (1995). "Why change gaits? Dynamics of the walk-run transition". In: *J Exp Psychol Hum Percept Perform* 21, 183–202. DOI: 10.1037/0096-1523.21.1.183.

Dill, K.A. and H.S. Chan (1997). "From Levinthal to pathways to funnels: The "new view" of protein folding kinetics". In: *Nat Struct Biol* 4.10.

Dill, K.A. and J.L. MacCallum (2012). "The Protein-Folding Problem, 50 Years On". In: *Science* 338, 1042–1046. DOI: 10.1126/science.1219021.

Dill, K.A., S.B. Ozkan, M.S. Shell, and T.R. Weikl (2008). "The protein folding problem". In: *Annu Rev Biophys* 37, 289–316. DOI: 10.1146/annurev.biophys.37.092707.153558.

Ding, Y., S.S. Sharpe, K. Wiesenfeld, and D.I. Goldman (2013). "Emergence of the advancing neuromechanical phase in a resistive force dominated medium". In: *Proc Natl Acad Sci* 110, 10123–10128. DOI: 10.1073/pnas.1302844110.

Domokos, G. and P.L. Várkonyi (2008). "Geometry and self-righting of turtles". In: *Proc R Soc B* 275, 11–17. DOI: 10.1098/rspb.2007.1188.

Dunbabin, M. and L. Marques (2012). "Robotics for environmental monitoring: Significant advancements and applications". In: *IEEE Robot Autom Mag* 19, 24–39. DOI: 10.1109/MRA.2011.2181683.

Dürr, V. and M. Schilling (2018). "Transfer of spatial contact information among limbs and the notion of peripersonal space in insects". In: *Front Comput Neurosci* 12, 1–20. DOI: 10.3389/fncom.2018.00101.

Ellington, C.P., C. Van Den Berg, A.P. Willmott, and A.L.R. Thomas (1996). "Leading-edge vortices in insect flight". In: *Nature* 384.6610, pp. 626–630.

Faisal, A.A. and T. Matheson (2001). "Coordinated righting behaviour in locusts". In: *J Exp Biol* 204, 637–48.

Ferris, D.P., M. Louie, and C.T. Farley (1998). "Running in the real world: Adjusting leg stiffness for different surfaces". In: *Proc R Soc B* 265, 989–994. DOI: 10.1098/rspb.1998.0388.

Fodor, É. and M.C. Marchetti (2018). "The statistical physics of active matter: From self-catalytic colloids to living cells". In: *Physica A* 504, 106–120. DOI: 10.1016/j.physa.2017.12.137.

Forlizzi, J. and C. DiSalvo (2006). "Service robots in the domestic environment". In: *Proceeding of the 1st ACM SIGCHI/SIGART Conference on Human-Robot Interaction - HRI '06*. ACM Press, p. 258. DOI: 10.1145/1121241.1121286.

Frantsevich, L.I. and P.A. Mokrushov (1980). "Turning and righting in Geotrupes (Coleoptera, Scarabaeidae)". In: *J Comp Physiol A* 136, 279–289. DOI: 10.1007/BF00657348.

Fryxell, J.M., M. Hazell, L. Börger, B.D. Dalziel, D.T. Haydon, J.M. Morales, T. McIntosh, and R.C. Rosatte (2008). "Multiple movement modes by large herbivores at multiple spatiotemporal scales". In: *Proc Natl Acad Sci* 105, 19114–19119. DOI: 10.1073/pnas.0801737105.

Full, R., A. Yamauchi, and D. Jindrich (1995). "Maximum single leg force production: Cockroaches righting on photoelastic gelatin". In: *J Exp Biol* 198, 2441–2452. DOI: 10.1242/jeb.198.12.2441.

Full, R.J (1987). "Locomotion energetics of the ghost crab: I : Metabolic cost and endurance". In: *J Exp Biol* 153, 137–153.

Full, R.J. and D.E. Koditschek (1999). "Templates and anchors: neuromechanical hypotheses of legged locomotion on land". In: *J Exp Biol* 202, 3325–3332.

Full, R.J. and M.S. Tu (1990). "Mechanics of six-legged runners". In: *J Exp Bio* 148.1, pp. 129–146.

Garrido-Jurado, S., R. Muñoz-Salinas, F.J. Madrid-Cuevas, and M.J. Marín-Jiménez (2014). "Automatic generation and detection of highly reliable fiducial markers under occlusion". In: *Pattern Recognit* 47, 2280–2292. DOI: 10.1016/j.patcog.2014.01.005.

Gart, S.W. and C. Li (2018). "Body-terrain interaction affects large bump traversal of insects and legged robots". In: *Bioinspir Biomim* 13.026005. DOI: 10.1088/1748-3190/aaa2d0.

Gart, S.W., C. Yan, R. Othayoth, Z. Ren, and C. Li (2018). "Dynamic traversal of large gaps by insects and legged robots reveals a template". In: *Bioinspir Biomim* 13.026006. DOI: 10.1088/1748-3190/aaa2cd.

Gatesy, S.M., M. Bäker, and JR Hutchinson (2009). "Constraint-based exclusion of limb poses for reconstructing theropod dinosaur locomotion". In: *J Vertebr Paleontol* 29, 535–544. DOI: 10.1671/039.029.0213.

Geyer, H., A. Seyfarth, and R. Blickhan (2006). "Compliant leg behaviour explains basic dynamics of walking and running". In: *Proc R Soc B* 273, 2861–2867. DOI: 10.1098/rspb.2006.3637.

Gibson, J.J. (2014). *The theory of affordances:The ecological approach to visual perception*. Psychology Press, 41–64. DOI: 10.4324/9781315740218.

Gillette, R., R.-C. Huang, N. Hatcher, and L.L. Moroz (2000). "Cost-benefit analysis potential in feeding behavior of a predatory snail by integration of hunger, taste, and pain". In: *Proc Nat Acad Sci* 97.7, pp. 3585–3590.

Goldman, D.I. (2014). "Colloquium: Biophysical principles of undulatory self-propulsion in granular media". In: *Rev Mod Phys* 86, 943–958. DOI: 10.1103/RevModPhys.86.943.

Goldman, D.I., T.S. Chen, D.M. Dudek, and R.J. Full (2006). "Dynamics of rapid vertical climbing in cockroaches reveals a template". In: *J Exp Biol* 209, 2990–3000. DOI: 10.1242/jeb.02322.

Golubović, A., M. Anđelković, D. Arsovski, X. Bonnet, and L. Tomović (2017). "Locomotor performances reflect habitat constraints in an armoured species". In: *Behav Ecol Sociobiol* 71. DOI: 10.1007/s00265-017-2318-0.

Golubović, A., X. Bonnet, S. Djordjević, M. Djurakic, and L. Tomović (2013). "Variations in righting behaviour across Hermann's tortoise populations". In: *J Zool* 291, 69–75. DOI: 10.1111/jzo.12047.

Golubović A Tomović L, Ivanović A. (2015). "Geometry of self righting: The case of Hermann's tortoises". In: *Zool Anz* 254, 99–105. DOI: 10.1016/j.jcz.2014.12.003.

Gould, S. and E. Vrba (1982). "Exaptation—a missing term on the science of form". In: *Paleobiology*. DOI: 10.1017/S0094837300004310.

Gravish, N. and G.V. Lauder (2018). "Robotics-inspired biology". In: *Journal of Experimental Biology* 221.7, jeb138438.

Greer, J.D., L.H. Blumenschein, A.M. Okamura, and E.W. Hawkes (2018). "Obstacle-aided navigation of a soft growing robot". In: *IEEE Int Conf Rob Autom*. IEEE, pp. 4165–4172.

Guizzo, E. and E. Ackerman (2015). "The hard lessons of DARPA's robotics challenge". In: *IEEE Spectr* 52, 11–13. DOI: 10.1109/mspec.2015.7164385.

Hackett, J., W. Gao, M. Daley, J. Clark, and C. Hubicki (2020). "Risk-constrained motion planning for robot locomotion: Formulation and running robot demonstration". In: *International Conference on Intelligent Robots and Systems (IROS)*. IEEE, 3633–3640. DOI: 10.1109/IROS45743.2020.9340810.

Haldane, D.W., C.S. Casarez, J.T. Karras, J. Lee, C. Li, A.O. Pullin, E.W. Schaler, D. Yun, H. Ota, Ali J., and R.S Fearing (2015). "Integrated manufacture of exoskeletons and sensing structures for folded millirobots". In: *J. Mech. Robot.* 7.2, p. 021011.

Hammond, T.T., D. Springthorpe, R.E. Walsh, and T. Berg-Kirkpatrick (2016). "Using accelerometers to remotely and automatically characterize behavior in small animals". In: *J Exp Biol* 219, 1618–1624. DOI: 10.1242/jeb.136135.

Han, Y., R. Othayoth, Y. Wang, C.-C. Hsu, R. Tijera Obert, E. Francois, and C. Li (2021). "Shape-induced obstacle attraction and repulsion during dynamic locomotion". In: *Int J Rob Res* 40, 939–956. DOI: 10.1177/0278364921989372.

Harley, C.M., B.A. English, and R.E. Ritzmann (2009). "Characterization of obstacle negotiation behaviors in the cockroach, Blaberus discoidalis". In: *J Exp Biol* 212, 1463–1476. DOI: 10.1242/jeb.028381.

Harvey, A.C. (1990). *Forecasting, structural time series models and the Kalman filter*. Cambridge university press.

Hedrick, T.L. (2008). "Software techniques for two- and three-dimensional kinematic measurements of biological and biomimetic systems". In: *Bioinspir Biomim* 3.034001. DOI: 10.1088/1748-3182/3/3/034001.

Helbing, D. (2001). "Traffic and related self-driven many-particle systems". In: *Rev Mod Phys* 73, 1067–1141. DOI: 10.1103/RevModPhys.73.1067.

Herreid, C.F. and R.J. Full (1984). "Cockroaches on a treadmill: Aerobic running". In: *J Insect Physiol* 30, 395–403. DOI: 10.1016/0022-1910(84)90097-0.

Hoffman, D. (1980). "Defensive Responses of Marine Gastropods (Prosobranchia, Trochidae) to Certain Predatory Seastars and the Dire Whelk, Searlesia dira (Reeve)". In:

Holmes, P., R.J. Full, D.E. Koditschek, and J. Guckenheimer (2006). "The dynamics of legged locomotion: Models, analyses, and challenges". In: *SIAM Rev* 48, 207–304. DOI: 10.1137/S0036144504445133.

Hoyt, D.F. and C.R. Taylor (1981). "Gait and the energetics of locomotion in horses". In: *Nature* 292, 239–240. DOI: 10.1038/292239a0.

Hu, D.L., J. Nirody, T. Scott, and M.J. Shelley (2009). "The mechanics of slithering locomotion". In: *Proc Natl Acad Sci* 106, 10081–10085. DOI: 10.1073/pnas.0812533106.

Hu, W., G.Z. Lum, M. Mastrangeli, and M. Sitti (2018). "Small-scale soft-bodied robot with multimodal locomotion". In: *Nature* 554, 81–85. DOI: 10.1038/nature25443.

Hwangbo, J., J. Lee, A. Dosovitskiy, D. Bellicoso, V. Tsounis, V. Koltun, and M. Hutter (2019). "Learning agile and dynamic motor skills for legged robots". In: *Sci Rob* 4.26.

Ijspeert, A.J. (2008). "Central pattern generators for locomotion control in animals and robots: A review". In: *Neural Networks* 21, 642–653. DOI: 10.1016/j.neunet.2008.03.014.

Ijspeert, A.J. (2014). "Biorobotics: using robots to emulate and investigate agile locomotion". In: *Science* 346, 196–203. DOI: 10.1126/science.1254486.

Jayakumar, R.P., M.S. Madhav, F. Savelli, H.T. Blair, N.J. Cowan, and J.J. Knierim (2019). "Recalibration of path integration in hippocampal place cells". In: *Nature* 566, 533–537. DOI: 10.1038/s41586-019-0939-3.

Kaspari, M., Weiser MD, Kaspari M, and Weiser MDM (1999). "The size-grain hypothesis and interspecific scaling in ants". In: *Funct Ecol* 13, 530–538. DOI: 10.1046/j.1365-2435.1999.00343.x.

Kelso, J.A.S. (2012). "Multistability and metastability: Understanding dynamic coordination in the brain". In: *Philos Trans R Soc B* 367, 906–918. DOI: 10.1098/rstb.2011.0351.

Kenneally, G., A. De, and D.E. Koditschek (2016). "Design principles for a family of direct-drive legged robots". In: *IEEE Rob Autom Lett* 1.2, pp. 900–907.

Kennedy, A., K. Asahina, E. Hoopfer, H. Inagaki, Y. Jung, H. Lee, R. Remedios, and D.J. Anderson (2014). "Internal states and behavioral decision-making: Toward an integration of emotion and cognition". In: *Cold Spring Harb Symp Quant Biol* 79, 199–210. DOI: 10.1101/sqb.2014.79.024984.

Kessens, C.C., D.C. Smith, and P.R. Osteen (2012). "A framework for autonomous self-righting of a generic robot on sloped planar surfaces". In: *Proc - IEEE Int Conf Robot Autom*, 4724–4729. DOI: 10.1109/ICRA.2012.6224770.

Khatib, O. (1986). "Real-time obstacle avoidance for manipulators and mobile robots". In: *Auton Robot Veh*, 396–404. DOI: 10.1007/978-1-4613-8997-2_29.

Kleitman, N. and T. Koppanyi (1926). "Body-righting in the fowl (Gallus domesticus)". In: *Am J Physiol Content* 78, 110–126. DOI: 10.1152/ajplegacy.1926.78.1.110.

Koditschek, D.E. (2021). "What Is Robotics? Why do we need it and how can we get it?" In: *Annu Rev Control Robot Auton Syst* 4, 1–33. DOI: 10.1146/annurev-control-080320-011601.

Koditschek, D.E., R.J. Full, and M. Buehler (2004). "Mechanical aspects of legged locomotion control". In: *Arthropod Struct Dev* 33, 251–272. DOI: 10.1016/j.asd.2004.06.003.

Koehl, M.A.R (2003). "Physical modelling in biomechanics". In: *Phil Trans Roy Soc London B: Biol Sci* 358.1437, pp. 1589–1596.

Kohlsdorf, T. and A.A. Biewener (2006). "Negotiating obstacles: Running kinematics of the lizard Sceloporus malachiticus". In: *J Zool* 270, 359–371. DOI: 10.1111/j.1469-7998.2006.00150.x.

Koppányi, T. and N. Kleitman (1927). "Body righting and related phenomena in the domestic duck (Anas boscas)". In: *Am J Physiol Content* 82, 672–685. DOI: 10.1152/ajplegacy.1927.82.3.672.

Kovac, M., M. Fuchs, A. Guignard, J.-C. Zufferey, and D. Floreano (2008). "A miniature 7g jumping robot". In: *Int Conf Rob Autom*, 373–378. DOI: 10.1109/ROBOT.2008.4543236.

Kram, R., T.M. Griffin, J.M. Donelan, and Y.H. Chang (1998). "Force treadmill for measuring vertical and horizontal ground reaction forces". In: *J Appl Physiol* 85, 764–769. DOI: 10.1152/jappl.1998.85.2.764.

Kram, R., B. Wong, and R.J. Full (1997). "Three-dimensional kinematics and limb kinetic energy of running cockroaches". In: *J Exp Biol* 200, 1919–29. DOI: 10.1242/jeb.200.13.1919.

Krishnasamy, J. (1996). "Mechanics of entrapment with application to design of industrial parts feeders". PhD thesis. Massachusetts Institute of Technology.

Kuo, A.D. (2007). "The six determinants of gait and the inverted pendulum analogy: A dynamic walking perspective". In: *Hum Mov Sci* 26, 617–656. DOI: 10.1016/j.humov.2007.04.003.

Larcombe, MHE (1979). "Mobile robots for industrial use". In: *Industrial Robot: An International Journal*.

Latombe, J.-C. (2012). *Robot Motion Planning*. Springer Science & Business Media.

Latty, T. and M. Beekman (2010). "Food quality and the risk of light exposure affect patch-choice decisions in the slime mold Physarum polycephalum". In: *Ecology* 91.1, pp. 22–27.

Lauder, G.V. and E.G. Drucker (2002). "Forces, fishes, and fluids: Hydrodynamic mechanisms of aquatic locomotion". In: *News Physiol. Sci* 17, 235–240.

Lauder, G.V., B. Flammang, and S. Alben (2012). "Passive robotic models of propulsion by the bodies and caudal fins of fish". In:

Lee, J., J. Hwangbo, L. Wellhausen, V. Koltun, and M. Hutter (2020). "Learning quadrupedal locomotion over challenging terrain". In: *Sci Rob* 5.47.

Lepetit, V., F. Moreno-Noguer, and P. Fua (2009). "EPnP: An accurate O(n) solution to the PnP problem". In: *Int J Comput Vis* 81, 155–166. DOI: 10.1007/s11263-008-0152-6.

Li, C., S.T. Hsieh, and D.I. Goldman (2012). "Multi-functional foot use during running in the zebra-tailed lizard (Callisaurus draconoides)". In: *J Exp Biol* 215, 3293–3308. DOI: 10.1242/jeb.061937.

Li, C., C.C. Kessens, R.S. Fearing, and R.J. Full (2017). "Mechanical principles of dynamic terrestrial self-righting using wings". In: *Adv Robot* 31, 881–900. DOI: 10.1080/01691864.2017.1372213.

Li, C., C.C. Kessens, A. Young, R.S. Fearing, and R.J. Full (2016). "Cockroach-inspired winged robot reveals principles of ground-based dynamic self-righting". In: *Int Conf Intell Rob Sys*, 2128–2134. DOI: 10.1109/IROS.2016.7759334.

Li, C., A.O. Pullin, D.W. Haldane, H.K. Lam, R.S. Fearing, and R.J. Full (2015). "Terradynamically streamlined shapes in animals and robots enhance traversability through densely cluttered terrain". In: *Bioinspir Biomim* 10.46003. DOI: 10.1088/1748-3190/10/4/046003.

Li, C., P.B. Umbanhowar, H. Komsuoglu, and D.I. Goldman (2010). "The effect of limb kinematics on the speed of a legged robot on granular media". In: *Proc Soc Exp Mech*, 1383–1393. DOI: 10.1007/S11340-010-9347-1.

Li, C., P.B. Umbanhowar, H. Komsuoglu, D.E. Koditschek, and D.I. Goldman (2009). "Sensitive dependence of the motion of a legged robot on granular media". In: *Proc Natl Acad Sci* 106, 3029–3034. DOI: 10.1073/pnas.0809095106.

Li, C., T. Wöhrl, H.K. Lam, and R.J. Full (2019). "Cockroaches use diverse strategies to self-right on the ground". In: *J Exp Biol* 222:jeb186080. DOI: 10.1242/jeb.186080.

Li, C., T. Zhang, and D.I. Goldman (2013). "A terradynamics of legged locomotion on granular media". In: *Science* 339, 1408–1412. DOI: 10.1126/science.1229163.

Li, L. (2000). "Stability landscapes of walking and running near gait transition speed". In: *J Appl Biomech* 16, 428–435. DOI: 10.1123/jab.16.4.428.

Liljeback, P., K.Y. Pettersen, Ø. Stavdahl, and J.T. Gravdahl (2011). "Experimental investigation of obstacle-aided locomotion with a snake robot". In: *IEEE Trans Rob* 27.4, pp. 792–800.

Lindhe Norberg, U.M. (2002). "Structure, form, and function of flight in engineering and the living world". In: *J Morph* 252.1, pp. 52–81.

Lock, R.J., S.C. Burgess, and R. Vaidyanathan (2013). "Multi-modal locomotion: from animal to application". In: *Bioinspir Biomim* 9.011001. DOI: 10.1088/1748-3182/9/1/011001.

Long, J. (2012). *Darwin's devices: what evolving robots can teach us about the history of life and the future of technology*. Basic Books (AZ).

Low, K.H., T. Hu, S. Mohammed, J. Tangorra, and M. Kovac (2015). "Perspectives on biologically inspired hybrid and multi-modal locomotion". In: *Bioinspir Biomim* 10.020301. DOI: 10.1088/1748-3190/10/2/020301.

Maladen, R.D., P.B. Umbanhowar, Y. Ding, A. Masse, and D.I. Goldman (2011). "Granular lift forces predict vertical motion of a sand-swimming robot". In: *Proc - IEEE Int Conf Robot Autom 1398–1403*. DOI: 10.1109/ICRA.2011.5980301.

Malashichev, Y. (2016). "Asymmetry of righting reflexes in sea turtles and its behavioral correlates". In: *Physiol Behav* 157, 1–8. DOI: 10.1016/j.physbeh.2016.01.001.

Marvi, H., C. Gong, N. Gravish, H. Astley, M. Travers, R.L. Hatton, Choset Mendelson JR, Hu H, Goldman DL, and D.I. (2014). "Sidewinding with minimal slip: Snake and robot ascent of sandy slopes". In: *Science* 346, 224–229. DOI: 10.1126/science.1255718.

McFarland, D.J. (1977). "Decision making in animals". In: *Nature* 269.5623, pp. 15–21.

McInroe, B., H.C. Astley, C. Gong, S.M. Kawano, P.E. Schiebel, J.M. Rieser, H. Choset, R.W. Blob, and D.I. Goldman (2016). "Tail use improves performance on soft substrates in models of early vertebrate land locomotors". In: *Science* 353, 154–158. DOI: 10.1126/science.aaf0984.

Mearns, D.S., J.C. Donovan, A.M. Fernandes, J.L. Semmelhack, and H. Baier (2020). "Deconstructing hunting behavior reveals a tightly coupled stimulus-response loop". In: *Curr Biol* 30, 54–69. DOI: 10.1016/j.cub.2019.11.022.

Minetti, A.E., C. Moia, G.S. Roi, D. Susta, and G. Ferretti (2002). "Energy cost of walking and running at extreme uphill and downhill slopes". In: *J Appl Physiol* 93, 1039–1046. DOI: 10.1152/japplphysiol.01177.2001.

Mohri, N and N Saito (1994). "Some effects of ultrasonic vibration on the inserting operation". In: *Int J Adv Manu Tech* 9.4, pp. 225–230.

Mongeau, J., L.E. Schweikert, A.L. Davis, M.S. Reichert, and J.K. Kanwal (2021). "Multimodal integration across spatiotemporal scales to guide invertebrate locomotion". In: *Integr Comp Biol*. DOI: 10.1093/icb/icab041.

Mongeau, J.-M., A. Demir, C.J. Dallmann, K. Jayaram, N.J. Cowan, and R.J. Full (2014). "Mechanical processing via passive dynamic properties of the cockroach antenna can facilitate control during rapid running". In: *J Exp Biol* 3333–3345. DOI: 10.1242/jeb.101501.

Mongeau, J.-M., S.N. Sponberg, J.P. Miller, and R.J. Full (2015). "Sensory processing within cockroach antenna enables rapid implementation of feedback control for high-speed running maneuvers". In: *J Exp Biol* 218, 2344–54. DOI: 10.1242/jeb.118604.

Moritz, C.T. and C.T. Farley (2003). "Human hopping on damped surfaces: Strategies for adjusting leg mechanics". In: *Proc R Soc B* 270, 1741–1746. DOI: 10.1098/rspb.2003.2435.

Murphy, R.R., S. Tadokoro, D. Nardi, A. Jacoff, P. Fiorini, H. Choset, and A.M. Erkmen (2008). *Search and Rescue Robotics*. Springer Handb Robot.

Nakanishi, J., T. Fukuda, and D. E. Koditschek (2000). "A brachiating robot controller". In: *IEEE Trans Rob Autom* 16.2, pp. 109–123.

Nathan, R., W.M. Getz, E. Revilla, M. Holyoak, R. Kadmon, D. Saltz, and P.E. Smouse (2008). "A movement ecology paradigm for unifying organismal movement research". In: *Proc Natl Acad Sci* 105, 19052–19059. DOI: 10.1073/pnas.0800375105.

Nishikawa, K., A.A. Biewener, P. Aerts, A.N. Ahn, H.J. Chiel, M.A. Daley, T.L. Daniel, R.J. Full, M.E. Hale, T.L. Hedrick, A.K. Lappin, T.R. Nichols, R.D. Quinn, R.A. Satterlie, and B. Szymik (2007). "Neuromechanics: An integrative approach for understanding motor control". In: *Integr Comp Biol* 47, 16–54. DOI: 10.1093/icb/icm024.

Okada, J. and Y. Toh (2000). "The role of antennal hair plates in object-guided tactile orientation of the cockroach (Periplaneta americana)". In: *J Comp Physiol - A Sensory, Neural, Behav Physiol* 186, 849–857. DOI: 10.1007/s003590000137.

Okada, J. and Y. Toh (2006). "Active tactile sensing for localization of objects by the cockroach antenna". In: *J Comp Physiol A Neuroethol Sensory, Neural, Behav Physiol* 192, 715–726. DOI: 10.1007/s00359-006-0106-9.

Olberding, J.P., L.D. McBrayer, and T.E. Higham (2012). "Performance and three-dimensional kinematics of Bipedal lizards during Obstacle negotiation". In: *J Exp Biol* 215, 247–255. DOI: 10.1242/jeb.061135.

Onuchic, J.N., Z. Luthey-Schulten, and P.G. Wolynes (1997). "Theory of protein folding: the energy landscape perspective". In: *Ann Rev Phys Chem* 48.1, pp. 545–600.

Onuchic, J.N. and P.G. Wolynes (2004). "Theory of protein folding". In: *Curr Opin Struct Biol* 14, 70–75. DOI: 10.1016/j.sbi.2004.01.009.

Othayoth, R. and C. Li (2021). "Propelling and perturbing appendages together facilitate strenuous ground self-righting". In: *eLife* 10. DOI: 10.7554/eLife.60233.

Othayoth, R., B. Strebel, Y. Han, E. Francois, and C. Li (2021a). "A terrain treadmill to study small animal locomotion through large obstacles". In: *bioRxiv*. DOI: 10.1101/2021.08.31.458392.

Othayoth, R., G. Thoms, and C. Li (2020). "An energy landscape approach to locomotor transitions in complex 3D terrain". In: *Proc Natl Acad Sci* 117, 14987–14995. DOI: 10.1073/pnas.1918297117.

Othayoth, R., Q. Xuan, Y. Wang, and C. Li (2021b). "Locomotor transitions in the potential energy landscape-dominated regime". In: *Proc R Soc B*. DOI: 10.1098/rspb.2020.2734.

O'Donnel, D. (2018). *Mechanics of righting behavior in the tarantula (Theraphosidae)*. Wake Forest University.

Padilla, D.K., T.L. Daniel, P.S. Dickinson, D. Grünbaum, C. Hayashi, D.T. Manahan, J.H. Marden, B.J. Swalla, and B. Tsukimura (2014). "Addressing grand challenges in organismal biology: The need For synthesis". In: *Bioscience* 64, 1178–1187. DOI: 10.1093/biosci/biu164.

Park, H.W., P.M. Wensing, and S. Kim (2015). "Online planning for autonomous running jumps over obstacles in high-speed quadrupeds". In: *Robot Sci Syst* 11. DOI: 10.15607/RSS.2015.XI.047.

Parker, S.E. and L.D. McBrayer (2016). "The effects of multiple obstacles on the locomotor behavior and performance of a terrestrial lizard". In: *J Exp Biol* 219, 1004–1013. DOI: 10.1242/jeb.120451.

Pellis, V.C., S.M. Pellis, and P. Teitelbaum (1991). "A descriptive analysis of the postnatal development of contact-righting in rats (Rattus norvegicus)". In: *Dev Psychobiol* 24, 237–263. DOI: 10.1002/dev.420240405.

Penn, D. and H.J. Brockmann (1995). "Age-biased stranding and righting in male horseshoe crabs, Limulus polyphemus". In: *Anim Behav* 49, 1531–1539. DOI: 10.1016/0003-3472(95)90074-8.

Peshkin, M.A. and A.C. Sanderson (1988). "Planning robotic manipulation strategies for workpieces that slide". In: *IEEE J Robot Autom* 4, 524–531. DOI: 10.1109/56.20437.

Qian, F. and D.E. Koditschek (2020). "An obstacle disturbance selection framework: emergent robot steady states under repeated collisions". In: *Int J Rob Res* 39.13, pp. 1549–1566.

Quigley, M., K. Conley, B. Gerkey, J. Faust, T. Foote, J. Leibs, E. Berger, R. Wheeler, and A. Mg (2009). "ROS: an open-source Robot Operating System". In: p. 5. DOI: doi:http://www.willowgarage.com/papers/ros-open-source-robot-operating-system.

Raibert, M. (1986). *Legged Robots That Balance*. MIT Press.

Raibert, M. (2008). "BigDog, the rough-terrain quadruped robot". In: *IFAC Proceedings*. DOI: 10.3182/20080706-5-KR-1001.4278.

Ramaswamy, S. (2010). "The Mechanics and Statistics of Active Matter". In: *Annu Rev Condens Matter Phys* 1, 323–345. DOI: 10.1146/annurev-conmatphys-070909-104101.

Revzen, S., S.A. Burden, T.Y. Moore, J.M. Mongeau, and R.J. Full (2013). "Instantaneous kinematic phase reflects neuromechanical response to lateral perturbations of running cockroaches". In: *Biol Cybern* 107, 179–200. DOI: 10.1007/s00422-012-0545-z.

Rimon, E. and D.E. Koditschek (1992). "Exact Robot Navigation Using Artificial Potential Functions". In: *IEEE Trans Robot Autom* 8.5.

Ritzmann, R.E., C.M. Harley, K.A. Daltorio, B.R. Tietz, A.J. Pollack, J.A. Bender, P. Guo, A.L. Horomanski, N.D. Kathman, C. Nieuwoudt, A.E. Brown, and R.D. Quinn (2012). "Deciding which way to go: How do insects alter movements to negotiate barriers?" In: *Front Neurosci* 6, 1–10. DOI: 10.3389/fnins.2012.00097.

Roberts, S.F., D.E. Koditschek, and L.J. Miracchi (2020). "Examples of Gibsonian affordances in legged robotics research using an empirical, generative framework". In: *Front Neurorobot* 14, 1–9. DOI: 10.3389/fnbot.2020.00012.

Robins, A., G. Lippolis, A. Bisazza, G. Vallortigara, and L.J. Rogers (1998). "Lateralized agonistic responses and hindlimb use in toads". In: 56, 875–881. DOI: 10.1006/anbe.1998.0877.

Roth, E., R.W. Hall, T.L. Daniel, and S. Sponberg (2016). "Integration of parallel mechanosensory and visual pathways resolved through sensory conflict". In: *Proc Natl Acad Sci* 113, 12832–12837. DOI: 10.1073/pnas.1522419113.

Saranli, U., M. Buehler, and D.E. Koditschek (2001). "RHex: A simple and highly mobile hexapod robot". In: *Int J Rob Res* 20.7, pp. 616–631.

Sasaki, M. and T. Nonaka (2016). "The Reciprocity of Environment and Action in Self-Righting Beetles: The Textures of the Ground and an Object, and

the Claws". In: *Ecol Psychol* 28, 78–107. DOI: 10.1080/10407413.2016.1163983.

Savoie, W., T.A. Berrueta, Z. Jackson, A. Pervan, R. Warkentin, S. Li, T.D. Murphey, K. Wiesenfeld, and D.I. Goldman (2019). "A robot made of robots: Emergent transport and control of a smarticle ensemble". In: *Sci Robot* 4:eaax4316. DOI: 10.1126/scirobotics.aax4316.

Selvaggio, M, L.A. Ramirez, N.D. Naclerio, B. Siciliano, and E.W. Hawkes (2020). "An obstacle-interaction planning method for navigation of actuated vine robots". In: *IEEE Int Conf Rob Autom*. IEEE, pp. 3227–3233.

Sharpe, S.S., Y. Ding, and D.I. Goldman (2013). "Environmental interaction influences muscle activation strategy during sand-swimming in the sandfish lizard Scincus scincus". In: *J Exp Biol* 216, 260–274. DOI: 10.1242/jeb.070482.

Sharpe, S.S., S.A. Koehler, R.M. Kuckuk, M. Serrano, P.A. Vela, J. Mendelson, and D.I. Goldman (2015). "Locomotor benefits of being a slender and slick sand swimmer". In: *J Exp Biol* 218, 440–450. DOI: 10.1242/jeb.108357.

Shepard, E.L.C., R.P. Wilson, W.G. Rees, E. Grundy, S.A. Lambertucci, and S.B. Vosper (2013). "Energy landscapes shape animal movement ecology". In: *Am Nat* 182, 298–312. DOI: 10.1086/671257.

Sherman, E., M. Novotny, and J.M. Camhi (1977). "A modified walking rhythm employed during righting behavior in the cockroach Gromphadorhina portentosa". In: *J Comp Physiol A* 113, 303–316. DOI: 10.1007/BF00620404.

Shrivastava, S., A. Karsai, Y.O. Aydin, R. Pettinger, W. Bluethmann, R.O. Ambrose, and D.I. Goldman (2020). "Material remodeling and unconventional gaits facilitate locomotion of a robophysical rover over granular terrain". In: *Sci Robot* 5:eaba3499. DOI: 10.1126/scirobotics.aba3499.

Silvey, G.E. (1973). "Motor control of tail spine rotation of the horseshoe crab, Limulus polyphemus". In: *J Exp Biol* 58, 599–625.

Snijders, A.H., V. Weerdesteyn, Y.J. Hagen, J. Duysens, N. Giladi, and B.R. Bloem (2010). "Obstacle avoidance to elicit freezing of gait during treadmill walking". In: *Mov Disord* 25, 57–63. DOI: 10.1002/mds.22894.

Socci, N.D., J.N. Onuchic, and P.G. Wolynes (1996). "Diffusive dynamics of the reaction coordinate for protein folding funnels". In: *J Chem Phys* 104, 5860–5868. DOI: 10.1063/1.471317.

Spagna, J.C., D.I. Goldman, P.-C. Lin, D.E. Koditschek, and R.J. Full (2007). "Distributed mechanical feedback in arthropods and robots simplifies control of rapid running on challenging terrain". In: *Bioinspir Biomim* 2, 9–18. DOI: 10.1088/1748-3182/2/1/002.

Spence, A.J., S. Revzen, J. Seipel, C. Mullens, and R.J. Full (2010). "Insects running on elastic surfaces". In: *J Exp Biol* 213, 1907–1920. DOI: 10.1242/jeb.042515.

Sponberg, S. and R.J. Full (2008). "Neuromechanical response of musculoskeletal structures in cockroaches during rapid running on rough terrain". In: *J Exp Biol* 211, 433–446. DOI: 10.1242/jeb.012385.

Spong, M.W. (1995). "The swing up control problem for the acrobot". In: *IEEE control systems magazine* 15.1, pp. 49–55.

Stephens, G.J., B. Johnson-Kerner, W. Bialek, and W.S. Ryu (2008). "Dimensionality and dynamics in the behavior of C. elegans". In: *PLoS Comput Biol*. DOI: 10.1371/journal.pcbi.1000028.

Stephens, G.J., M. Mesquita, W.S. Ryu, and W. Bialek (2011). "Emergence of long timescales and stereotyped behaviors in Caenorhabditis elegans". In: *Proc Natl Acad Sci* 108, 7286–7289. DOI: 10.1073/pnas.1007868108.

Steyermark, A.C. and JR Spotila (2001). "Body Temperature and Maternal Identity Affect Snapping Turtle (Chelydra serpentina)". In: *Righting Response. Copeia* 2001, 1050–1057. DOI: 10.1643/0045-8511(2001)001.

Stolze, H., J.P. Kuhtz-Buschbeck, C. Mondwurf, A. Boczek-Funcke, K. Jöhnk, G. Deuschl, and M. Illert (1997). "Gait analysis during treadmill and overground locomotion in children and adults". In: *Electroencephalogr Clin Neurophysiol - Electromyogr Mot Control* 105, 490–497. DOI: 10.1016/S0924-980X(97)00055-6.

Suraci, J.P., M. Clinchy, L.Y. Zanette, and C.C. Wilmers (2019). "Fear of humans as apex predators has landscape-scale impacts from mountain lions to mice". In: *Ecol Lett* 22, 1578–1586. DOI: 10.1111/ele.13344.

Swanson, P.J., R.R. Burridge, and D.E. Koditschek (1995). "Global asymptotic stability of a passive juggler: A parts feeding strategy". In: *Proc IEEE Int Conf on Rob Autom*. Vol. 2. IEEE, pp. 1983–1988.

Taylor, C.R. and N.C. Heglund (1982). "Energetics and Mechanics of Terrestrial Locomotion". In: *Annu Rev Physiol* 44, 97–107. DOI: 10.1146/annurev.ph.44.030182.000525.

Teoh, Z.E. and R.J. Wood (2013). "A flapping-wing microrobot with a differential angle-of-attack mechanism". In: *Proc. - IEEE Int. Conf. Robot. Autom*, 1381–1388.

Theunissen, L.M., S. Vikram, and V. Dürr (2014). "Spatial coordination of foot contacts in unrestrained climbing insects". In: *J Exp Biol* 217, 3242–53. DOI: 10.1242/jeb.108167.

Thrun, S. (2010). "Toward robotic cars". In: *Commun ACM* 53.99. DOI: 10.1145/1721654.1721679.

Tinbergen, N. (1955). *Study of Instinct*. Clarendon Press.

Titus, T.N., J.J. Wynne, M.J. Malaska, A. Agha-Mohammadi, P.B. Buhler, E.C. Alexander, J.W. Ashley, A. Azua-Bustos, P.J. Boston, D.L. Buczkowski, L. Chiao, G.E. Cushing, J. DeDecker, P. León, C. Demirel-Floyd, J. De Waele, A.G. Fairén, A. Frumkin, G.L. Harris, H. Jones, L.H. Kerber, E.J. Leonard, R.J. Léveillé, K. Manyapu, M. Massironi, A.Z. Miller, J.E. Mylroie, B.P. Onac, S. Parazynski, C.B. Phillips, C.M. Phillips-Lander, T.H. Prettyman, H.M. Sapers, F. Sauro, N. Schorghofer, D. Schulze-Makuch, J.E. Scully, K. Uckert, Wagner R. V., W.L. Whittaker, K.E. Williams, and U.Y. Wong (2021). "A roadmap for planetary caves science and exploration". In: *Nat Astron* 5, 524–525. DOI: 10.1038/s41550-021-01385-1.

Transeth, A.A., R.I. Leine, C. Glocker, K.Y. Pettersen, and P. Liljebäck (2008). "Snake robot obstacle-aided locomotion: Modeling, simulations, and experiments". In: *IEEE Trans Rob* 24.1, pp. 88–104.

Tucker, D.B. and L.D. Mcbrayer (2012). "Overcoming obstacles: The effect of obstacles on locomotor performance and behaviour". In: *Biol J Linn Soc* 107, 813–823. DOI: 10.1111/j.1095-8312.2012.01993.x.

Tuthill, J.C. and E. Azim (2018). "Proprioception". In: *Curr Biol* 28:R194–R203. DOI: 10.1016/j.cub.2018.01.064.

Tuthill, J.C. and R.I. Wilson (2016). "Mechanosensation and adaptive motor control in insects". In: *Curr Biol* 26:R1022–R1038. DOI: 10.1016/j.cub.2016.06.070.

Varga, A.G., N.D. Kathman, J.P. Martin, P. Guo, and R.E. Ritzmann (2017). "Spatial navigation and the central complex: Sensory acquisition, orientation, and motor control". In: *Front Behav Neurosci* 11. DOI: 10.3389/fnbeh.2017.00004.

Vince, M.A. (1986). "Response of the newly born clun forest lamb to maternal vocalisations". In: *Behaviour* 96, 164–170. DOI: 10.1163/156853986X00261.

Viswanathan, G.M., M.G.E. Da Luz, E.P. Raposo, and H.E. Stanley (2011). *The Physics of Foraging*. Cambridge University Press.

Voelz, V.A., M. Jäger, S. Yao, Y. Chen, L. Zhu, S.A. Waldauer, G.R. Bowman, M. Friedrichs, O. Bakajin, L.J. Lapidus, S. Weiss, and V.S. Pande (2012). "Slow unfolded-state structuring in acyl-CoA binding protein folding revealed by simulation and experiment". In: *J Am Chem Soc* 134, 12565–12577. DOI: 10.1021/ja302528z.

Voloshina, A.S., A.D. Kuo, Daley M. a, and D.P. Ferris (2013). "Biomechanics and energetics of walking on uneven terrain". In: *J Exp Biol* 216, 3963–3970. DOI: 10.1242/jeb.081711.

Wales, D.J. (2003). *Energy Landscapes: Applications to clusters, biomolecules and glasses*. Cambridge University Press.

Wang, Y., R. Othayoth, and C. Li (2021). "Cockroaches adjust body and appendages to traverse cluttered large obstacles". In: *bioRxiv*. DOI: 10.1101/2021.10.02.462900.

Watson, J.T. and R.E. Ritzmann (1997). "Leg kinematics and muscle activity during treadmill running in the cockroach, Blaberus discoidalis: I Slow running." In: *J Comp Physiol - A Sensory, Neural, Behav Physiol* 182, 11–22. DOI: 10.1007/s003590050153.

Watson, J.T., R.E. Ritzmann, and A.J. Pollack (2002). "Control of climbing behavior in the cockroach, Blaberus discoidalis II. Motor activities associated with joint movement." In: *J Comp Physiol A Neuroethol Sensory, Neural, Behav Physiol* 188, 55–69. DOI: 10.1007/s00359-002-0278-x.

Weinstein, R.B. and R.J. Full (1999). "Intermittent locomotion increases endurance in a gecko". In: *Physiol Biochem Zool* 72, 732–739. DOI: 10.1086/316710.

Weldon, P.J. and D.L. Hoffman (1979). "Kick and thrust foot movements in the righting and escape behavior of marine prosobranch gastropods (Mollusca: Gastropoda)". In: *Z Tierpsychol* 50, 387–398. DOI: 10.1111/j.1439-0310.1979.tb01039.x.

Wiltschko, A.B., M.J. Johnson, G. Iurilli, R.E. Peterson, J.M. Katon, S.L. Pashkovski, V.E. Abraira, R.P. Adams, and SR Datta (2015). "Mapping sub-second structure in mouse behavior". In: *Neuron* 88, 1121–1135. DOI: 10.1016/j.neuron.2015.11.031.

Winter, A.G., R.L.H. Deits, D.S. Dorsch, A.H. Slocum, and A.E. Hosoi (2014). "Razor clam to RoboClam: Burrowing drag reduction mechanisms and their robotic adaptation". In: *Bioinspiration and Biomimetics* 9. DOI: 10.1088/1748-3182/9/3/036009.

Winters, W.D., A.J. Hance, G.C. Cadd, and M.L. Lakin (1986). "Seasonal and sex influences on ketamine-induced analgesia and catalepsy in the rat; a possible role for melatonin". In: *Neuropharmacology* 25, 1095–1101. DOI: 10.1016/0028-3908(86)90156-5.

Wu, X.A., T.M. Huh, R Mukherjee, and M Cutkosky (2016). "Integrated ground reaction force sensing and terrain classification for small legged robots". In: *IEEE Rob Autom Letters* 1.2, pp. 1125–1132.

Xuan, Q. and C. Li (2020a). "Coordinated appendages accumulate more energy to self-right on the ground". In: *IEEE Robot Autom Lett* 5, 6137–6144. DOI: 10.1109/LRA.2020.3011389.

Xuan, Q. and C. Li (2020b). "Randomness in appendage coordination facilitates strenuous ground self-righting". In: *Bioinspir Biomim* 21, 1–9. DOI: 10.1088/1748-3190/abac47.

Yang, G.Z., J. Bellingham, P.E. Dupont, P. Fischer, L. Floridi, R. Full, N. Jacobstein, V. Kumar, M. McNutt, R. Merrifield, B.J. Nelson, B. Scassellati, M. Taddeo, R. Taylor, M. Veloso, Z.L. Wang, and R. Wood (2018). "The grand challenges of science robotics". In: *Sci Robot* 3. DOI: 10.1126/scirobotics.aar7650.

Ye, S., J.P. Dowd, and C.M. Comer (1995). "A motion tracking system for simultaneous recording of rapid locomotion and neural activity from an insect". In: *J Neurosci Methods* 60, 199–210. DOI: 10.1016/0165-0270(95)00013-K.

Zhang, Y., S. Li, P. Zuo, J. Li, and J. Liu (2020). "A mechanics study on the self-righting of abalone from the substrate". In: *Appl Bionics Biomech.* DOI: 10.1155/2020/8825451.

Zhu, J., C. White, D.K. Wainwright, V. Di Santo, G.V. Lauder, and H. Bart-Smith (2019). "Tuna robotics: A high-frequency experimental platform exploring the performance space of swimming fishes". In: *Sci. Robot* 4.

Zill, S.N. (1986). "A model of pattern generation of cockroach walking reconsidered". In: *J Neurobiol* 17, 317–328. DOI: 10.1002/neu.480170406.

Zumel, N.B. (1997). "A nonprehensile method for reliable parts orienting". PhD thesis.

Vita

Ratan Sadanand Othayoth Mullankandy was born in Kannur, Kerala, India on October 10th 1992. He received his B.Tech degree in Mechanical Engineering from the National Institute of Technology Calicut, India in 2014, and the M.S.E degree in Mechanical Engineering from the Johns Hopkins University, Baltimore, MD, USA in 2017, where he is currently pursuing his Ph.D. degree in Mechanical Engineering. His research is focused on understanding principles of physical interaction of animals and robots with their environment during locomotion. He has published his research in journals including *PNAS*, *Proceedings of the Royal Society*, and *eLife*. He was shortlisted as the Best Student Paper finalist (Division of Comparative Biomechanics) at the SICB Annual Meeting in 2018 and 2019.